OPTICAL FREQUENCY MIXERS USING THREE-WAVE MIXING FOR OPTICAL FIBER COMMUNICATIONS

By
Ming-Hsien Chou
G.L. No. 5671

A DISSERTATION

SUBMITTED TO THE DEPARTMENT OF APPLIED PHYSICS

AND THE COMMITTEE ON GRADUATE STUDIES

OF STANFORD UNIVERSITY

IN PARTIAL FULFILLMENT OF THE REQUIREMENTS

FOR THE DEGREE OF

DOCTOR OF PHILOSOPHY

August 1999

I certify that I have read this dissertation and that in my opinion it is fully adequate, in scope and quality, as a dissertation for the degree of Doctor of Philosophy.

Martin M. Fejer (Principal Adviser)

I certify that I have read this dissertation and that in my opinion it is fully adequate, in scope and quality, as a dissertation for the degree of Doctor of Philosophy.

Robert L. Byer

I certify that I have read this dissertation and that in my opinion it is fully adequate, in scope and quality, as a dissertation for the degree of Doctor of Philosophy.

David A. B. Miller

Approved for the University Committee on Graduate Studies:

Abstract

The rapid evolution of broadband telecommunication systems is creating enormous demands for optoelectronic components with capacities beyond those currently available for transmission, multiplexing/demultiplexing, and switching. Examples of devices that could have major impact on future optical communication systems include all-optical wavelength converters in wavelength-division multiplexed (WDM) systems, all-optical gated mixers in optical time-division multiplexed (TDM) systems, and components for eliminating dispersion and nonlinear effects in fiber links. This dissertation describes the development of optical frequency (OF) mixers, analogous to the RF mixers in microwave signal processing technology, fabricated in periodically poled $LiNbO_3$ (PPLN) waveguides for optical fiber communications and other all-optical signal processing applications. Such OF mixers would be an enabling technology to realize high capacity and transparency in WDM and in high speed TDM systems.

The OF mixers developed in this dissertation are based on three-wave mixing using nonlinear optical effects based on the second-order nonlinear susceptibility $\chi^{(2)}$. In an OF mixer, the (usually weak) signal at frequency ω_s is mixed with a strong local oscillator at frequency ω_{LO} to generate an output at frequency $\omega_{out} = \omega_{LO} - \omega_s$. Such an OF mixer is well suited to communication applications. It can easily accommodate terahertz signal bandwidth, has negligible spontaneous emission noise, has no intrinsic frequency chirp, and can up and down convert multiple wavelengths with equal efficiency. Phasematching in the nonlinear frequency-mixing process can be accomplished by quasi-phasematching (QPM) structures, which can be engineered to design devices for various novel functions.

The main challenge with OF mixers is to fabricate a highly efficient device, capable of operating at local oscillator powers of tens of mW. With the development of efficient PPLN waveguides and integrated waveguide structures, several potentially important devices have been demonstrated, including efficient WDM wavelength converters within the 1.5-μm-band or between the 1.3-μm-band and the 1.5-μm-band, and spectral inverters for dispersion compensation in fiber links. By use of non-uniform QPM structures, multiple-channel wavelength converters for dynamic reconfiguration and broadcasting, as well as very broadband converters have also been demonstrated. Applications of OF mixers as optical gated mixers for TDM systems are investigated theoretically.

Acknowledgements

I have been extraordinarily privileged to work with many talented and generous people during my stay at Stanford. If I have matured as a good scientist and a better person, it has mainly come from interacting with them. It is a great pleasure for me to acknowledge these wonderful people.

My thesis advisor, Prof. Martin Fejer, has devoted invaluable amounts of time, attention, and support in guiding me through my Ph.D. research. His patience and advice were critical in helping me survive the dark days. Working for Marty has been a wonderful experience. His insight as well as his true devotion to science has been inspirational to me. I deeply owe my technical career to him.

Prof. Robert Byer's enthusiasm and optimism have always inspired me. I learned from him the importance of positive thinking to success, which will be invaluable to my future career and life.

It was a pleasure to have Prof. David Miller serve on my oral and reading committees. His careful reading of and comments on this dissertation have been very helpful. I thank the efforts of Prof. Steve Harris and Prof. Robert Feigelson, who served on my oral committee. I also appreciate Prof. Walter Harrision, my academic advisor, who has been very generous and important to me, especially in my first year at Stanford.

If I have had any luck in my research, it has come from working with many wonderful people in the lab. Dr. Igal Brener from Bell Labs, Lucent Technologies was the most important person in my research during my last year at Stanford. I cannot overstate how lucky I was to work with him. I am very impressed by his enthusiasm and efficiency. He brought me to Bell Labs as a visiting researcher, taught me practical fiber optics, and finally tried to create an opportunity for me to work at Bell Labs after my graduation.

I have also been very fortunate in working closely with two of Marty's students: Krishnan Parameswaran and Mark Arbore. Krishnan is always very helpful and optimistic. I am so grateful for having worked with him. We worked together to make significant progress on QPM waveguide technology. Without him around, I might still need to be working in the lab today. Mark taught me many things, from fundamental optics to QPM waveguides. I also learned from him how to make an efficient plan for graduate research.

I also enjoyed the interaction with Byer-Fejer group members and other Ginzton students. Greg Miller gave me a lot of insight into materials issues and cleanroom processing, and I also learned the spirit of persistence from him. Discussion with Yen-Chieh Huang, my lab TA and good friend, was very fruitful to both my graduate research and my future career. I also appreciate the friendship and help from the rest of the current and former Byer/Fejer group members (Loren Eyres, Gena Imeshev, Patrick Tourreau, Dong Zheng, Matt Lawrence, Todd Rutherford, Bill Tulloch, Rob Batchko, Gary Woods, Larry Myers, Michael Proctor, Leslie Gordon, Jan-Peter Meyn, Alex Alexandrovski, Gisele Foulon, Roger Route, Eric Gustafson, Kelly Koucky, Sandy Bretz, and more).

The Byer-Fejer group always attracts the very best students and scientists from around the world. This atmosphere proved to be very fruitful for me. I appreciate the one-year experience of working closely with Jerome Hauden, a post-doc from France and now a Prof. at Universite de Franche Comte. Through the interaction with Kazuo Fujiura, a visiting researcher from NTT, I started to investigate devices for TDM applications. Discussion of cascaded second order nonlinear processes with Katia Gallo, a visiting student from Italy, lead to my interest in pursuing that subject and generating very good results in the end. There are several others-too many to name all of them.

The support of the Ginzton laboratory staff really makes life and research easier. Paula Perron in the applied physics office, Tom Carver in the microfabrication laboratory, Chris Remen and Joe Vrehl in the crystal shop, Ted Bradshaw and Larry Randall in the machine shop, and Paul Jerabek in CIS have all helped me considerably.

The commitment to graduate studies has made me miss many activities outside the lab. Nevertheless, many friends have given me support whenever necessary. Special thanks go to Shih-Chi Chiu and Chin-Lung Chou. Shih-Chi has been my very good friend since we were in high school together. Chin-Lung and I came to Stanford in the same year and also finish in the same year. Without him, my first year at Stanford would have been miserable.

Finally, I want to thank my parents and my wife Wen-Hsiu for their deep understanding and endless support. I dedicate this dissertation to them with love.

Table of Contents

LIST OF ILLUSTRATIONS

CHAPTER 1

INTRODUCTION

1.1 Motivation

Development of high capacity optical networks has accelerated because of emerging demands for world-wide communications. Information, interactive multimedia service, electronic commerce, and many other services are efficiently delivered online through the Internet. Optical fiber communication serves as the enabling technology to realize those Internet activities. Today several tens of gigabits-per-second of data traffic are carried over many thousands of kilometers through optical fiber communication systems. Terabits-per-second communication systems are rapidly being developed and will be the backbone for the global world interconnection in the foreseeable future.

Transmission of high capacity data and, more importantly, the management of that high capacity data are the keys to the realization of terabits-per-second global networks. Such rapid evolution in communication systems is creating enormous demands for optoelectronic components with capabilities beyond those currently available. Examples of devices that could have major impact on such rapidly expanding systems include all-optical wavelength converters for wavelength reconfiguration and reuse in wavelength-division multiplexed (WDM) systems, all-optical gated mixers for managing high speed data in time-division multiplexed (TDM) systems, and components for eliminating dispersion and nonlinear effects in fiber links. The most natural approach to these devices requires an optical frequency analogue of the diode mixer omnipresent in radio frequency signal processing technology, in which an input signal is mixed with a local oscillator to generate a frequency-shifted output. However, such an optical frequency component is currently unavailable for efficient operation in optical fiber communication systems.

This dissertation is devoted to the development of an optical frequency (OF) mixer that can operate at microwatt-milliwatt signal powers and tens of milliwatts local oscillator (LO) powers based on second-order nonlinear effects. Demonstration of functions and evaluation of physics issues of such a device in a WDM system testbed are also provided. Communication devices based on strong second-order nonlinear frequency mixing offer a fundamentally different set of capabilities compared to other mixing schemes, and are essentially unexplored. Such devices would not only be an enabling technology for WDM and TDM networks, but could also open the door to more novel devices and applications. For instance, other devices that could be implemented based on the OF mixer developed in this dissertation include optical amplifiers that can be operated anywhere in the infrared spectrum, and optical transistors in which low power control beams switch high power signal beams.

After a brief summary of optical fiber communication systems to illustrate the demands for optical components, the concepts and applications of OF mixers are presented. The essential tool to fabricate efficient OF mixers is then discussed, followed with an overview of this dissertation.

1.2 Optical Fiber Communications

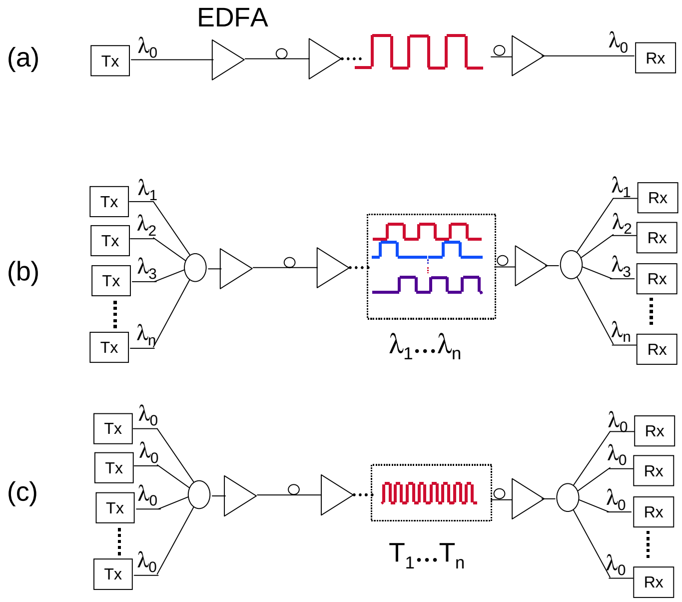

Figure 1.1 Schematic diagrams of optical fiber transmission systems. (a) Single-channel system; (b) WDM system, where multiple channels (with each channel carried by a different wavelength) are multiplexed into the same fiber to increase system capacity; (c) TDM system, where multiple channels (with each channel carried by the same wavelength) are interleaved with each other to increase system bit rate. (EDFA: Erbium-Doped-Fiber Amplifier; T_X: Transmitter; R_X: Receiver.)

In current optical fiber communication systems, there are two major approaches to increase transmission capacities: one is WDM [1, 2, 3, 4, 5, 6, 7] and the other is TDM [8, 9] as shown in figure 1.1. WDM opens up a whole new dimension for increasing the capacity and flexibility of communication networks. In WDM systems, multiple signal channels are independently transmitted through the same fiber with each channel carried by a different wavelength. One hundred signal channels and one terabit-per-second capacity in a single fiber were demonstrated in a Dense WDM (DWDM) system [10]. To advance from point-to-point applications as they are now towards a whole range of WDM networks, functions for controlling and processing multiple wavelengths are required. Although optoelectronic components will remain important in the future, other functions can be more efficient in all-optical operations. For example, erbium-doped-fiber amplifiers (EDFA's) allow amplification of more than one hundred wavelengths simultaneously, which was the key factor for the rapid advance of WDM systems. All-optical devices having similar advantages will be crucial to WDM networks. Examples of such all-optical devices are given in figure 1.2, including wavelength routers, switches, wavelength add/drops, and wavelength converters.

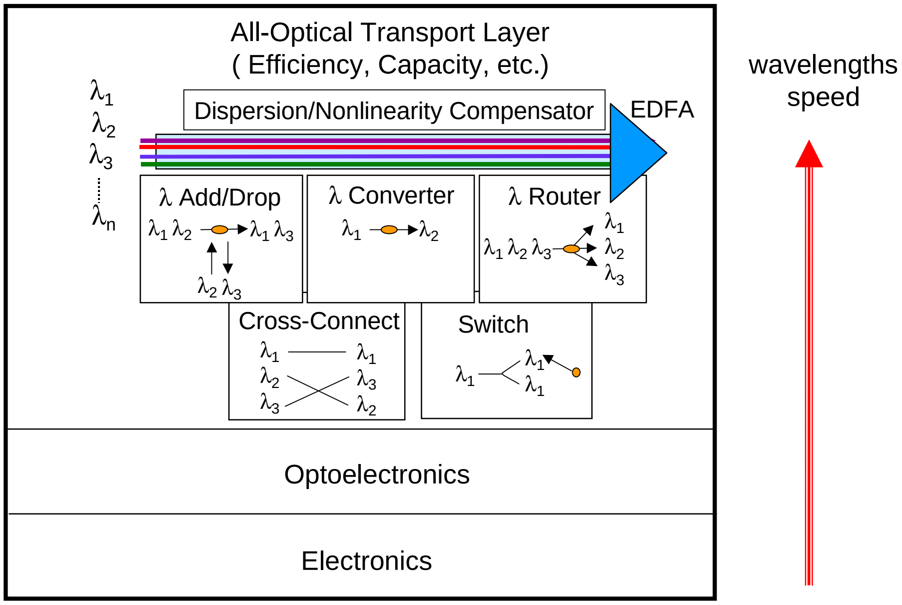

Figure 1.2 Examples of components for all-optical networks. As numbers of different wavelengths and system bit rate increase, there will be more demands for all-optical components.

TDM offers an alternative that is complementary to WDM. In a TDM system, multiple channels at low bit rate are multiplexed into a high bit rate stream where each channel occupies a fraction of the time slot. Currently the capacity of a single fiber is approaching one terabit-per-second in TDM systems [11]. Over three terabits-per-second transmission capacity of a single fiber has been achieved by combining WDM and TDM systems [12]. The main challenge in TDM systems is to process high speed data due to the speed limitation (currently ~40 Gbits/s) of electronic components. Optical techniques are needed to fully exploit the transmission bandwidth of optical fibers. Further limitations of the capacity expansion in transmission systems are the chromatic dispersion [13] and fiber nonlinearity [14], which limit the signal transmission distance. Methods to eliminate these impairments are required.

1.3 Optical Frequency (OF) Mixers

Principle and Application

In the radio frequency region, one can efficiently manipulate signals by a radio frequency (RF) mixer (figure 1.3(1a)), which mixes an input signal with a local oscillator to generate a frequency-shifted output. RF mixers are the basic building blocks in microwave signal processing technology. Modulation, detection, heterodyne receiving, and frequency multiplexing can be performed through currently available RF mixers. The high efficiency of the radio frequency mixing process is mainly due to the availability of very strongly nonlinear elements, such as diode junctions. Figure 1.3(1b) shows a typical I (current) versus V (voltage) response of a diode junction. With strongly nonlinear elements, one can realize broadband and efficient lumped RF mixers with devices much smaller than the wavelengths of the interacting waves.

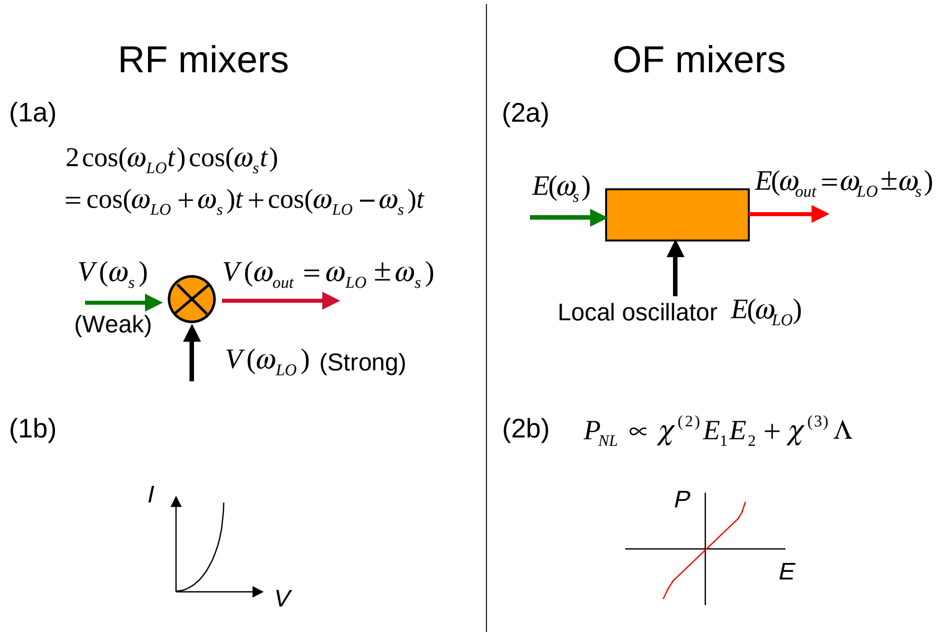

Figure 1.3 RF mixers vs. OF mixers: (1a) RF mixer; (1b) Typical I-V curve for a diode junction; (2a) OF mixer; (2b) Polarization *P* vs. electric field *E* for nonlinear materials.

In the optical frequency region, an optical element with strong nonlinearity is currently unavailable. Nonlinearities that come from materials' second-order nonlinear susceptibility ($\chi^{(2)}$) and third-order nonlinear susceptibility ($\chi^{(3)}$) in OF mixers as in figure 1.3(2b) are relatively weak compared to that of the diode junction in RF mixers. To realize an efficient OF mixer (figure 1.3(2a)) analogous to the RF mixer, a distributed mixer with length longer than the wavelengths of the interacting waves is necessary. Phasematching among the interacting waves must be preserved to ensure the efficient accumulation of the fields generated by the nonlinearities along the whole length of the device. Hence the weak nonlinearities impose technical challenges on the realization of efficient and broadband OF mixers.

The OF mixers we developed are based on three-wave mixing by use of the second-order nonlinear susceptibility $\chi^{(2)}$ (e.g. difference-frequency mixing (DFM), cascaded second-order nonlinear frequency mixing ($\chi^{(2)}$: $\chi^{(2)}$ mixing), and sum-frequency mixing (SFM)). Frequency-mixing processes are traditionally used for the generation of coherent light sources such as tunable visible [15, 16] and mid-infrared radiation [17, 18]. However, they also have various other applications in all-optical signal process functions [19]. In the following, DFM is used as an example to illustrate several basic functions of OF mixers.

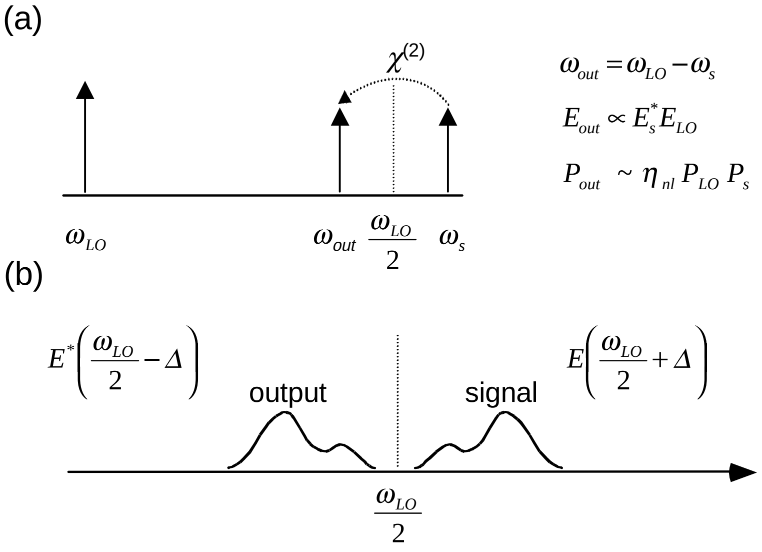

Figure 1.4 (a) A schematic description of DFM, which generates a frequency-shifted output. (b) The spectrum of the DFM output wave is inverted with respect to the input wave.

In a DFM-based OF mixer, as in a conventional RF mixer, the (usually weak) input signal at frequency ω_s is mixed with a strong local oscillator at frequency ω_{LO} to generate an output at frequency $\omega_{out} = \omega_{LO} - \omega_s$. Figure 1.4 summarizes the basic properties of DFM-based OF mixer. In the small signal limit, the output power P_{out} is linearly proportional to the signal power P_s, with a scaling factor proportional to the local oscillator power P_{LO}. This permits operation at arbitrarily low input signal power. To see the utility of a DFM-based OF mixer for communication applications, consider a local oscillator at a frequency close to twice that of the input signal. With $\omega_{LO} = 2\omega_s - \Delta$, the output frequency is $\omega_{out} = \omega_s - \Delta$; that is, the output frequency is shifted by an amount controlled by the offset of the local oscillator frequency. Another important property of DFM-based OF mixers results from the proportionality of the output wave to the complex conjugate of the input signal wave. If a chirped input signal spectrum $E(\omega_{LO}/2 + \Delta)$ is mixed with a local oscillator at ω_{LO}, the output spectrum is then $E^*(\omega_{LO}/2 - \Delta)$, effectively reversing the chirp on the input signal as illustrated in figure 1.4(b). This function allows complete "mid-span" correction of chromatic dispersion in any arbitrarily dispersed fiber link [20].

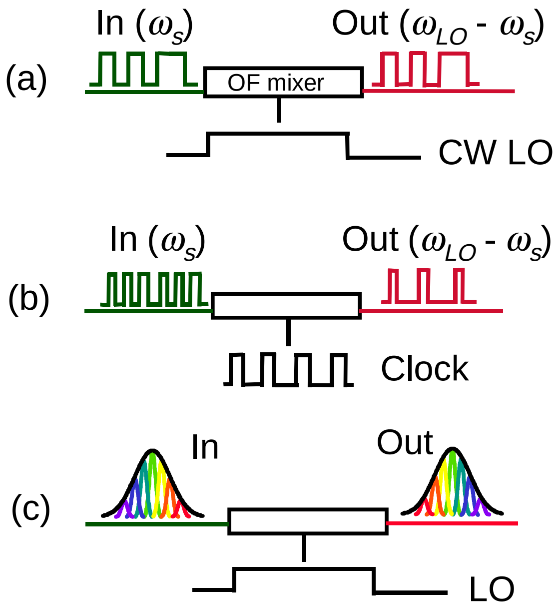

Figure 1.5 Examples of applications of OF mixers, which perform functions similar to RF mixers. (a) Wavelength Converter, converting input signal from one wavelength to another wavelength by using a CW LO. (b) Time Gated Mixer, extracting information from TDM signals using optical clocking. (c) Spectral Inverter, inverting signal chirp for dispersion compensation of fiber links.

An OF mixer based on $\chi^{(2)}$ is well suited to communication applications [19, 20, 21, 22, 23, 24, 25]. It is a transparent process preserving all amplitude, frequency and phase information. In addition, it is an instantaneous process that easily accommodates even terahertz modulation bandwidth. It has negligible spontaneous emission (parametric fluorescence) noise, has no intrinsic frequency chirp, can up and down convert multiple wavelengths with equal efficiency, and has no inherent limitation on wavelength-shift so that even a 1.5-µm to 1.3-µm conversion is straightforward. OF mixers can also be designed for a variety of novel functions by engineering the quasi-phasematching (QPM) structure [26, 27, 28, 29, 30]. Figure 1.5 shows several examples of applications of OF mixers.

Figure of Merit (FOM) of OF Mixers

From an application standpoint, the two most important parameters describing the performance of OF mixers are the conversion efficiency η and the wavelength acceptance bandwidth. In DFM [31, 32] the small signal conversion efficiency can be written as

$$\eta = P_{out} / P_s \approx \eta_{nl} P_{LO} \ . \tag{1.1}$$

Where η_{nl} is the nonlinear mixing efficiency in units of %/W, which characterizes the material properties and device geometry. The nonlinear mixing efficiency η_{nl} of guided-wave nonlinear frequency mixing can be expressed as

$$\eta_{nl} = \eta_{norm} L^2 \propto \frac{\chi^{(2)\,2}}{n^3} \frac{L^2}{A_{eff}} \operatorname{sinc}^2\left(\frac{\Delta\beta L}{2}\right) \ . \tag{1.2}$$

η_{norm} is the normalized efficiency expressed in units of %/W-cm^2 and is independent of the length of the device. The first factor in the proportional relation characterizes the material's FOM, where $\chi^{(2)}$ is the second-order nonlinear susceptibility and *n* is the refractive index. The second and third factors are related to the waveguide geometry and the phasematching among interacting waves, respectively. *L* is the interaction length. A_{eff} is the effective area, which quantifies the overlap of the interacting waves and the material's second-order nonlinear susceptibility $\chi^{(2)}$. $\Delta\beta$ is the phase-mismatch among interacting waves and is defined by the relation

$$\Delta\beta = \beta_{LO} - \beta_s - \beta_{out} \ , \tag{1.3}$$

where β_i (*i* = *LO, s* and *out*) represent the propagation constants of the interacting waves. In annealed proton-exchanged periodically poled LiNbO$_3$ (APE-PPLN) waveguides operating at 1.5 µm, the theoretical value of normalized efficiency η_{norm} is 50-100%/W-cm^2. In a 5-cm-long waveguide the nonlinear mixing efficiency η_{nl} is 1000-2500%/W, thus 0-dB conversion efficiency can be expected by using 780-nm local oscillator with power less than 100 mW. In an orientation-patterned AlGaAs device [33], η_{norm} is an order of magnitude larger, so that the same performance could be achieved by a local oscillator with power less than 10 mW.

The signal bandwidth of an OF mixer, about 50-100 nm for a typical configuration, is broader than the bandwidth of a typical EDFA. A wider bandwidth accommodates a larger number of WDM channels (currently the channel separation is ~0.4-0.8 nm/channel). But the local oscillator bandwidth, which scales inversely to the length of the device, is narrow; it is about 0.1 nm for a typical OF mixer configuration. However, non-uniform quasi-phasematching (QPM) structures [34] can be used to increase the local oscillator bandwidth. In the application as an optical gated mixer where both the control wave and input signal wave are short pulses and at significantly different wavelengths, group-velocity mismatch among the interacting waves limits the usable length of the device. For example, the walk-off distance is ~0.3 mm for one-picosecond pulses at wavelengths of 780 nm and 1550 nm in a PPLN device. Thus, techniques conceptually similar to QPM should be implemented to achieve quasi-group-velocity matching.

Essential Tools for OF Mixers

The main challenge of OF mixers is to fabricate a highly efficient device, capable of operating at local oscillator powers of tens of mW. There have been proof-of-principle communication-band mixers fabricated in QPM $LiNbO_3$ waveguides [21, 22]. Although these devices showed the expected wavelength-shifting function and the predicted extremely broad signal acceptance bandwidth, the devices suffered sufficiently serious limitations that system characterization was impractical and further communication applications were not pursued. In particular, difficulty in robustly launching the input signal and local oscillator into the waveguide and an efficiency lower than desired were major problems. For the realization of practical OF mixers, several essential techniques including QPM, waveguides, and integrated waveguide structures needed to be further addressed, and thus constitute a major portion of this dissertation.

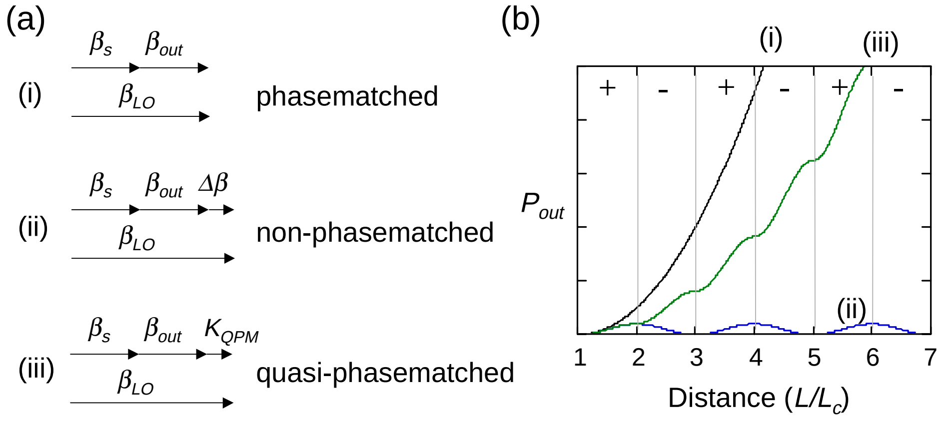

Figure 1.6 (a) A schematic description of three-wave mixing. (b) The growth of converted output power with distance for (i) phasematched, (ii) non-phasematched, and

(iii) quasi-phasematched interactions. The + and – sign represents the sign of the second-order nonlinear susceptibility $\chi^{(2)}$.

In a conventionally phasematched frequency-mixing device, the interacting waves travel with the same phase velocity, so the phase relationship among the interacting waves is preserved along the whole interaction length. As a consequence, power monotonically flows from the local oscillator to the other waves, and the output power grows with distance. Waves travel with different phase velocities in a non-phasematched interaction, which causes accumulation of phase error among the waves. As a result, the output power oscillates, i.e. it grows until a phase-shift of π is accumulated and then it decreases afterwards to zero when a phase-shift of 2π is accumulated. The characteristic length for a π phase-shift to be accumulated is called the coherence length L_c, which is defined as

$$L_c = \frac{\pi}{\Delta\beta}, \tag{1.4}$$

where $\Delta\beta$ is defined graphically in figure 1.6. In QPM [26, 27, 28], resetting the phase-shift to zero once it grows to π will prevent the oscillation of the output power owing to the accumulated phase mismatch. In the implementation of first-order QPM, the sign of the nonlinear susceptibility is reversed every coherence length L_c so that the change in the sign of nonlinear polarization compensates for the accumulated phase mismatch. The phase mismatch offset by the QPM-grating becomes

$$\Delta\beta' = \Delta\beta - K_{QPM}, \tag{1.5}$$

where $K_{QPM} = \pi/L_c$ for the first-order QPM. Figure 1.6 shows the schematic description of phasematched, non-phasematched, and quasi-phasematched conditions. QPM allows for any particular desired interaction because the phase-velocity mismatch can be compensated by periodically modulating the sign of material's nonlinear susceptibility. That is, QPM permits the use of otherwise non-phasematched, yet highly nonlinear materials. Figure 1.6(a) shows the wave-vector relationship among interacting waves and figure 1.6(b) shows the growth of the converted output power with distance for phasematched, quasi-phasematched, and non-phasematched conditions.

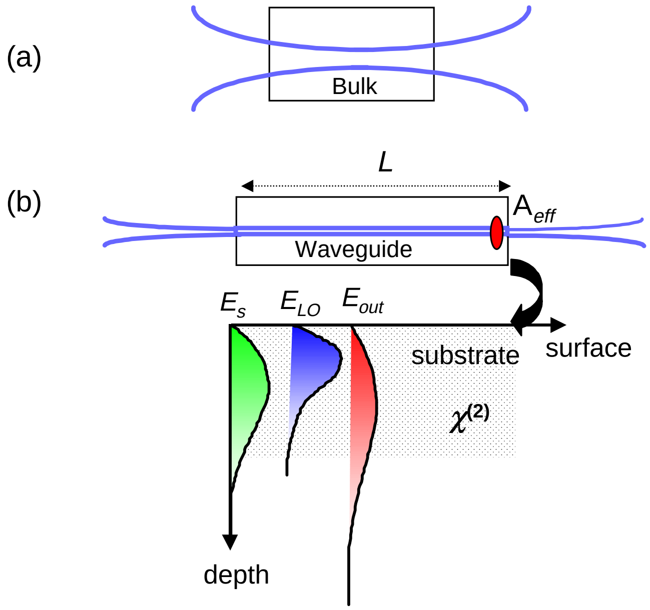

Figure 1.7 Schematic drawings of nonlinear frequency mixing. (a) Diffraction associated with bulk media; (b) Optical confinement provided by a waveguide; Optimization of mode overlap among the interacting waves (E_s, E_{LO}, E_{out}) and second-order nonlinear susceptibility ($\chi^{(2)}$) is important for efficient devices.

Waveguides can further enhance nonlinear mixing efficiency η_{nl}, as compared to bulk media, by tightly confining optical fields over long distances. Figure 1.7 shows a schematic drawing of nonlinear frequency mixing in a bulk medium and in a waveguide. When a tightly focused wave propagates in a bulk device it will diffract, so high efficiency cannot be achieved. In waveguides the mode profile is confined to a transverse dimension on the order of the wavelength. High optical intensities can be maintained over considerable distances to improve efficiency by two to three orders of magnitude as compared to bulk devices. Nonlinear mixing efficiency η_{nl} is quadratically proportional to the interaction length L (as in equation (1.2)), thus fabrication of long, uniform, and low-loss waveguides is essential for high efficiency OF mixers. In addition, optimization of the waveguide geometry is important for efficient devices, since the normalized efficiency η_{norm} is directly related to the mode overlap of the interacting waves and the material's second-order nonlinear susceptibility [35, 36].

A waveguide optimized for nonlinear frequency mixing in general has a tightly confined mode to reduce the effective area A_{eff} (referred to equation (1.2)). The tightly confined mode is not well mode-matched to the optical fiber, so coupling between waveguides and fibers is not efficient. In addition, mode coupling is difficult for non-symmetric waveguide modes which are the general mode profiles in the depth direction for ion exchanged and diffused waveguides (shown in figure 1.7(b)). Nonlinear frequency mixing in the waveguide involves two or three interacting waves at significantly different wavelengths, which complicates the mode coupling even more and thus inhibits practical applications of the device [37]. In Chapter 4 we will describe the waveguide structures that integrate mode-coupling components and nonlinear frequency-mixing sections to allow robust coupling of interacting radiation and achieve device optimization.

1.4 Overview of This Dissertation

Figure 1.8 highlights the roles of this thesis in the development of the enabling technology for optical networks. The development of networks, systems, and subsystems requires adequate components and modules, which are very often limited by the fundamental physics and material issues. This thesis starts from understanding the physics for guided-wave nonlinear frequency conversion and solving the material issues (APE-PPLN waveguide fabrication). Then, based on the understood and/or developed tools (QPM, PPLN waveguides, integrated mode-coupling structures, Fourier transform synthesis of tuning curves), several telecommunication OF mixers are fabricated and their performance is tested.

The design and fabrication techniques developed in the research produce PPLN waveguides with a maximum interaction length of 56 mm, close to an ideal sinc^2 tuning curve, and nonlinear mixing efficiency η_{nl} of more than 750%/W (including waveguide propagation losses). The integrated waveguide structures developed in this research allow for robust coupling of the interacting waves, which is essential for practical device operation. The device quality and integrated waveguide structures allowed for the demonstration of generic OF mixers, useful for a variety of applications in WDM and TDM optical systems. By use of engineerable QPM structures, multiple-channel mixers and bandwidth-broadened mixers have also been demonstrated. The results accomplished in this research, with some further improvements, will lead to OF mixers as practical components for optical fiber communications and other all-optical signal processing applications. The organization of this dissertation is summarized in the following paragraph.

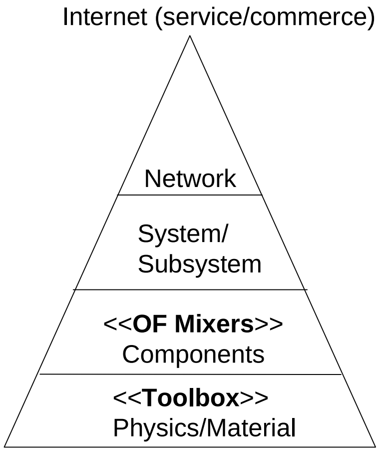

Figure 1.8 Role of this thesis in the development of the enabling technology for optical networks. Toolbox includes several essential tools (QPM, waveguides, mode coupling structures, and Fourier synthesis of tuning curves) for efficient OF mixers.

Chapter 2 derives the coupled-mode equations for guided-wave nonlinear frequency mixing. Chapter 3 describes the design and fabrication of efficient APE-PPLN waveguides. Chapter 4 describes the integrated waveguide structures for nonlinear frequency conversion. These three chapters provide the basis for efficient OF mixers for several telecommunication applications, as described in Chapter 5 through Chapter 7. Chapter 5 contains the application of OF mixers as wavelength converters in WDM systems. Chapter 6 shows the application for dispersion compensation in fiber links. Chapter 7 describes novel OF mixers based on non-uniform QPM structures. Finally, Chapter 8 concludes this dissertation. Applications of OF mixers in TDM systems will be described in Appendix A.

References for Chapter 1:

---

1. C. A. Brackett, “Dense wavelength division multiplexing networks: principles and applications,” *IEEE J. Select. Areas Commun.* **8**, 948-964 (1990).
2. C. A. Brackett, A. S. Acampora, J. Sweitzer, G. Tangonan, M. T. Smith, W. Lennon, K.–C. Wang, R. H. A. Hobbs, “Scalable multiwavelength multihop optical network: a proposal for research on all-optical networks,” *IEEE J. Lightwave Technol.* **11**, 736-753 (1993).
3. A. E. Willner, “Mining the optical bandwidth for a terabit per second,” *IEEE Spectrum*, **34**, 32-41, (1997).
4. I. P. Kaminow, C. R. Doerr, C. Dragone, T. Koch, U. Koren, A. A. M. Saleh, A. J. Kirby, C. M. Ozveren, C. M. B. Schofield, R. E. Thomas, R.. A. Barry, D. M. Castagnozzi, V. W. S. Chan, B. R. Jr. Hemenway, D. Marquis, S. A. Parikh, M. L. Stevens, E. A. Swanson, S. G. Finn, R. G. Gallager, “A wideband all-optical WDM network,” *IEEE J. Lightwave Technol.* **14**, 780-799 (1996).
5. T. Ono and Y. Yano, “Key technologies for terabit/second WDM systems with high spectral efficiency of over 1 bit/s/Hz,” *IEEE J. Quantum Electron.* **34**, 2080-2088 (1998).
6. A. R. Chraplyvy, R. W. Tkach, “Terabit/second transmission experiments,” *IEEE J. Quantum Electron.* **34**, 2103-2108, (1998).
7. L. Kazovsky, S. Benedetto, A. E. Willner, *Optical Fiber Communication Systems*, Artech House, Boston 1996. pp. 529-603.
8. S. Kawanishi, “Ultrahigh-speed optical time-division-multiplexed transmission technology based on optical signal processing,” *IEEE J. Quantum Electron.* **34**, 2064-2079 (1998).
9. J. D. Moores, J. Korn, K. L. Hall, S. G. Finn, K. A. Rauschenbach, “Ultrafast optical TDM networking: extension to the wide area,” *IEICE Trans. Commun.* **E82-B**, 209-221 (1999).
10. A. K. Srivastava, Y. Sun, J. Sulhoff, C. Wolf, M. Zirngibl, R. Monnard, A. R. Chraplyvy, A. A. Abramov, R. P. Espindola, T. A. Strasser, J. R. Pedrazzani, A. M. Vengsarkar, J. L. Zyskind, J. Zhou, D. A. Ferrand, P. F. Wysocki, J. B. Judkins, and Y. P. Li, “1 Tb/s transmission of 100 WDM 10 Gb/s channels over 400 km of TrueWave fiber,” *OFC’98*, PD10.
11. M. Nakazawa, E. Yoshida, T. Yamamoto, E. Yamada, A. Sahara, “TDM single channel 640 Gbit/s transmission experiment over 60 km using a 400 fs pulse train and a walk-off free, dispersion-flattened nonlinear optical loop mirror,” *OFC’98*, PD 14.
12. S. Kawanishi, H. Takara, K. Uchiyama, I. Shake, and K. Mori, “3 Tbit/s (160 Gbit/s x 19 ch) OTDM-WDM transmission experiment,” *OFC’99*, PD1.
13. A. M. Vengsarkar, “Dispersion compensation techniques,” *OFC’98*, TuL.
14. G. P. Agrawal, *Nonlinear Fiber Optics*, 2nd ed., Academic Press, San Diego 1995.

---

15. Y. Kitaoka, K. Yamamoto, K. Mizuuchi, K. Narumi, M. Kato, “Blue second-harmonic generation waveguide device and its application to high-density optical disk,” *CLEO’98*, CWG1.
16. G. D. Miller, “Periodically poled lithium niobate: modeling, fabrication, and nonlinear optical performance,” Ph.D. Dissertation, Department of Electrical Engineering, Stanford University, Stanford, CA (1998).
17. See feature issues on OPOs, *J. Opt. Soc. Am. B* **10**, 2151-2218 (1993) and *J. Opt. Soc. Am. B* 12, 2147-2209 (1995).
18. L. E. Myers, “Quasi-phasematched optical parametric oscillators in bulk periodically poled lithium noibate,” Ph.D. Dissertation, Department of Electrical Engineering, Stanford University, Stanford, CA (1995).
19. S. J. B. Yoo, “Wavelength conversion technologies for WDM network applications,” *J. Lightwave Technol*. **14**, 955-966 (1996).
20. I. Brener, M. H. Chou, G. Lenz, R. Scotti, E. E. Chaban, J. Shmulovich, D. Philen, K. R. Parameswaran, and M. M. Fejer, “High efficiency (-7 dB), wideband (70 nm) and tunable LiNbO3-waveguide mid-span spectral inverter and its use for dispersion compensation in 4x10 Gb/s,” *ECOC ’99*, WB1.
21. C. Q. Xu, H. Okayama, and M. Kawahara, “1.5 μm band efficient broadband wavelength conversion by difference frequency generation in a periodically domain-inverted $LiNbO_3$ channel waveguide,” *Appl. Phys. Lett.* **63**, 3559-3561 (1993).
22. M. L. Bortz, D. Serkland, M. M. Fejer, and S. J. B. Yoo, “Near degenerate difference frequency generation at 1.3 μm in $LiNbO_3$ waveguides for application as an all-optical channel shifter,” *CLEO’94*, CTHD6.
23. S. J. B. Yoo, C. Caneau, R. Bhat, M. A. Koza, A. Rajhel, N. Antoniades, “Wavelength conversion by difference frequency generation in AlGaAs waveguides with periodic domain inversion achieved by wafer bonding,” *Appl. Phys. Lett.* **68**, 2609-2611 (1996).
24. M. H. Chou, J. Hauden, M. A. Arbore, and M. M. Fejer, “1.5 μm band wavelength conversion based on difference frequency generation in $LiNbO_3$ waveguides with integrated coupling structures,” *Opt. Lett.* **23**, 1004-1006 (1998).
25. M. H. Chou, I. Brener, M. M. Fejer, E. E. Chaban, and S. B. Christman, “1.5-μm-band wavelength conversion based on cascaded second-order nonlinear susceptibility in $LiNbO_3$ waveguides,” *Photonics Technol. Lett.* **11**, 653-655 (1999).
26. J. A. Armstrong, N. Bloembergen, J. Ducuing, and P. S. Pershan, “Interactions between light waves in a nonlinear dielectric,” *Phys. Rev. Lett.* **127**, 1918-1939 (1962).
27. P. A. Franken and J. F. Ward, “Optical harmonics and nonlinear phenomena,” *Rev. Mod. Phys.* **35**, 23-39 (1963).

28. M. M. Fejer, G. A. Magel, D. H. Jundt, R. L. Byer, “Quasi-phase-matched second harmonic generation: tuning and tolerances,” *IEEE J. Quantum Electron.* **28**, 2631-2654 (1992).
29. M. A. Arbore, “Generation and manipulation of infrared light using quasi-phasematched devices: ultrashort-pulse, aperiodic-grating and guided-wave frequency conversion,” Ph.D. Dissertation, Department of Electrical Engineering, Stanford University, Stanford, CA (1998).
30. G. Imeshev, A. Galvanauskas, D. Harter, M. A. Arbore, M. Proctor, M. M. Fejer, “Engineerable femtosecond pulse shaping by second-harmonic generation with Fourier synthetic quasi-phase-matching gratings,” *Opt. Lett.* **23**, 864-866 (1998).
31. R. L. Byer, “Parametric oscillators and nonlinear materials,” in *Nonlinear Optics*, P. G. Harper and B. S. Wherrett eds.(Academic, San Francisco, 1977), pp. 47-160.
32. R. A. Baumgartner and R. L. Byer, “Optical parametric amplification,” *IEEE J. Quantum Electron.* **15**, 432-444 (1979).
33. L. A. Eyres, C. B. Ebert, M. M. Fejer, J. S. Harris, “MBE growth of laterally antiphase-patterned GaAs films using thin Ge layers for waveguide mixing,” *CLEO’98*, CWH4.
34. M. H. Chou, I. Brener, K. Parameswaran, and M. M. Fejer, “Stability and bandwidth enhancement of difference frequency generation based wavelength conversion by pump detuning,” *CLEO’99*, CWB8.
35. E. J. Lim, “Quasi-phasematching for guided-wave nonlinear optics in lithium niobate,” Ph.D. Dissertation, Department of Electrical Engineering, Stanford University, Stanford, CA (1992).
36. M. L. Bortz, “Quasi-phasematched optical frequency conversion in lithium niobate waveguides,” Ph.D. Dissertation, Department of Applied Physics, Stanford University, Stanford, CA (1994).
37. M. H. Chou, M. A. Arbore, and M. M. Fejer, “Adiabatically tapered periodic segmentation of channel waveguides for mode-size transformation and fundamental mode excitation,” *Opt. Lett.* **21**, 794-796 (1996).

CHAPTER 2

THEORY OF GUIDED-WAVE QUASI-PHASEMATCHED OPTICAL FREQUENCY MIXING

2.1 Introduction

Guided-wave quasi-phasematched optical frequency mixing is an efficient method for the generation of coherent radiation and manipulation of optical frequency signals. By mixing two input waves in a second-order nonlinear medium via difference-frequency mixing (DFM) or optical parametric amplification (OPA), one can generate coherent infrared radiation for spectroscopic applications such as molecular sensing [1] or perform optical signal processing in telecommunication systems [2, 3, 4]. Widely tunable infrared radiation can be generated from one strong pump by optical parametric generation (OPG) [5, 6] and optical parametric oscillation (OPO) [7, 8], in which the pump is mixed with vacuum noise input.

The OF mixers developed in this work are based on guided-wave quasi-phasematching (QPM) by use of the second-order nonlinear susceptibility, $\chi^{(2)}$, implemented by DFM and by cascaded second-order nonlinear frequency mixing ($\chi^{(2)}$:$\chi^{(2)}$ mixing). In this chapter, we give a brief summary of some well-known $\chi^{(2)}$-based wave mixing phenomena that are useful for developing communication OF mixers. Basic concepts of nonlinear optics and waveguide theory used in the derivation can be found in several textbooks [9, 10, 11, 12, 13] and will not be repeated in this chapter.

2.2 Difference-Frequency Mixing

DFM is a three-wave-mixing process where a strong local oscillator at frequency ω_{LO} is mixed with a (usually weak) signal at frequency ω_s to generate a frequency-shifted output $\omega_{out}=\omega_{LO} - \omega_s$ via the second-order nonlinear susceptibility, $\chi^{(2)}$. A schematic description of DFM is shown in figure 2.1. In the following, we derive the coupled-mode equations governing the three-wave interaction in nonlinear waveguides and discuss their solutions [14, 15, 16, 17].

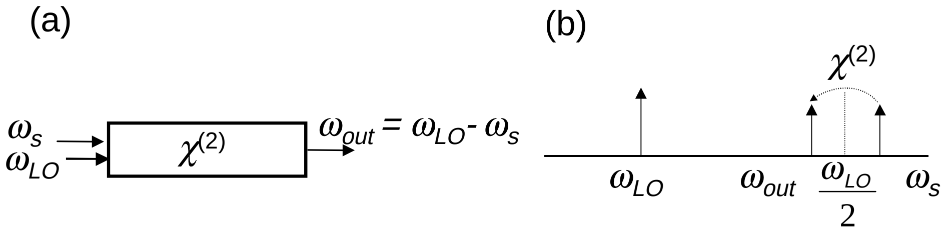

Figure 2.1 Schematic descriptions of difference-frequency mixing between a strong local oscillator at ω_{LO} and a signal at ω_s

Coupled-Mode Equations of Three-Wave Mixing

The nonlinear wave equations in the waveguide governing the wave interactions can be written as a one-dimensional scalar equation:

$$\frac{\partial^2 E}{\partial z^2} - \mu_0 \sigma \frac{\partial E}{\partial t} - \mu_0 \varepsilon_0 \varepsilon \frac{\partial^2 E}{\partial t^2} = \mu_0 \frac{\partial^2 P_{NL}}{\partial t^2}, \tag{2.1}$$

where $E=E_{LO}+E_s+E_{out}$ is the electric field of the interacting waves, P_{NL} is the nonlinear polarization induced in the medium by the electric field, σ is the conductivity, ε is the dielectric constant, μ_0 is the permeability of free space, and ε_0 is the permittivity of free space. For simplicity, we assume that the waves in the waveguide can be treated as propagating in a single waveguide mode. Thus the electric field can be expressed as

$$E_i(x,y,z,t) = \frac{1}{2}\gamma_i e_i(x,y)\left\{A_i(z,t)\exp[j(\omega_i t - \beta_i z)] + c.c.\right\}. \tag{2.2}$$

The subscripts i = *LO*, *s*, and *out* refer to the local oscillator, input signal, and output waves, respectively. $\gamma_i \equiv \sqrt{\frac{2}{n_i c_0 \varepsilon_0}}$ is a normalization constant, where $n_i \equiv \sqrt{\varepsilon(\omega_i)}$ is the refractive index and c_0 is the velocity of light in free space. $e_i(x,y)$ is the normalized transverse field profile and is defined by

$$\iint_{-\infty}^{\infty} e_i^2(x,y)\,dxdy = 1 \ . \tag{2.3}$$

The above normalization makes the square of $A_i(z,t)$ equal to the power of the corresponding wave (i.e. optical power $P_i = |A_i(z,t)|^2$). The function $A_i(z,t)$ containing both amplitude and phase information describes the temporal and spatial evolution of the field envelope in the propagation direction z. The component of nonlinear polarization that is quadratic in the electric field can be expressed as

$$P_{NL} = \frac{1}{2}\chi^{(2)}\varepsilon_0 E^2 = d_0 d(x,y) d(z)\varepsilon_0 E^2 \ , \tag{2.4a}$$

$$P_{NL,LO} = 2d_0 d(x,y) d(z)\varepsilon_0 E_s E_{out} \ , \tag{2.4b}$$

$$P_{NL,s} = 2d_0 d(x,y) d(z)\varepsilon_0 E_{LO} E_{out}^* \ , \tag{2.4c}$$

$$P_{NL,out} = 2d_0 d(x,y) d(z)\varepsilon_0 E_{LO} E_s^* \ , \tag{2.4d}$$

where d_0 is the nonlinear coefficient in single-domain bulk medium and is related to the second-order nonlinear susceptibility by $\chi^{(2)} = 2d_0 d(x,y)d(z)$. $d(x,y)$ is the normalized nonlinearity distribution in the transverse cross-section, and ranges between 0 and 1. $d(z)$ is the normalized nonlinearity distribution in the propagation direction z, and ranges between 1 and -1. Note for the special case of second-harmonic generation (SHG), the nonlinear polarization is given by $P_{NL,2\omega} = d_0 d(x,y) d(z)\varepsilon_0 E_\omega^2$, rather than the expression in equation (2.4d).

Under the slowly varying envelope approximation (SVEA), where the field amplitude changes slowly relative to the fast optical carrier frequency, by substituting equation (2.2) and equations (2.4) into equation (2.1), we can get the coupled-wave equations describing the evolution of the fields in the propagation direction,

$$\frac{\partial}{\partial z}A_{LO} + \frac{1}{v_{g_{LO}}}\frac{\partial}{\partial t}A_{LO} = -j\kappa_{LO} d(z) A_s A_{out} \exp(j\Delta\beta_0 z) - \frac{\alpha_{LO}}{2}A_{LO}, \tag{2.5a}$$

$$\frac{\partial}{\partial z}A_s + \frac{1}{v_{g_s}}\frac{\partial}{\partial t}A_s = -j\kappa_s d(z) A_{LO} A_{out}^* \exp(-j\Delta\beta_0 z) - \frac{\alpha_S}{2}A_s, \tag{2.5b}$$

$$\frac{\partial}{\partial z}A_{out} + \frac{1}{v_{g_{out}}}\frac{\partial}{\partial t}A_{out} = -j\kappa_{out} d(z) A_{LO} A_s^* \exp(-j\Delta\beta_0 z) - \frac{\alpha_{out}}{2}A_{out}. \tag{2.5c}$$

In equation (2.5), $A_i \equiv A_i(z,t)$ ($i = LO, s, out$) as in equation (2.2), $v_{g_i} = (\mathrm{d}\beta_i/\mathrm{d}\omega_i)^{-1}$ is the group-velocity of the mode at frequency ω_i, $\alpha_i = \mu_0\sigma_i c_0/2$ is the power loss coefficient (waveguide propagation loss). The phase mismatch $\Delta\beta_0$ is defined by

$$\Delta\beta_0 = \beta_{LO} - \beta_s - \beta_{out} = \left(\frac{n_{LO}}{\lambda_{LO}} - \frac{n_s}{\lambda_s} - \frac{n_{out}}{\lambda_{out}} \right), \tag{2.6}$$

where the n_i are the effective indices of the waveguide modes, defined implicitly in equation (2.6). κ_i is the coupling coefficient, defined by

$$\kappa_i = \sqrt{\frac{8\pi^2 d_0^{\,2}}{n_{LO} n_s n_{out} c \varepsilon_0 \lambda_i^2}}\ \vartheta \ . \tag{2.7}$$

ϑ is the overlap integral defined by

$$\vartheta = \iint_{-\infty}^{\infty} d(x,y) e_{LO}(x,y) e_s(x,y) e_{out}(x,y) dxdy \ . \tag{2.8}$$

The group-velocity dispersion is ignored in equation (2.5), since it will have impact on the frequency-mixing process only when the pulse length approaches 10-100 fs, which is much shorter than the general pulse width (>ps) used in communication systems. The inverse square of the overlap integral ϑ is commonly referred to as the effective area A_{eff} (i.e. $A_{eff} = 1/\left|\vartheta\right|^2$), which describes the strength of overlap among the modes of the interacting waves and the transverse profile of the normalized nonlinearity. Efficiency optimization in waveguide devices requires designing the waveguide geometry to maximize the overlap integral (i.e. minimize the effective area).

For QPM structures [14, 15, 18, 19], which use a periodic axial modulation in the nonlinear coefficient to compensate for index dispersion, $d(z)$ is a periodic function with a modulation period of Λ_{QPM} along the propagation and can be written as a Fourier series:

$$d(z) = \sum_m G_m \exp(-j\, 2\pi m z / \Lambda_{QPM}) \,, \tag{2.9}$$

where the Fourier coefficients are given by

$$G_m = \frac{1}{\Lambda_g} \int_{-\Lambda_g/2}^{\Lambda_g/2} d(z) \exp(j\, 2\pi m z / \Lambda_{QPM}) \,. \tag{2.10}$$

In order to evaluate the nonlinear optical interaction in the periodic medium, equation (2.9) was inserted into equations (2.5). By assuming that $\Lambda_{QPM} << L$ (i.e. the device is much longer than the QPM period, which is generally true ($L/L_c > 10^4$)), equations (2.5) can be simplified to an expression containing only the term close to phasematching:

$$\frac{\partial}{\partial z}A_{LO}+\frac{1}{v_{g_{LO}}}\frac{\partial}{\partial t}A_{LO}=-j\kappa_{eff,LO}A_sA_{LO}\exp(j\Delta\beta_0 z)-\frac{\alpha_{LO}}{2}A_{LO}\,, \tag{2.11a}$$

$$\frac{\partial}{\partial z}A_s+\frac{1}{v_{g_s}}\frac{\partial}{\partial t}A_s=-j\kappa_{eff,s}A_{LO}A_{out}^*\exp(-j\Delta\beta_0 z)-\frac{\alpha_s}{2}A_s\,, \tag{2.11b}$$

$$\frac{\partial}{\partial z}A_{out}+\frac{1}{v_{g_{out}}}\frac{\partial}{\partial t}A_{out}=-j\kappa_{eff,out}A_{LO}A_s^*\exp(-j\Delta\beta_0 z)-\frac{\alpha_{out}}{2}A_{out}\,. \tag{2.11c}$$

The phase mismatch in the QPM structure is compensated by the grating vector K_{QPM} = $2\pi/m\Lambda_{QPM}$ and is expressed as

$$\Delta\beta=\beta_{LO}-\beta_s-\beta_{out}-K_{QPM}=2\pi\left[\frac{n_{LO}}{\lambda_{LO}}-\frac{n_s}{\lambda_s}-\frac{n_{out}}{\lambda_{out}}-\frac{1}{m\Lambda_{QPM}}\right]. \tag{2.12}$$

κ_{eff} is the *effective* coupling coefficient, defined by

$$\kappa_{eff,i}=\sqrt{\frac{8\pi^2 d_{eff}{}^2}{n_1n_2n_3c\varepsilon_0\lambda_i^2}}\ \vartheta=\frac{d_{eff}}{d_0}\kappa_i\ . \tag{2.13}$$

$d_{eff}\equiv d_0G_m$ is the effective nonlinearity for the QPM process. When the nonlinear coefficient is modulated with periodic sign reversal, the Fourier coefficient is $G_m=(2/m\pi)\sin(m\pi D)$, where the duty cycle D = l/Λ_{QPM} is given by the length l of a reversed domain divided by the period Λ_{QPM} of domain reversal. The effective nonlinear coefficient for QPM of a first-order process (m=1) with 50% duty cycle factor is

$$d_{eff}=\frac{2}{\pi}d_0\,. \tag{2.14}$$

When a CW local oscillator is used, and the group-velocity mismatch between the signal and the output can be ignored ($\lambda_s\sim\lambda_{out}$), equations (2.11) can be simplified as

$$\frac{d}{dz}A_{LO}=-j\kappa_{eff,LO}A_sA_{out}\exp(j\Delta\beta z)-\frac{\alpha_{LO}}{2}A_{LO}\,, \tag{2.15a}$$

$$\frac{d}{dz}A_s=-j\kappa_{eff,s}A_{LO}A_{out}^*\exp(-j\Delta\beta z)-\frac{\alpha_s}{2}A_s\,, \tag{2.15b}$$

$$\frac{d}{dz}A_{out} = -j\kappa_{eff,out}A_{LO}A_s^* \exp(-j\Delta\beta z) - \frac{\alpha_{out}}{2}A_{out}\,. \tag{2.15c}$$

Equations (2.11) and equations (2.15) represent useful formulas for describing QPM guided-wave nonlinear optics. Although the notation used here is convenient for DFM and OPA/OPG, it can also be adjusted to other frequency processes such as sum-frequency generation.

Solution

The solutions of the above equations generally can only be expressed in integral formats and require numerical integration to obtain the results [14, 15, 16, 17, 18]. In the limit of an undepleted pump and a lossless waveguide, one can get analytic solutions for DFM using the boundary condition $A_{out}(0)=0$:

$$A_{LO}(L) = A_{LO}(0)\,, \tag{2.16a}$$

$$A_s(L) = A_s(0)\cosh gL\,, \tag{2.16b}$$

$$A_{out}(L) = j\sqrt{\frac{\lambda_s}{\lambda_{out}}}\,\frac{\sqrt{\eta_{norm}P_{LO}}}{g}\exp(-\Delta\beta L/2)A_s^*(0)\sinh gL\,. \tag{2.16c}$$

The gain coefficient g is defined as

$$g = \sqrt{\eta_{norm}P_{LO} - \left(\frac{\Delta\beta}{2}\right)^2}\,. \tag{2.17}$$

The normalized efficiency η_{norm}, in general expressed in units of %/W-cm^2, is defined by

$$\eta_{norm} = \kappa_{eff,s}\kappa_{eff,out} = \frac{8\pi^2 d_{eff}{}^2}{n_{LO}n_s n_{out}c\varepsilon_0\lambda_s\lambda_{out}}\frac{1}{A_{eff}}\,. \tag{2.18}$$

The above parametric process enables operation at arbitrarily low input signal powers, preserves signal phase information and reverses signal chirp ($A_{out} \propto A_s^*$). By taking the square magnitude of equation (2.16c), we can obtain the power conversion efficiency of DFM expressed as

$$\eta \text{ (linear scale)} = P_{out}(L)\big/P_s(0) = \frac{\lambda_s}{\lambda_{out}}\frac{\eta_{norm}P_{LO}}{g^2}\sinh^2 gL \tag{2.19a}$$

$$\approx \frac{\lambda_s}{\lambda_{out}} \eta_{norm} L^2 P_{LO} \operatorname{sinc}^2(\frac{\Delta\beta L}{2}) \quad \text{(in the low gain limit: } \eta_{norm} L^2 P_{LO} < 1\text{)} \tag{2.19b}$$

$$\propto \frac{d_{eff}^2}{n^3} \frac{L^2}{A_{eff}} P_{LO} \operatorname{sinc}^2(\frac{\Delta\beta L}{2}) . \tag{2.19c}$$

Equation (2.19c) is another form of equation (1.1) and equation (1.2), emphasizing the relationship of conversion efficiency to material properties (d_{eff} and n), device geometry (A_{eff} and L), local oscillator power, and the phase mismatching term ($\operatorname{sinc}^2(\Delta\beta L/2)$). Since one of the most important parameters to describe the frequency-mixing process is the maximum achievable efficiency, we write the conversion efficiency η in dB under the phasematched condition ($\Delta\beta L = 0$) by

$$\eta \text{ (dB)} = 10\log\left(\frac{\lambda_s}{\lambda_{out}} \sinh^2\left(\sqrt{\eta_{norm} L^2 P_{LO}}\right)\right) \tag{2.20a}$$

$$\approx 10\log\left(\frac{\lambda_s}{\lambda_{out}} \eta_{norm} L^2 P_{LO} \right) . \quad \text{(in the low gain limit: } \eta_{norm} L^2 P_{LO} < 1\text{)} \tag{2.20b}$$

Waveguide Propagation Losses

The waveguide propagation loss usually is an important parameter for guided-wave nonlinear frequency mixing, as it causes efficiency reduction and some bandwidth broadening effects [16, 20]. When the waveguide propagation losses are not negligible, the nonlinear mixing efficiency η_{nl} can be related to the nonlinear mixing efficiency of a lossless, but otherwise identical, device ($\eta_{nl-lossless} = \eta_{norm} L^2$) by

$$\eta_{nl-lossy} / \eta_{nl-lossless} = e^{-(\alpha_{LO}+\alpha_s)L} \left(e^{\Delta\alpha L} - 1\right)^2 / \left(\Delta\alpha L\right)^2 , \tag{2.21}$$

where $\Delta\alpha = (\alpha_{LO} + \alpha_s - \alpha_{out})/2$ ($\Delta\alpha \sim \alpha_{LO}/2$ for near-degenerate DFM). To see the effect of waveguide propagation loss on the reduction of nonlinear mixing efficiency, we plot equation (2.21) under several conditions, as shown in figure 2.2.

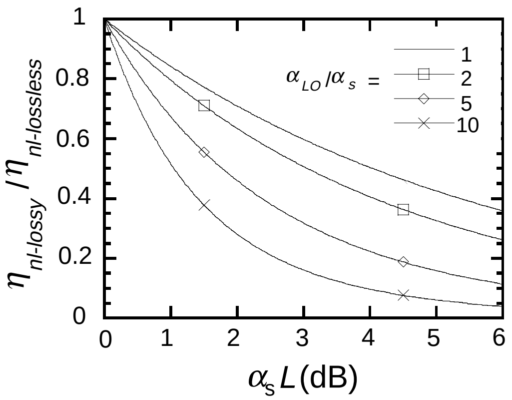

Figure 2.2 Reduction of nonlinear mixing efficiency normalized to the lossless case, versus $\alpha_s L$ for different values of α_{LO}/α_s. Loss contributes to a significant reduction of conversion efficiency.

Bandwidth

In frequency mixing the output power in the low gain limit is proportional to the phase mismatch $\mathrm{sinc}^2(\Delta\beta L/2)$ (referred to equation (2.19b)). To study the sensitivity of conversion efficiency to various parameters (wavelength, temperature, waveguide geometry, etc.), we can Taylor expand the phase mismatch as a function of an arbitrary parameter ξ as [19]

$$\Delta\beta L(\xi) = \Delta\beta L(\xi_0) + (\xi - \xi_0)\frac{d}{d\xi}\Delta\beta L(\xi_0) + (\xi - \xi_0)^2 \frac{d^2}{d\xi^2}\Delta\beta L(\xi_0) + \ldots\ldots \qquad (2.22)$$

At $\xi = \xi_0$, the interaction is phasematched. We define the bandwidth $\Delta\xi_{3dB}$ as the 3-dB bandwidth that occurs when $\mathrm{sinc}^2(x) = 1/2$ at $x = \pm 0.443\pi$. When the first-order term in the Taylor expansion dominates the phase mismatch, the 3-dB bandwidth is linearly proportional to the inverse of the interaction length as

$$\Delta\xi_{\mathrm{3dB}} = 1.772\pi \left| \frac{d}{d\xi}(\Delta\beta L) \right|^{-1}. \qquad (2.23)$$

In this situation, the phasematching restricts the range of efficient frequency mixing to within a narrow wavelength range. When the first-order term is zero in the Taylor expansion, the expansion is dominated by the second-order term, and the 3-dB bandwidth scales as the inverse square root of length:

$$\Delta\xi_{3\mathrm{dB}} = \sqrt{\frac{3.544\pi}{L}\left|\frac{\partial^2 \Delta\beta}{\partial \xi^2}\right|^{-1}} \quad . \tag{2.24}$$

Under certain circumstances, it is possible to design the waveguide geometry such that the first derivative of phasematching condition with respective to various parameters is equal to zero, resulting in a noncritical condition. In Chapter 3, we will describe a waveguide geometry that facilitates a condition insensitive to errors in the fabrication process by taking advantage of such a design. In Chapter 7, we will use the above equation to further study the bandwidth of $\chi^{(2)}$-based devices. More detailed description of tuning and tolerances of frequency-mixing processes can be found in reference 19.

2.3 Cascaded Second-Order Nonlinear Frequency Mixing ($\chi^{(2)}$:$\chi^{(2)}$ Mixing)

$\chi^{(2)}$:$\chi^{(2)}$ Mixing using Co-Propagating Beams

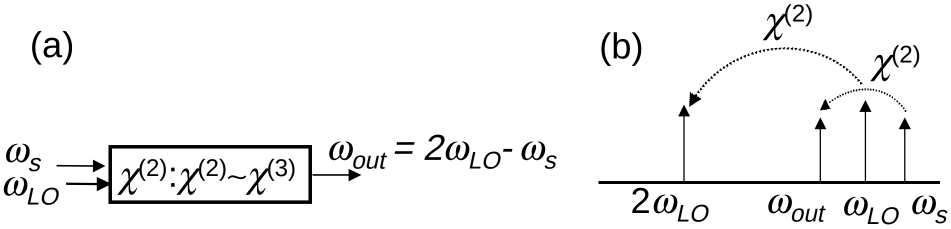

Figure 2.3 Schematic descriptions of a cascaded second-order nonlinear frequency mixing with *co-propagating* local oscillator and signal.

Nonlinear frequency mixing can also be carried out by use of a $\chi^{(2)}$:$\chi^{(2)}$ process [21, 22, 23, 24] where both local oscillator and signal are within the same band, and the interaction involves the cascading of second-harmonic generation (SHG) and DFM. We can classify the mixing processes as simultaneous $\chi^{(2)}$:$\chi^{(2)}$ mixing or discrete $\chi^{(2)}$:$\chi^{(2)}$ mixing. The simultaneous cascading process uses co-propagating local oscillator and signal. The schematic plot of such a conversion process is shown in figure 2.3. The local oscillator at frequency ω_{LO} is up-converted to frequency $2\omega_{LO}$ (ω_{SHG}) by SHG via the second-order nonlinear susceptibility $\chi^{(2)}$. Simultaneously the generated $2\omega_{LO}$ is mixed with the input signal ω_s to generate wavelength-shifted output ω_{out}=$2\omega_{LO}$ - ω_s by DFM via another $\chi^{(2)}$ process. Since all the input waves are within the same band ($\lambda_{LO} \approx \lambda_s \approx \lambda_{out}$ and $\lambda_{SHG} = \lambda_{LO}/2$) in this frequency-mixing process, $\kappa_{LO} \approx \kappa_s \approx \kappa_{out} \equiv \kappa$ and $\kappa_{SHG} = 2\kappa_{LO}$. The coupled-mode equations can be expressed as

$$\frac{\partial}{\partial z}A_{LO}+\frac{1}{v_{g_{LO}}}\frac{\partial}{\partial t}A_{LO}=-j\kappa A_{SHG}A_{LO}^{*}\exp(-j\Delta\beta_{SHG}z)-\frac{\alpha_{LO}}{2}A_{LO}\,, \tag{2.25a}$$

$$\frac{\partial}{\partial z}A_{SHG}+\frac{1}{v_{g_{SHG}}}\frac{\partial}{\partial t}A_{SHG}=-j\kappa A_{LO}A_{LO}\exp(j\Delta\beta_{SHG}z)$$

$$-j2\kappa A_{s}A_{out}\exp(j\Delta\beta_{DFM}z)-\frac{\alpha_{SHG}}{2}A_{SHG}(z,t), \tag{2.25b}$$

$$\frac{\partial}{\partial z}A_{s}+\frac{1}{v_{g_{s}}}\frac{\partial}{\partial t}A_{s}=-j\kappa A_{SHG}A_{out}^{*}\exp(-j\Delta\beta_{DFM}z)-\frac{\alpha_{s}}{2}A_{s}\,, \tag{2.25c}$$

$$\frac{\partial}{\partial z}A_{out}+\frac{1}{v_{g_{out}}}\frac{\partial}{\partial t}A_{out}=-j\kappa A_{SHG}A_{s}^{*}\exp(-j\Delta\beta_{DFM}z)-\frac{\alpha_{out}}{2}A_{out}\,, \tag{2.25d}$$

where phase mismatch is defined by $\Delta\beta_{SHG}=\beta_{SHG}-2\beta_{LO}$ and $\Delta\beta_{DFM}=\beta_{SHG}-\beta_{s}-\beta_{out}$. For such a mixing process, significant local oscillator depletion is required to convert the local oscillator to its harmonic wave $2\omega_{LO}$, which serves as the pump for the DFM process. Numerical analysis in general is used to solve these four coupled-mode equations. To get some insights into the conversion process, we derive the simplest analytic solution by assuming that the local oscillator depletion, waveguide propagation losses and group-velocity mismatch can be ignored, and a CW local oscillator is used. In such a situation, we write the conversion efficiency η in dB under the phasematched condition ($\Delta\beta L=0$) by

$$\eta\ (\mathrm{dB})\approx 10\log\left(\frac{1}{4}\eta_{norm}^{2}L^{4}P_{LO}^{2}\right).\ \ \text{(in the low gain limit: } \eta_{norm}L^{2}P_{LO}<1\text{)} \tag{2.26}$$

The conversion efficiency depends on the length of the device raised to the power of four due to the cascaded process, thus it is important to have a long device to achieve significant conversion efficiency. In practice, owing to the local oscillator depletion and waveguide propagation loss, the dependence on the length is less than the fourth power. The properties and bandwidth of the output in $\chi^{(2)}$:$\chi^{(2)}$ mixing are similar to those of direct DFM mixing, since the output is actually generated through the DFM process.

The above description ignores the possible direct interaction between the local oscillator and signal via sum-frequency generation. In general, it will happen only when the input signal is tuned too close to the local oscillator (i.e. within the narrow sum-frequency bandwidth <~0.5 nm). The complete equations for describing such interactions are given in reference 25.

$\chi^{(2)}$:$\chi^{(2)}$ Mixing using Counter-Propagating Beams

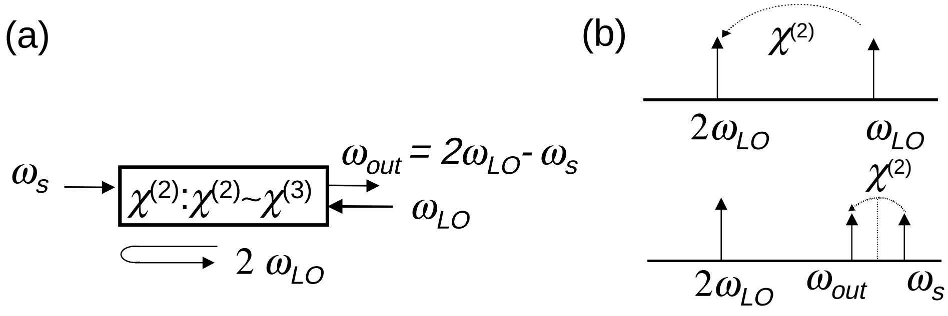

Figure 2.4 Schematic descriptions of cascaded second-order nonlinear frequency mixing with *counter-propagating* local oscillator and signal.

The discrete $\chi^{(2)}$:$\chi^{(2)}$ mixing also involves a SHG process and a DFM process, but both processes do not happen simultaneously since counter-propagating local oscillator and signal are used. A schematic plot of the mixing process is shown in figure 2.4. In such a process, the local oscillator is converted to a second harmonic (SH) wave, then the generated SH wave is reflected from the end of the waveguide and used as the pump for mixing with the input signal for output generation via a DFM process. The coupled-mode equations can be written as

SHG:

$$\frac{\partial}{\partial z}A_{LO} + \frac{1}{v_{g_{LO}}}\frac{\partial}{\partial t}A_{LO} = -j\kappa A_{SHG}A_{LO}^{*}\exp(-j\Delta\beta_{SHG}z) - \frac{\alpha_{LO}}{2}A_{LO}\,, \tag{2.27a}$$

$$\frac{\partial}{\partial z}A_{SHG} + \frac{1}{v_{g_{SHG}}}\frac{\partial}{\partial t}A_{SHG} = -j\kappa A_{LO}A_{LO}\exp(j\Delta\beta_{SHG}z) - \frac{\alpha_{SHG}}{2}A_{SHG}\,. \tag{2.27b}$$

DFM:

$$\frac{\partial}{\partial z}A_{SHG} + \frac{1}{v_{g_{SHG}}}\frac{\partial}{\partial t}A_{SHG} = -j2\kappa A_{s}A_{out}\exp(j\Delta\beta_{DFM}z) - \frac{\alpha_{SHG}}{2}A_{SHG}\,, \tag{2.28a}$$

$$\frac{\partial}{\partial z}A_{s} + \frac{1}{v_{g_{s}}}\frac{\partial}{\partial t}A_{s} = -j\kappa A_{SHG}A_{out}^{*}\exp(-j\Delta\beta_{DFM}z) - \frac{\alpha_{s}}{2}A_{s}\,, \tag{2.28b}$$

$$\frac{\partial}{\partial z}A_{out}+\frac{1}{v_{g_{out}}}\frac{\partial}{\partial t}A_{out}=-j\kappa A_{SHG}A_s^*\exp(-j\Delta\beta_{DFM}z)-\frac{\alpha_{out}}{2}A_{out}\,. \tag{2.28c}$$

By solving the SHG and DFM separately, we can get a solution for $\chi^{(2)}:\chi^{(2)}$ mixing with counter-propagating beams. In the limit of non-pump depletion and a lossless waveguide, one can get a stationary solution by use of the boundary condition. The power conversion efficiency can be expressed as

$$\eta\ \text{(linear scale)}=P_{out}/P_s=\frac{\lambda_s}{\lambda_{out}}\frac{\eta_{norm}P_{LO}}{g^2}\tanh^2\left(\sqrt{\eta_{norm}L^2P_{LO}}\right)\sinh^2(gL)\,. \tag{2.29}$$

We write the conversion efficiency η in dB (under the same assumption of equation (2.26)) as

$$\eta\ (\text{dB})\approx 10\log\left(\eta_{norm}^2L^4P_{LO}^2\right)\,.\qquad \text{(in the low gain limit:}\ \eta_{norm}L^2P_{LO}<1\text{)} \tag{2.30}$$

One major advantage of using counter-propagating beams is that the full length of the device is used twice and thus the interaction is more efficient than the co-propagating schemes.

2.4 Summary

In this chapter, we have developed coupled-mode equations for QPM guided-wave nonlinear frequency mixing, including difference-frequency mixing and cascaded second-order nonlinear frequency mixing. We have also discussed their simplified solutions to illustrate the dependence on several important parameters. The use of DFM requires a local oscillator (~780 nm) at roughly half of the signal wavelength for frequency mixing within the 1.5-µm-band. However, by use of $\chi^{(2)}:\chi^{(2)}$ mixing, a local oscillator wavelength within the 1.5-µm-band for 1.5-µm-band frequency mixing is allowed because it involves the cascading of SHG and DFM. Comparison of these different mixing schemes will be given in Chapter 5.

Reference for Chapter 2:

---

1. K. P. Petrov, A. T. Ryan, T. L. Patterson, L. Huang, S. J. Field, D. J. Bamford, “Spectroscopic detection of methane by use of guided-wave diode-pumped difference-frequency generation,” *Opt. Lett.* **23**, 1052-1054 (1998).
2. S. J. B. Yoo, “Wavelength conversion technologies for WDM network applications,” *J. Lightwave Technol*. **14**, 955-966 (1996).
3. M. H. Chou, J. Hauden, M. A. Arbore, and M. M. Fejer, “1.5-μm-band wavelength conversion based on difference frequency generation in $LiNbO_3$ waveguides with integrated coupling structures,” *Opt. Lett.* **23**, 1004-1006 (1998).
4. T. Suhara, H. Ishizuki, M. Fujimura, and H. Nishhara, “Waveguide quasi-phase-matched sum-frequency generation device for optical sampling,” *ECIO’99*, pp 501-504.
5. M. A. Arbore, M. H. Chou, M. M. Fejer, A. Galvanauskas, and D. Harter, “380-pJ-threshold optical parametric generator in periodically poled lithium niobate waveguides,” *ASSL’98*, PD paper.
6. A. Galvanauskas, K. K. Wong, K. El Hadi, M. Hofer, M. E. Fermann, and D. Harter; M. H. Chou, and M. M. Fejer, “Amplification in 1.2 to 1.7 μm communication window using OPA in PPLN waveguides,” *submitted to Electron. Lett.*
7. M. A. Arbore and M. M. Fejer, “Singly resonant optical parametric oscillation in periodically poled lithium niobate waveguides,” *Opti. Lett.* **22**, 151-153 (1997).
8. D. Hofrman. G. Shreiber, C. Hasse, H. Herrmann, R. Ricken, W. Sholer, “Continuous-wave mid-infrared optical parametric oscillators with periodically poled Ti:$LiNbO_3$ waveguides,” *ECIO’99*, Torino, Italy, PD paper.
9. R. W. Boyd, *Nonlinear Optics*, Academic Press, Boston, 1992.
10. Y. R. Shen, *The Principle of Nonlinear Optics*, Wiley, New York, 1983.
11. R. Syms and J. Cozens, *Optical Guided Waves and Devices*, McGraw-Hill, England, 1992.
12. H. Nishhara. M. Harauna, T. Suhara, *Optical Integrated Circuits*, McGraw-Hill, 1987.
13. D. Marcuse, *Theory of Dielectric Optical Waveguides*, Academic Press, Boston, 1991.
14. J. A. Armstrong, N. Bloembergen, J. Ducuing, and P. S. Pershan, “Interactions between light waves in a nonlinear dielectric,” *Phys. Rev. Lett.* **127**, 1918-1939 (1962).
15. P. A. Franken and J. F. Ward, “Optical harmonics and nonlinear phenomena,” *Rev. Mod. Phys.* **35**, 23-39 (1963).
16. R. L. Byer, “Parametric oscillators and nonlinear materials,” in *Nonlinear Optics*, P. G. Harper and B. S. Wherrett eds.(Academic, San Francisco, 1977), pp. 47-160.

---

17. R. A. Baumgartner and R. L. Byer, “Optical parametric amplification,” *IEEE J. Quantum Electron.* **15**, 432-444 (1979).
18. K. C. Rustagi, S. C. Mehendale, S. Meenakshi, “Optical frequency conversion in quasi-phase-matched stacks of nonlinear crystals,” *IEEE J. Quantum Electron.* **18**, 1029-1041 (1982).
19. M. M. Fejer, G. A. Magel, D. H. Jundt, R. L. Byer, “Quasi-phase-matched second harmonic generation: tuning and tolerances,” *IEEE J. Quantum Electron.* **28**, 2631-2654 (1992).
20. M. L. Bortz, S. J. Field, M. M. Fejer, D. W. Nam, R. G. Waarts, and D. F. Welch, “Noncritical quasi-phasematched second harmonic generation in an annealed proton exchanged $LiNbO_3$ waveguides,” *Trans. on Quantum Electron.* **30**, 2953 (1994).
21. G. I. Stegeman, D. J. Hagan, and L. Torner, “$\chi^{(2)}$ cascading phenomena and their applications to all-optical signal processing, mode-locking, pulse compression and solitons,” *Opt. and Quantum Electron.* **28**, 1691-1740 (1996).
22. K. Gallo and G. Assanto, “Analysis of lithium niobate all-optical wavelength shifters for the third spectral window,” *J. Opt. Soc. Am. B.* **16**, 741-753 (1999). K. Gallo, G. Assanto, G. I. Stegeman, “Efficient wavelength shifting over the erbium amplifier bandwidth via cascaded second order processes in lithium niobate waveguides,” *Appl. Phys. Lett.* **71**,1020-1022 (1997).
23. G. P. Banfi, P. K. Datta, V. Degiorgio, and D. Fortusini, “Wavelength shifting and amplification of optical pulses through cascaded second-order processes in periodically poled lithium niobate,” *Appl. Phys. Lett.* **7**,136-138 (1998).
24. M. H. Chou, I. Brener, M. M. Fejer, E. E. Chaban, and S. B. Christman, “1.5-µm-band wavelength conversion based on cascaded second-order nonlinearity in $LiNbO_3$ waveguides,” *Photon. Technol. Lett.* **11**, 653-655 (1999).
25. Coupled-mode equations for cascaded second-order nonlinear frequency mixing including sum-frequency generation:

$$\frac{\partial}{\partial z}A_{LO} = -j\kappa A_{SHG}A_{LO}^{*}\exp(-j\Delta\beta_{SHG}z) - j\kappa A_{SFG1}A_{s}^{*}\exp(-j\Delta\beta_{SFG1}z)$$

$$- j\kappa A_{SFG2}A_{out}^{*}\exp(-j\Delta\beta_{SFG2}z) - \frac{\alpha_{LO}}{2}A_{LO}$$

$$\frac{\partial}{\partial z}A_{SHG} = -j\kappa A_{LO}A_{LO}\exp(j\Delta\beta_{SHG}z) - j2\kappa A_{s}A_{out}\exp(j\Delta\beta_{DFM}z) - \frac{\alpha_{SHG}}{2}A_{SHG}$$

$$\frac{\partial}{\partial z}A_{s} = -j\kappa A_{SHG}A_{out}^{*}\exp(-j\Delta\beta_{DFM}z) - j\kappa A_{SFG1}A_{LO}^{*}\exp(-j\Delta\beta_{SFG1}z) - \frac{\alpha_{s}}{2}A_{s}$$

$$\frac{\partial}{\partial z}A_{out} = -j\kappa A_{SHG}A_{s}^{*}\exp(-j\Delta\beta_{DFM}z) - j\kappa A_{SFG2}A_{LO}^{*}\exp(-j\Delta\beta_{SFG2}z) - \frac{\alpha_{out}}{2}A_{out}$$

$$\frac{\partial}{\partial z}A_{SFG1} = -j2\kappa A_{LO}A_{s}\exp(j\Delta\beta_{SFG1}z) - \frac{\alpha_{SFG1}}{2}A_{SFG2}$$

$$\frac{\partial}{\partial z} A_{SFG2} = -j2\kappa A_{LO} A_{out} \exp(j\Delta\beta_{SFG2} z) - \frac{\alpha_{SFG2}}{2} A_{SFG2}$$

CHAPTER 3

DESIGN AND FABRICATION OF APE-PPLN WAVEGUIDES

3.1 Introduction

Waveguide confinement can increase the single-pass nonlinear mixing efficiency by a factor up to 1000, as compared to bulk media. In order to demonstrate efficient OF mixers, suitable materials with appropriate microstructured nonlinearity to achieve quasi-phasematching (QPM) and techniques to fabricate homogeneous low-loss waveguides are required. Ferroelectric oxides and semiconductors are two potential candidates that satisfy these criteria [1, 2, 3, 4]. Patterned semiconductors (laterally orientation-patterned AlGaAs films) currently suffer from high propagation losses. However, with advances in the fabrication processes, they will be important for future applications [5]. In this work, we chose to use $LiNbO_3$ to demonstrate efficient OF mixers because of the availability of periodically-poled-$LiNbO_3$ (PPLN) material and waveguide fabrication techniques in this kind of substrate. With improvements in both full-wafer PPLN and waveguides, devices with nonlinear mixing efficiency of ~750%/W were developed in this work. This chapter describes the design and fabrication of annealed proton-exchanged (APE) PPLN waveguides for telecommunication applications.

3.2 Fabrication of Periodically Poled $LiNbO_3$ for Waveguide Applications

PPLN has been well developed [6, 7, 8, 9, 10, 11], however, most developed recipes are not optimized for fabricating PPLN waveguides. For waveguide applications, it is crucial that the fabrication process does not degrade the surface quality, because the waveguide is only a few microns under the wafer surface. Chemical reduction, contamination, or surface damage of PPLN wafers will result in excess waveguide propagation losses or induce unwanted phasematching effects. Contamination or surface damage can occur during the preparation of patterned electrodes or during the poling process. For example, deposition of metal electrodes (such as nichrome or aluminum) will cause metal in-diffusion into the wafer surface. A thin photoresist film on the wafer surface, due to under-development in the photolithography process, will cause surface damage when high voltage is applied. Another important criterion for high quality PPLN waveguides is the waveguide homogeneity, which is crucial for keeping the phasematching conditions over the whole interaction length. Thus, a full-wafer fabrication process is required.

To fabricate PPLN for waveguide applications, we have improved the reported recipe to obtain high quality 3-inch-diameter PPLN wafers suitable for telecommunication OF mixers, which require QPM periods of 10-20 µm. A schematic description of the APE-PPLN waveguide fabrication process used in this work is shown in figure 3.1. Figure 3.1(a) shows the major steps for the 3-inch-diameter PPLN wafer fabrication, which consists of electrode patterning through standard photolithographic processing and electric field poling through high voltage (11 kV over a 500-µm-thick wafer). The important processing parameters used to obtain the PPLN wafer are described below. Figure 3.1(b) shows the major steps for fabricating APE waveguide in PPLN, which will be described in the next section.

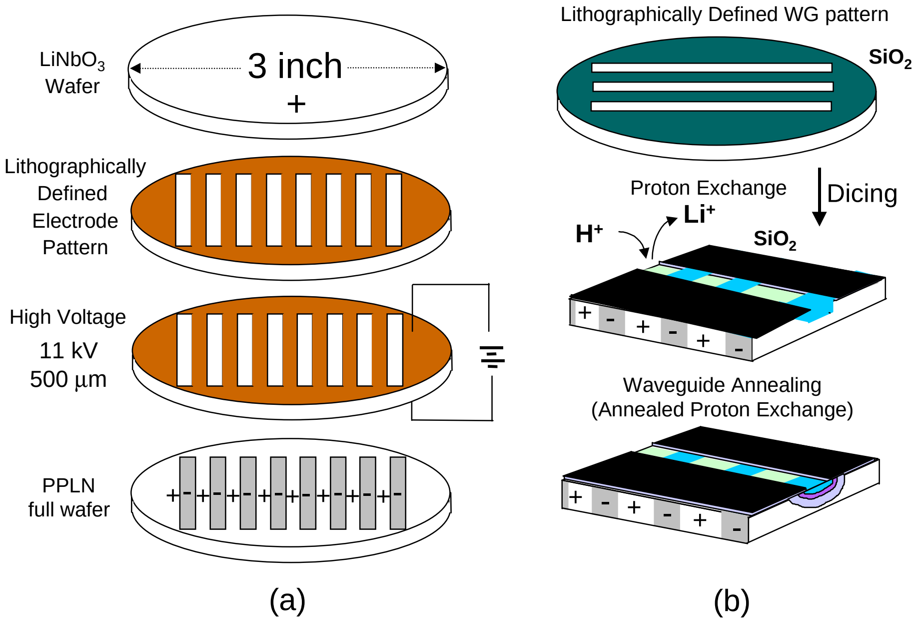

Figure 3.1 A schematic description of APE-PPLN waveguide fabrication. (a) PPLN fabrication; (b) APE waveguide fabrication.

The +*z* face of an optical grade *z*-cut $LiNbO_3$ wafer was patterned to define the poling electrodes through single-step lithographic processing by use of photoresist AZ4620P. The photoresist AZ4620P has a very high dielectric strength, thus it is a good high voltage insulator when post-baked at a temperature of ~150 °C. The thickness of the photoresist is 4-5 microns after the post-baking. In designing the photolithography mask, a better optimization is generally achieved by keeping the electrode linewidth slightly narrower (~0.75 µm) than the theoretical prediction [9], because the high temperature post-baking process will shrink the photoresist and result in an offset between the designed electrode linewidth and the processed result. To avoid unwanted domains from pyroelectric effects before high voltage poling, the temperature ramp rate for photoresist baking is kept at about 20-30 °C/hour and a metal mask is used to ground the surface during the cooling process when the temperature is down to ~100 °C.

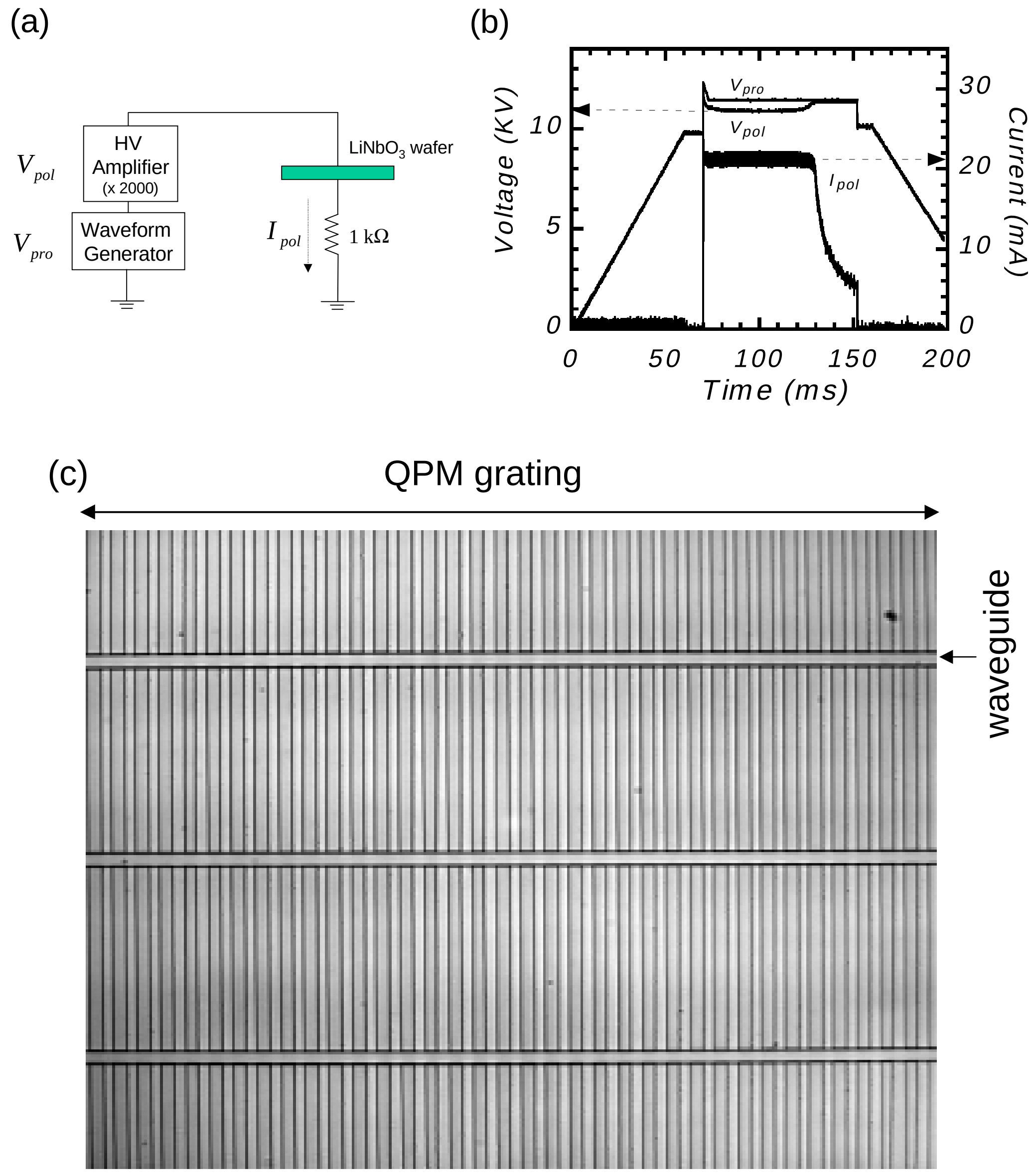

Figure 3.2 (a) Electric field poling circuit. (b) Typical voltage and current waveforms. V_{pro} is the programmed waveform through waveform generator, V_{pol} is the poling waveform, which is the voltage across the wafer, and I_{pol} is the current flowing through the wafer. (c) Etched +z surface of a PPLN wafer with a period of 14.75 microns and etched 11.5-µm wide APE-channel waveguides.

The poling process is operated with a standard voltage waveform [9, 11], which consists of a nucleation spike at a voltage of ~23-24 kV/mm followed by a constant voltage of ~22 kV/mm. It is operated at the nominal current limit region (I_{pol}~21.5 mA), limited by the current source of the high voltage amplifier. The charge Q transferred to the sample to compensate the inversion of the spontaneous polarization is given by

$$Q = \int I_{pol}\,dt = 2P_{spon}A_{pol} \ , \tag{3.1}$$

where P_{spon}=78 μC/cm^2 is the spontaneous polarization of LiNbO$_3$, A_{pol} is the area of inversion region, and the factor 2 accounts for the polarity reversal. The electrolyte used was a saturated solution of lithium chloride in deionized water. Figure 3.2(a) shows the circuit used in the experiments. A Trek model 20/20 high voltage amplifier driven by a SRS DS345 arbitrary waveform generator was used for the high voltage source. The source was connected directly to the sample. A 1-kΩ resistor was used in the ground-return to measure the poling current flowing through the sample. The poling voltage was measured through a (÷2000) voltage monitor of the high voltage amplifier. Figure 3.2(b) shows the typical experimental poling voltage waveform and current trace recorded by an oscilloscope (voltages are scaled by 2000 times in the figure). The results conform with the self-terminating model as predicted by Miller [11]. Figure 3.2(c) shows the domains in the +z surface of a wafer with a period of 14.75 microns, where domains were revealed using hydrofluoric acid at room temperature for about 5 minutes. Figure 3.2(c) also shows the APE-channel waveguide structure with a waveguide width of 11.5 μm, where waveguides are also revealed using hydrofluoric acid.

3.3 Design and Fabrication of Annealed Proton-Exchanged Waveguides in PPLN

APE waveguides have several important applications in linear and nonlinear optical devices, such as electro-optic modulators or nonlinear frequency converters. The fabrication process of APE waveguides has been established [12, 13, 14, 15, 16]. However, the demonstrated results have not shown high nonlinear frequency-conversion efficiencies in telecommunication bands, partially because of the difficulty in fabricating long waveguides with good homogeneity. Key parameters important to high quality nonlinear waveguides include waveguide homogeneity, mode overlap among the interacting waves, and low waveguide propagation losses. The dependence of the nonlinear mixing efficiency on these parameters was described in Chapter 2**.** In addition, the power-handling capability of the nonlinear waveguides is also important in several applications. In this section, we will describe several practical issues and optimization of these parameters.

Waveguide Fabrication

The major fabrication steps for APE waveguides used in this work are shown in figure 3.1(b), including the lithography process for defining waveguide channels, proton exchange (H^+ in exchange with Li^+ of $LiNbO_3$) to induce a step-index increase, and thermal annealing for proton in-diffusion to form a final waveguide. We used a 1000-Å sputtered SiO_2 film as waveguide mask (SiO_2 can be etched by buffered oxide etch (BOE) to open waveguide channels). The proton exchange was performed in a benzoic acid melt at 160 °C, and thermal annealing was performed at a temperature of ~330 °C. A step concentration profile is assumed for the proton exchanged layer. The proton-exchange depth (d_e) was calculated based on a reported concentration independent equation [13]:

$$d_e = \sqrt{4D_e(T_e)t_e}\ , \tag{3.2}$$

where t_e is the duration of the proton exchange process. $D_e(T_e)$ is the effective diffusion coefficient defined by

$$D_e(T_e) = D_{e,0}\exp(-E_e/kT_e). \tag{3.3}$$

T_e and k are the absolute proton-exchange temperature and the Boltzman constant, respectively. $D_{e,0}$=1.84x10^9 μm^2/hr and E_e=0.974 eV for the z-cut $LiNbO_3$. Thermal annealing was performed at a temperature of ~330 °C. The annealing process was modeled based on a two-dimensional diffusion equation, with a reported concentration-dependent diffusion coefficient [14, 16], given by

$$\frac{dC'}{dt} = \frac{d}{dx}\left[D_a(C')\frac{dC'}{dx}\right] + \frac{d}{dy}\left[D_a(C')\frac{dC'}{dy}\right]. \tag{3.4}$$

C' is the H^+-concentration normalized to its initial value after proton exchange (i.e., C'=1 for PE-$LiNbO_3$), and

$$D_a(T_a, C') = D_{a,0}\exp(-E_a/kT_a)\left[a + (1-a)\exp(-bC')\right], \tag{3.5}$$

where $D_{a,0}$=1.357x10^8 μm^2/hr, E_a=1 eV, a=0.1, and b=12. T_a is the absolute annealing temperature.

Waveguide Propagation Losses

Proton exchange of $LiNbO_3$ forms a chemical composition of $H_xLi_{1-x}NbO_3$ (x~0.67) and generates a step-like index profile with a large increase in the extraordinary refractive index (Δn_e~0.1) [12, 13]. However, the nonlinearity of $LiNbO_3$ vanishes in the initial exchanged region (so-called *dead layer*) [17, 18]. In addition, the $H_xLi_{1-x}NbO_3$ (x~0.67) is in a β–phase (or possibly in a γ-phase) where the waveguide propagation loss is relatively high (~2 dB/cm). Thus the initial exchange structure is not suitable for nonlinear frequency mixing. Subsequent annealing processes will cause a phase transition of $H_xLi_{1-x}NbO_3$, partial recovery of the nonlinearity in the dead layer, and reduction of the hydrogen concentration in the film with a graded index profile and lower refractive index. The annealing process will initially increase the waveguide propagation losses, possibly due to the co-existence of multi-phases (mixture of α– and β–phases, 0.12<x<0.55) or other high loss phases [19, 20]. Further annealing will reduce the propagation losses to produce waveguides in a low loss (<0.4 dB/cm) α–phase (x<0.12) with $\Delta n_e \leq 0.03$.

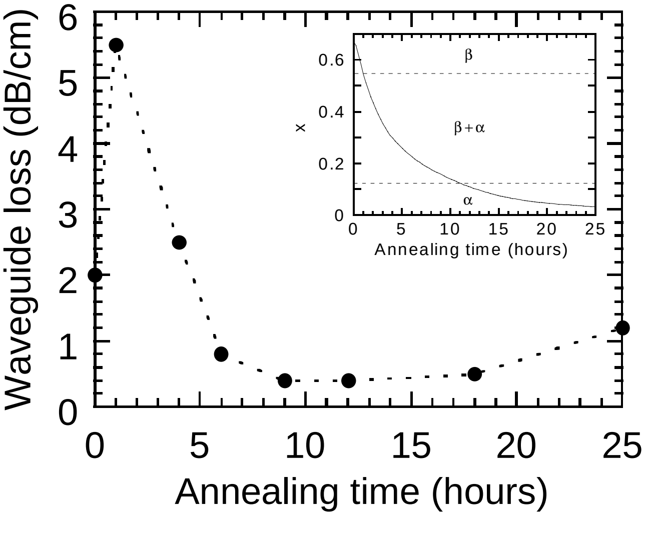

Figure 3.3 Measured waveguide propagation losses vs. annealing time. The inset shows the calculated proton concentration at the surface of the wafer, x, in $H_xL_{1-x}NbO_3$ vs. annealing time. x=0.67 is assumed for the un-annealed case; the phase structures are referred from reference 19.

To study waveguide propagation losses vs. annealing, we fabricated devices and measured the losses by the Fabry-Perot [21] method using a 1.3-μm laser. Samples with a proton-exchanged depth of 0.4 μm and a waveguide width of 5 μm were annealed at 333 °C. Figure 3.3 shows the measured results and the inset shows the calculated index-height versus annealing time and the possible phase structure inferred from the approximate phase diagram [19]. Although the actual phase and waveguide propagation losses depend on the detailed fabrication conditions (such as proton-exchange, annealing temperature, etc.), the above simplified argument on concentration range can be used as a useful guide to obtain low-loss nonlinear waveguides. Besides the volume inhomogeneities in the proton-exchanged material, another possible mechanism for waveguide propagation losses is considered to be scattering owing to the irregularly shaped waveguide-side walls [22].

Another readily available technique for fabricating low-loss waveguides in $LiNbO_3$ is use of titanium-diffused waveguides. Waveguide propagation loss of $Ti:LiNbO_3$ waveguides below 0.1 dB/cm has been reported [23, 24], though typically for rather loosely confining waveguides. There is no surface dead layer induced by the titanium-diffusion process. High quality Ti-PPLN waveguides for frequency conversion have been reported recently [23, 24]. However, the typical increase of surface refractive index is below 0.01, which limits the possibility to have a high normalized efficiency. In addition, $Ti:LiNbO_3$ waveguides require high processing temperature (~1000 °C) and are more sensitive to photorefractive effects than are $H:LiNbO_3$ waveguides [25]. Currently there are several other $H:LiNbO_3$ fabrication techniques under development by other researchers, including soft (diluted) proton exchange (by use of benzoic acid/lithium benzoate melts) [26, 27] and vapor phase exchange [28]. The key feature of those processes is the control of the proton exchange concentration to achieve the low-loss α–phase, with almost no structural change through the waveguide. The results show several attractive properties, such as low waveguide losses (<0.35 dB/cm), high refractive index increase (~0.03), higher optical damage threshold than APE waveguides, and no dead layer. Other attractive waveguide fabrication processes include Zn-diffused waveguides, which show high resistance to photorefractive effects [29]. Those processes are potentially important for fabricating high quality PPLN waveguides in the future. To make devices with good quality by use of those processes, further characterization and waveguide modeling are required.

Waveguide Homogeneity and Noncritical Design

The conversion efficiency in lossless waveguides is proportional to the square of the interaction length. However, fabricating long homogeneous waveguides demands tight control of the waveguide processing parameters, which include the proton exchange temperature, waveguide annealing temperature, and homogeneity of waveguide lithography. For a 50-mm interaction length, the temperature homogeneity requirement for a critical design could be as tight as ± 0.015 °C for proton exchange and ± 0.025 °C for annealing; the waveguide width variation should be kept to less than ± 12.5 nm.

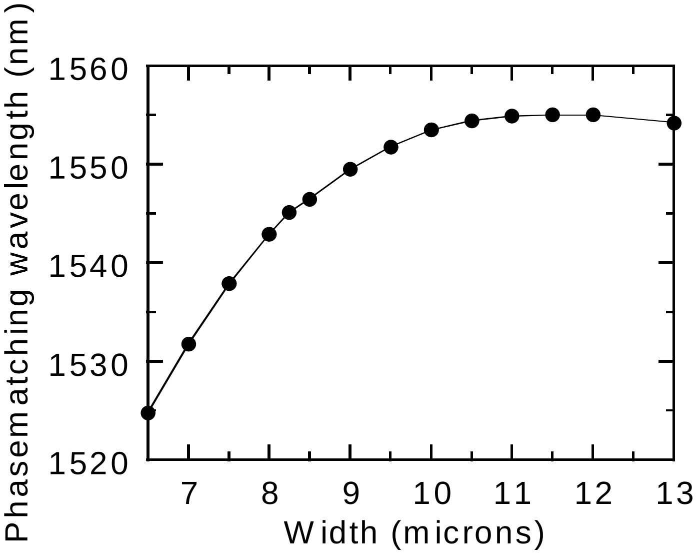

Figure 3.4 Measured phasematching wavelength vs. waveguide width. At a waveguide (mask) width of ~11.5 μm, the first derivative of the phasematching wavelength with respect to waveguide width is zero. This property loosens the requirements on uniformity of lithographic patterning.

The tight requirements on waveguide width can be alleviated by designing the waveguide geometry such that the first derivative of the phasematching condition with respect to waveguide width equals to zero (i.e. the first-order term in the Taylor expansion of equation (2.22) is zero). Such kinds of noncritical conditions thus loosen the tight requirements for waveguide lithography. Noncritical design has been investigated by several researchers [30, 31]. Most experimental results focused on the interaction of the fundamental mode (TM_{00}) of the fundamental wavelength and the first high-order mode (TM_{01}) of its harmonic waves. The advantages of those interactions will be discussed later in this section. In this work, we designed and fabricated noncritical waveguides for interaction of the fundamental modes (TM_{00}) of 780 nm and 1560 nm, using the linear and nonlinear model developed by Bortz [13]. Such interactions allow for launching the fundamental mode of the local oscillator into the waveguide through an adiabatic taper, which is easier compared with launching the TM_{01} mode. The waveguides were fabricated by proton exchange using benzoic acid at 160 °C for ~15 hours, to a depth of ~0.7 microns, then annealing at 325 °C for 26 hours. Figure 3.4 shows the measured phasematching wavelength vs. waveguide width. For a waveguide (mask) width of ~11.5 microns, the phasematching wavelength is insensitive to small width perturbations. Figure 3.5 shows a near-ideal tuning curve for a 50-mm-long device, with peak normalized efficiency of ~700%/W. A more efficient device with a 56-mm-long interaction length and peak normalized efficiency of 750%/W has also been fabricated. The waveguide propagation loss is ~0.35 dB/cm at wavelength of 1550 nm. The above design gives a waveguide that contains 2-3 modes at 1550 nm. To launch the input radiation into the desired fundamental mode and increase the fiber-waveguide coupling efficiency, tapered waveguides at the input and output are used (discussed in Chapter 4).

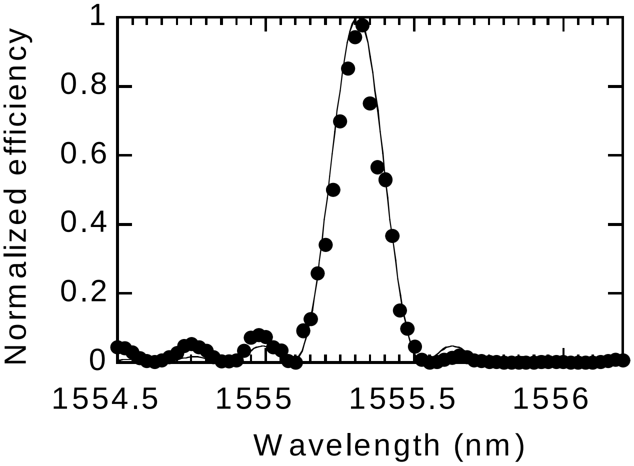

Figure 3.5 Wavelength-tuning curve of a 50-mm-long waveguide. The solid circles are measured results; the solid line is the theoretical fitting to an ideal sinc^2 curve (~7% wider than the theoretical prediction). The peak normalized efficiency is ~700%/W.

Modal Overlap

Normalized efficiency is a function of the overlap of the interacting modes with each other and with the material nonlinearity. APE-PPLN waveguides have non-symmetric modes in the depth direction and generate a layer (dead layer) without nonlinearity. Thus, mixing in the fundamental mode for both the long wavelength and short wavelength does not necessarily yield the best efficiency. In addition, the existence of the dead layer limits designs using tightly confined modes. Instead, the interaction of the TM_{00} mode at the long wavelength and the first high-order (TM_{01}) depth mode at the short wavelength gives better modal overlap, and takes advantage of the existence of the dead layer [31, 32]. Such mode mixing has been studied, and the results show that a noncritical phasematching condition can also be achieved with proper design. Another advantage of such an interaction is the lower dispersion and thus ~30% wider acceptance-bandwidth than obtained with the TM_{00} mode at 1550 nm and the TM_{00} mode at its harmonic, due to the similarity of the TM_{00} mode at 1550 nm and the TM_{01} mode at its harmonic. In ultra-short pulse applications, where group-velocity mismatch limits the device interaction length, such mode mixing can allow 10-20% longer interaction length.

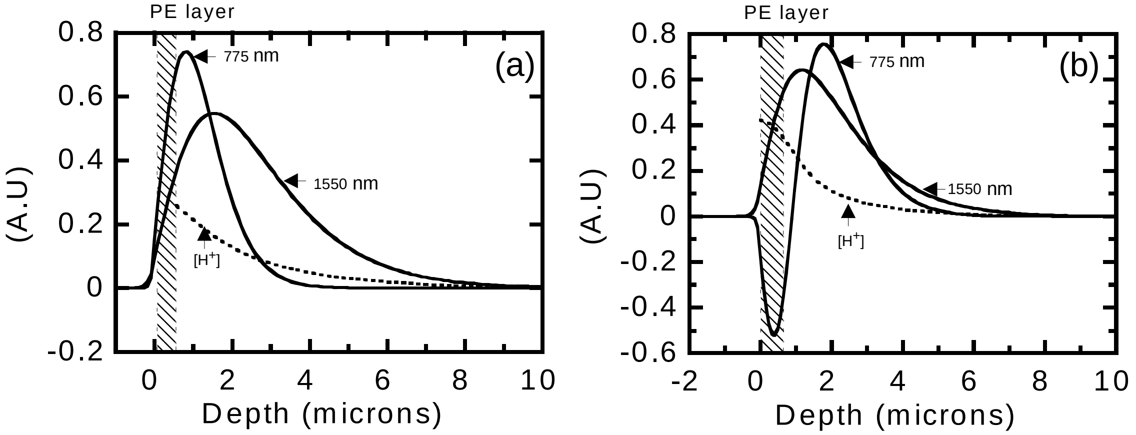

Figure 3.6 (a) Calculated TM_{00} field profiles at 1550 nm and its harmonic wavelength and H^+-concentration distribution in the depth direction. (b) Calculated TM_{00} field profile at 1550 nm, TM_{01} field profile at 775 nm, and H^+-concentration distribution in the depth direction. Note the overlap of the negative lobe of the TM_{01} mode with the "dead layer", eliminating the usual cancellation in the overlap integral.

For comparison, we plot the general profiles of different modes in the depth direction. Figure 3.6(a) shows the calculated TM_{00} field profiles at 1550 nm and its harmonic wavelength and H^+-concentration distribution in the depth direction. The waveguide has a PE-width of 12 μm and is fabricated by proton exchange using benzoic acid at 160 °C for about 15 hours to a depth of ~0.71 microns, then annealed at 325 °C for 26 hours. Figure 3.6(b) shows the calculated TM_{00} field profile at 1550 nm, TM_{01} field profile at 775 nm, and H^+-concentration distribution in the depth direction. The waveguide has a PE-width of 5 μm and is fabricated by proton exchange using benzoic acid at 160 °C for about 18.9 hours to a depth of ~0.8 microns, then annealed at 325 °C for 20 hours. The main challenge to fabricate highly efficient waveguides via high-order mode interaction is the trade-off between the mode overlap and waveguide propagation losses, since optimization of mode overlap generally requires a short annealing time. The mode overlap can also be possibly further increased by use of a high-index cladding layer, which has been reported in reference 33.

Device Stability and Power-Handling Capability

$LiNbO_3$ is sensitive to photorefractive effects at room temperature, where electric fields due to photo-generated carriers induce refractive index changes. Photorefractive effects shift the phasematching wavelength and reduce the device efficiency by destroying the phasematching condition ($\Delta\beta(z) \neq 0$). Such effects are especially serious at visible wavelengths and are enhanced in waveguide devices due to their high optical intensity. It is well known that photorefractive effects in $LiNbO_3$ can be reduced when operated at elevated temperatures. To study the power and temperature dependence of such effects in our APE-PPLN waveguide device, we measured the second-harmonic generation (SHG) tuning curves under a variety of conditions, as shown in figure 3.7. The waveguide has a 40-mm interaction length. A 1.5-μm external cavity laser (ECL) amplified by a high power erbium-doped-fiber amplifier (EDFA) was used as the pump (fundamental wavelength). When devices are operated at room temperature and high power condition (100-200 mW; intensity~100 MW/cm^2), photorefractive effects shift the phasematching wavelength relative to that at low power operation, distort the wavelength-tuning curve, and limit the conversion efficiency. In the phasematched and high power conditions, the optical intensities at fundamental wavelengths and its harmonic are ~100 MW/cm^2 and ~10 MW/cm^2, respectively. When the devices are operated at ~120 °C, such effects are dramatically reduced. The phasematching wavelength was slightly shifted up relative to the low power conditions, but the device is stable and efficient even at powers above 200 mW.

By improving waveguide fabrication processes, the sensitivity to photorefractive effects of $LiNbO_3$ devices can be reduced. We observed substantial reduction of those effects in a sample annealed in an O_2 atmosphere, and suspected that some amount of the photorefractive sensitivity was coming from the reduction of $LiNbO_3$ material caused by thermal cycling during sample preparation. The effects can be eliminated by using MgO-doped $LiNbO_3$ [34] or Zn-diffused $LiNbO_3$ waveguides [29]. Several orders of magnitude improvements in photorefractive effects have been observed in these materials, providing the possibility for devices operating at room temperature.

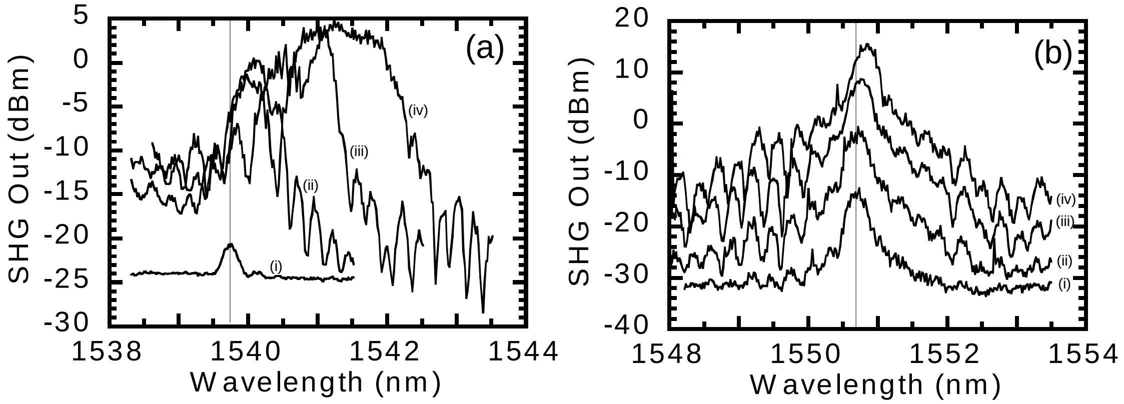

Figure 3.7 Measured SHG tuning curve in a logrithemic scale at several fundamental powers (a) at room temperature (i: 3 mW, ii: 35 mW, iii: 65 mW, iv: 80 mW); (b) at 120

°C. (i: 3 mW, ii: 35 mW, iii: 105 mW, iv: 216 mW). The line indicates the phasematching wavelength at low power condition.

3.4 Summary

In this chapter, we have described the basic APE-PPLN waveguide fabrication process and discussed several important parameters for device optimization. Fabrication of high quality PPLN waveguides requires full-wafers with high fidelity domains and clean surfaces. Key parameters important to high quality nonlinear waveguides include waveguide homogeneity over long lengths, mode overlap among the interacting waves, and low waveguide propagation losses. Another important issue is the device power-handling capacity, mainly limited by photorefractive effects in PPLN waveguides. Further detailed study on this issue will be required. APE-PPLN waveguides developed in this work give nonlinear mixing efficiency up to 750%/W. Several other waveguide fabrication techniques with potential importance currently are under development by other researchers. Advances in PPLN waveguide fabrication can possibly increase efficiencies by an order of magnitude in the future.

Reference for Chapter 3:

---

1. R. L. Byer, “Parametric oscillators and nonlinear materials,” in *Nonlinear Optics*, P. G. Harper and B. S. Wherrett eds. (Academic, San Francisco, 1977), pp. 47-160.
2. R. L. Byer, “Quasi-phase matched nonlinear interactions and devices,” *J. Nonlinear Optical Physics & Materials* **6** (4), 549-591 (1997).
3. P. F. Bordui and M. M. Fejer, “Inorganic crystals for nonlinear optical frequency conversion,” *Annu. Rev. Mater. Sci.* **23**, 321-379 (1993).
4. A. M. Prokhorov and Y. S. Kuz’minov, *Physics and Chemistry of Crystalline Lithium Niobate*, (Adam Hilger, Bristol, 1990).
5. L. A. Eyres, C. B. Ebert, M. M. Fejer, J. S. Harris, “MBE growth of laterally antiphase-patterned GaAs films using thin Ge layers for waveguide mixing,” *CLEO’98*, CWH4.
6. M. Yamada, N. Nada, M. Saitoh, K. Watanabe, “First-order quasi-phased matched $LiNbO_3$ waveguide periodically poled by applying an external field for efficient blue second-harmonic generation,” *Appl. Phys. Lett.*, **62**, 435-436 (1993).
7. J. Webjorn, V. Pruneri, P. S. J. Russell, J. R. M. Barr, D. C. Hanna, “Quasi-phase-matched blue light generation in bulk lithium niobate, electrically poled via periodic liquid electrodes,” *Electron. Lett*, **30**, 894-895 (1994).
8. L. E. Myers, R. C. Eckardt, M. M. Fejer, R. L. Byer, W. R. Bosenberg, and J. W. Pierce, “Quasi-phase-matched optical parametric oscillators in bulk periodically poled $LiNbO_3$,” *Opt. Soc. Am. B* **12**, 2102-2116 (1995).
9. G. D. Miller, R. G. Batchko, M. M. Fejer, and R. L. Byer, “Visible quasi-phase-matched harmonic generation by electric-field-poled lithium niobate,” *Proc. SPIE* **2700**, 34-45 (1996).
10. L. E. Myers, “Quasi-phasematched optical parametric oscillators in bulk periodically poled lithium noibate,” Ph.D. Dissertation, Department of Electrical Engineering, Stanford University, Stanford, CA (1995).
11. G. D. Miller, “Periodically poled lithium niobate: modeling, fabrication, and nonlinear optical performance,” Ph.D. Dissertation, Department of Electrical Engineering, Stanford University, Stanford, CA (1998).
12. J. L. Jackel, C. E. Rice, J. J. Veselka, “Proton exchange for high-index waveguides in $LiNbO_3$,” *Appl. Phys. Lett.* 41, 607-608 (1982).
13. D. F. Clark, A. C. G. Nutt, K. K. Wong, P. J. R. Laybourn, R. M. De La Rue, “Characterization of proton-exchange slab optical waveguides in z-cut $LiNbO_3$,” *J. Appl. Phys*. **54**, 6218-6220 (1983).
14. M. L. Bortz, and M. M. Fejer, “Annealed proton-exchanged $LiNbO_3$ waveguide,” *Opt. Lett*. **16**, 1844-1846 (1991).

15. E. J. Lim, “Quasi-phasematching for guided-wave nonlinear optics in lithium niobate,” Ph.D. Dissertation, Department of Electrical Engineering, Stanford University, Stanford, CA (1992).

16. M. L. Bortz, “Quasi-phasematched optical frequency conversion in lithium niobate waveguides,” Ph.D. Dissertation, Department of Applied Physics, Stanford University, Stanford, CA (1994).

17. T. Suhara, H. Tazaki, H. Nishihara, “Measurement of reduction in SHG coefficient of $LiNbO_3$ by proton exchanging,” *Electron. Lett*. **25**, 1326-1328 (1989).

18. M. L. Bortz, L. A. Eyres, and M. M. Fejer, “Depth profiling of the d_{33} nonlinear coefficient in annealed proton exchanged $LiNbO_3$ waveguides,” *Appl. Phys. Lett.* **62**, 2012-2014 (1993).

19. C. E. Rice, “The structure and properties of $Li_{1-x}H_xNbO_3$,” *J. Solid State Chem.* **64**, 188-199 (1986).

20. Yu. N. Korkishko, V. A. Fedorov, M. P. De Micheli, P. Baldi, K. E. Hadi, A. Leycuras, “Relationships between structural and optical properties of proton-exchanged waveguides on Z-cut lithium niobate,” *Appl. Opt.* **35**, 7056-7060 (1996).

21. R. Regener and W. Sohler, “Loss in low-finesse Ti:$LiNbO_3$ optical waveguide resonators,” *Appl. Phys.* ***B*** **36**, 143-147 (1985).

22. K. Yamamoto, K. Mizuuchi, and T. Taniuchi, “Low-loss waveguides in MgO:$LiNbO_3$ and $LiTaO_3$ by pyrophosphoric acid proton exchange,” *Jpn. J. Appl. Phys.* **31**, 1059-1064 (1992).

23. D. Hofmann. G. Shreiber, C. Hasse, H. Herrmann, R. Ricken, W. Sohler, “Mid-infrared difference-frequency generation in periodically poled Ti:$LiNbO_3$ channel waveguides,” *Opt. Lett.* **24**, 896-898 (1999).

24. D. Hofmann. G. Shreiber, C. Hasse, H. Herrmann, R. Ricken, W. Sohler, “Continuous-wave mid-infrared optical parametric oscillators with periodically poled Ti:$LiNbO_3$ waveguides,” *ECIO’99*, Torino, Italy, PD paper (1999).

25. T. Fujiwara, R. Srivastava, X. Cao, R. V. Ramaswamy , “Comparison of photorefractive index change in proton-exchanged and Ti-diffused $LiNbO_3$ waveguides,” *Opt. Lett.* **18**, 346-348 (1993).

26. P. G. Suchoski, T. K. Findakly, F. J. Leonberger, “Stable low-loss proton-exchanged $LiNbO_3$ waveguide devices with no electro-optic degradation,” *Opt. Lett.* **13**, 1050-1052 (1988).

27. K. El Hadi, V. Rastogi, M. R. Shenoy, K. Thyagarajan, M. De Micheli, D. B. Ostrowsky, “Spectral measurement of the film-substrate index difference in proton-exchanged $LiNbO_3$ waveguides,” *Appl. Opt.* **37**, 6463-6467 (1998).

28. J. Rams, J. M. Cabrera, “Preparation of proton-exchange $LiNbO_3$ waveguides in benzoic acid vapor,” *J. Opt. Soc. Am. B* **16**, 401-406 (1999). J. Rams, J. M. Cabrera, “Nonlinear optical efficient $LiNbO_3$ waveguides proton exchanged in benzoic acid vapor: Effect of the vapor pressure,” *J. Appl. Phys*. **85**, 1322-1328 (1999).

29. W. M. Young, M. M. Fejer, M. J. F. Digonnet, A. F. Marshall, R. S. Feigelson, “Fabrication, characterization and index profile modeling of high-damage resistance Zn-diffused waveguides in congruent and MgO:lithium niobate,” *J. Lightwave Technol.* **10**, 1238-1246 (1992).
30. E. J. Lim, S. Matsumoto, M. M. Fejer, “Noncritical phase matching for guided-wave frequency conversion,” Appl. Phys. Lett. **57**, 2294-2296 (1990).
31. M. L. Bortz, S. J. Field, M. M. Fejer, D. W. Nam, R. G. Waarts, and D. F. Welch, “Noncritical quasi-phasematched second harmonic generation in an annealed proton exchanged $LiNbO_3$ waveguides,” *Trans. on Quantum Electron.* **30**, 2953 (1994).
32. A. Galvanauskas, K. K. Wong, K. El Hadi, M. Hofer, M. E. Fermann, and D. Harter; M. H. Chou, and M. M. Fejer, “Amplification in 1.2 to 1.7 μm communication window using OPA in PPLN waveguides,” *Electron. Lett.* **35**, 731-733 (1999).
33. K. Mizuuchi, H. Ohta, K. Yamamoto, M. Kato, “Second-harmonic generation with a high-index-clad waveguide,” *Opt. Lett*. **22**, 1217-1219, (1997).
34. K. Mizuuchi, K. Yamamoto, M. Kato, “Harmonic blue light generation in X-cut $MgO:LiNbO_3$ waveguide,” *Electron. Lett.* **33**, 806-807 (1997).

CHAPTER 4

INTEGRATED WAVEGUIDE STRUCTURES FOR NONLINEAR FREQUENCY MIXING

4.1 Introduction

Waveguide confinement can significantly increase nonlinear frequency-mixing efficiency. However, a waveguide optimized for nonlinear frequency mixing in general has a tightly confined mode to reduce the effective area. The tightly confined mode is not well mode-matched to the optical fiber for fiber-pigtailing. In addition, guided-wave nonlinear frequency mixing involves two or three interacting waves at significantly different wavelengths, which complicates the input launching and thus inhibits use of the device for practical applications. In order to solve this mode-launching (i.e. coupling) issue and optimize the device, we developed integrated waveguide structures that consist of mode-coupling components and nonlinear frequency-mixing sections. In this chapter, we will describe the integrated waveguide structures and their applications in nonlinear frequency mixing. The design and characterization of integrated coupling components such as mode filters, adiabatic tapers, and directional couplers will also be described.

4.2 Integrated Waveguide Structures

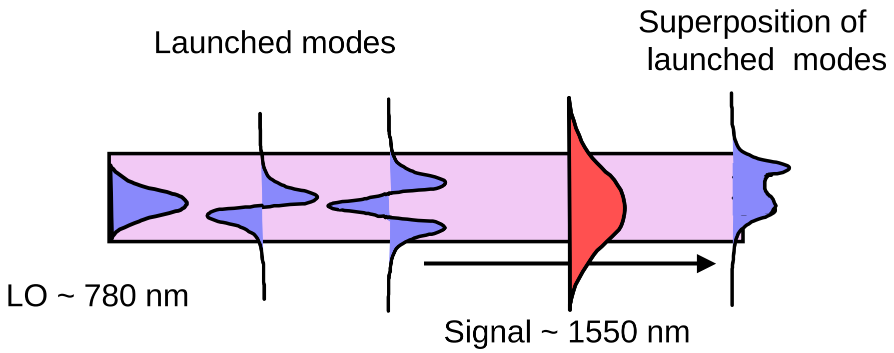

Figure 4.1 Schematic drawing of mode-launching issues. It is very difficult to launch the local oscillator into the fundamental mode of a waveguide that supports a mode at the signal (or output) wavelength, and hence several modes at the shorter (LO) wavelength.

In difference-frequency mixing (DFM), one or both of the input signal and the generated output (idler) must be at significantly longer wavelength than the local oscillator. Thus a waveguide that supports a mode at the longest wavelength (either signal or idler) is highly multimoded at the local oscillator wavelength. It is difficult to launch local oscillator radiation robustly into the fundamental mode of such a multimoded waveguide. Only the particular fraction of optical power present in the phasematched mode will contribute to the frequency conversion process. Figure 4.1 illustrates the typical result for launching the local oscillator into a multimoded waveguide. The mode-launching issues can be addressed by the integrated waveguide structures shown in figure 4.2(a) and figure 4.2(b) for off-degenerate mixing and near-degenerate mixing respectively.

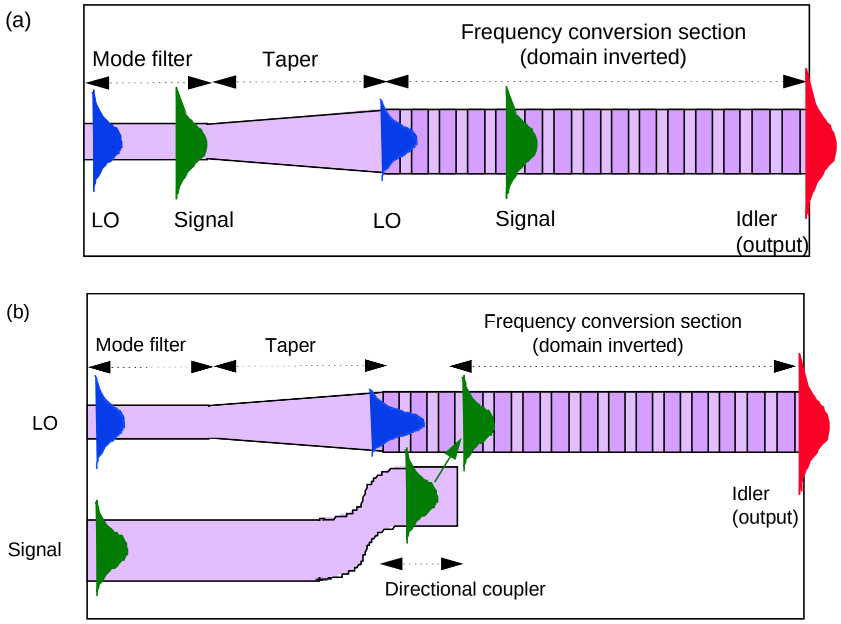

Figure 4.2 Schematic drawing of integrated nonlinear frequency mixers. (a) Off-degenerate mixing: Both local oscillator and signal are launched into a single-mode filter. A subsequent adiabatic taper permits efficient fundamental mode excitation in the DFM region. (b) Near-degenerate mixing: An adiabatic taper launches the local oscillator radiation into the fundamental mode of the DFM region, which is then mixed with the signal radiation that is launched by a directional coupler.

For off-degenerate mixing (figure 4.2(a)) the local oscillator wavelength is close to the signal wavelength (i.e. $\lambda_{LO} \sim \lambda_s$). Both local oscillator and signal are launched into a single-mode waveguide that acts as a single-mode filter and can also be optimized for efficient fiber-pigtailing. A subsequent adiabatic taper efficiently couples the input radiation into the fundamental mode of the highly multimoded waveguide, which is optimized for DFM. Both the mode filter and the taper can be implemented using periodically segmented waveguides (PSW's) [1, 2, 3, 4, 5, 6] or by nonlinear proton diffusion [7, 8] as described later.

For near-degenerate mixing (figure 4.2(b)) the local oscillator wavelength is significantly different from the signal wavelength (usually the signal wavelength is about twice the local oscillator wavelength). There is no single-mode waveguide that can serve simultaneously as the single-mode filter for both the signal and the local oscillator. So the two inputs are launched into different waveguides which are single-mode for their respective wavelengths. The local oscillator radiation is launched into the fundamental mode of the DFM region by an adiabatic taper, and the signal radiation is launched into the DFM region by a directional coupler.

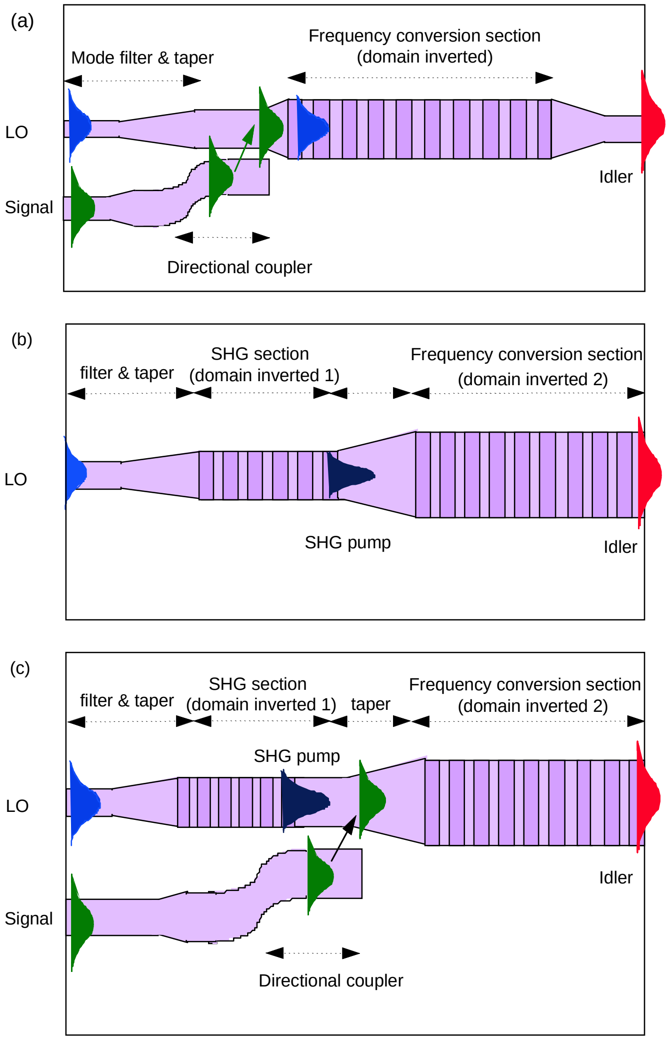

Figure 4.3 Examples of modifications of integrated coupling structures in Figure 4.2. In structures (b) and (c), the SHG section also acts as a mode converter that converts LO to the desired mode.

The integration of a waveguide mode-launching structure and a nonlinear frequency-mixing region allows for launching the input radiation into the desired mode and allows for independent optimization of each section. By use of integrated waveguide structures, we have demonstrated several periodically-poled $LiNbO_3$ (PPLN) waveguide devices for generation of tunable mid-IR radiation [9], wavelength conversion for wavelength-division multiplexed (WDM) systems [10], ultrafast pulse generation by guided-wave optical parametric generation (OPG) [11], and highly efficient second-harmonic generation (SHG) using a noncritical phasematching waveguide design (see Chapter 3).

In some applications, such as for efficiency improvement, there might be need to launch the input radiation into non-fundamental modes for guided-wave nonlinear frequency conversion. A mode converter (or coupler) can be used and integrated into the above structures [12, 13]. Since launching the input radiation into non-fundamental modes might be desired, the above integrated waveguide structures can be expanded into some other forms. For example, we can integrate (or cascade) two quasi-phasematching (QPM) gratings, the first stage is used for converting the input radiation into its second-harmonic at the desired mode and the second stage is used for further frequency conversion of the generated second-harmonic wave. Examples are shown in figure 4.3.

4.3 Adiabatically Tapered Waveguides

Introduction

Transformation of modal properties through the axial tapering of a dielectric waveguide structure is useful in several applications. In a tapered waveguide the mode size transformation allows independent optimization of the mode size in different portions of the waveguide. This increases the input and output coupling efficiency as well as the efficiency of active or electrooptic devices. An adiabatic taper from a single to a multimoded waveguide also allows robust coupling into the fundamental mode of a multimoded waveguide, which is important in several nonlinear guided-wave mixers as described above. A number of techniques have been developed for the growth of axially varying III-V semiconductor waveguides [14, 15], but less progress was made in the fabrication of tapers in diffused waveguides in insulating crystals.

While it is straightforward to taper the lateral dimension of a waveguide by lithographic means, to taper the vertical dimension requires techniques that are difficult to control such as diffusion in a temperature gradient or deposition of a nonuniform film. Since it is necessary to taper both dimensions to accomplish either a significant mode size or ellipticity transformation, a technique that facilitates the control of vertical confinement is required.

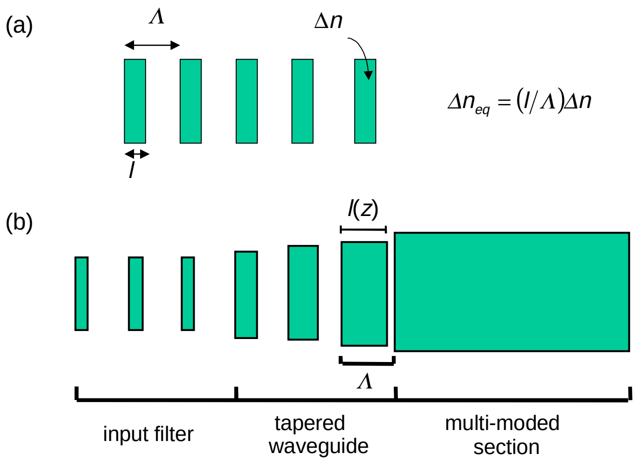

Figure 4.4 (a) Schematic plot of a periodically segmented waveguide. (b) Tapered waveguide using a segmented structure. Both the input filter section and taper are made from periodically segmented waveguides. Duty cycle and waveguide width can be modulated simultaneously to optimize the device.

A PSW consists of segments that repeat with a period Λ. Each segment consists of a region of length l that is indiffused with a dopant to produce an index-change Δn and is separated by an undoped region. Figure 4.4(a) shows a schematic plot of a PSW. Both theoretical and experimental investigations in the literature [2, 3, 4, 5, 6] show that an average-index model accurately predicts the modal properties of the waveguide. In the model the behavior of PSW is approximated by an equivalent waveguide in which the effective refractive index-step is taken to be

$$\Delta n_{eq} = \Gamma \Delta n \ , \tag{4.1}$$

where the duty cycle $\Gamma = l/\Lambda$. It has been demonstrated that under appropriate fabrication conditions the propagation losses are not significantly increased over a similar uniform waveguide. With independently controllable optical confinement in width (with physical width and segmentation duty cycle) and depth (with segmentation duty cycle), the segmented waveguide with axially-varying duty cycle is an attractive method to make a tapered waveguide, as illustrated in figure 4.4(b). Another major advantage of PSW's for tapers is that they can be integrated with essentially any existing integrated optic device without requiring additional lithography or diffusion steps.

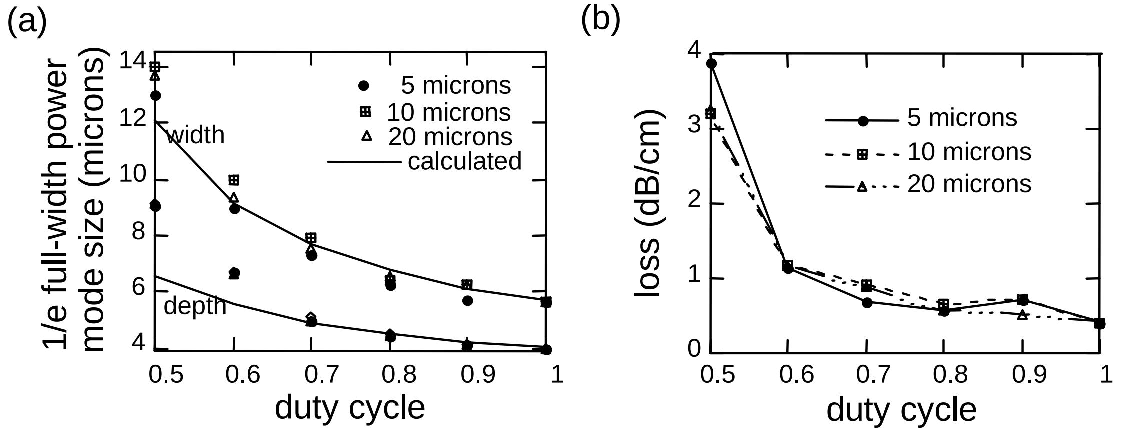

Figure 4.5 (a) Measured 1/*e* full-width power mode size vs. duty cycle, (b) measured loss vs. duty cycle for three segmentation periods (5 μm, 10 μm, and 20 μm).

We verified the reported mode and loss properties of PSW's in annealed proton-exchanged (APE) $LiNbO_3$ at 1.3-μm wavelength [5, 6]. The results are illustrated in figure 4.5 for samples annealed at 333°C for 12 hours with a proton exchange depth of 0.4 μm and a waveguide width of 5 μm at various duty cycle and segmentation periods. Figure 4.5(a) shows the measured 1/*e*-mode full-width versus duty cycle for three different segmentation periods. Results calculated based on the average-index model of equation (4.1) are also plotted in the graph. Figure 4.5(b) shows the losses *vs.* duty cycle, measured with the Fabry-Perot technique [16]. The results show that the waveguide properties depend only on the duty cycle, and do not depend significantly on the segmentation period. For sufficiently large duty cycle, the effective waveguide is not close to cutoff so the loss does not increase significantly above that of a uniform waveguide.

We chose as a demonstration a taper that allows coupling local oscillator radiation (780 nm) into the fundamental mode of a waveguide designed for near-degenerate DFM within 1.5-μm-band. A sample with proton exchange depth 0.5 μm and waveguide width 5.5 μm was chosen. After annealing at 333°C for 9 hours, it gives a waveguide single-moded at 1.5 μm and nominally 13-moded for the local oscillator. The tapered waveguide was modeled by beam-propagation methods (BPM) [17]. This device consists of a 1.5-mm-long input mode filter waveguide with a period of 10 μm and a duty cycle of 0.2. The duty cycle was increased from 0.2 to 1 gradually over the taper section according to either the linear taper function $\Gamma(z)=0.2+0.8(z/L)$ or the concave taper function $\Gamma(z)=0.2+0.8(z/L)^3$ (where z is the distance along the taper section and L is the length of the taper) without variations in waveguide width. Samples fabricated according to these designs were tested at 780 nm for spatial mode profiles, taper losses, mode conversion efficiency (defined as the ratio of the output power in the fundamental mode to the total output power), and dependence of output mode on input coupling conditions. The measured spatial mode profiles, with 1/*e*-intensity-dimensions of the fundamental mode equal to 6.0 µm x 4.4 µm in the input filter sections and 2.0 µm x 1.3 µm in the multi-mode sections (with a 2.5-mm-long concave taper), are shown in figure 4.6.

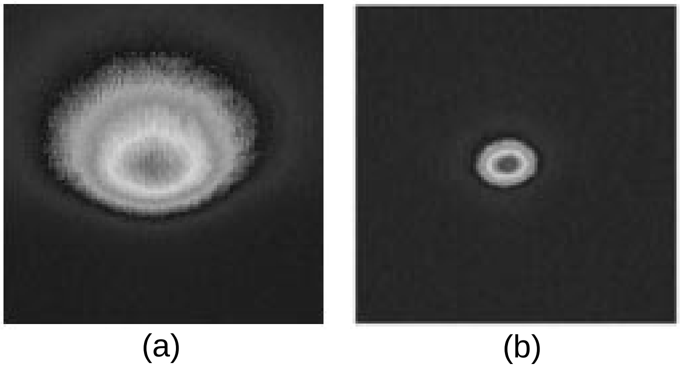

Figure 4.6 Measured mode profiles at wavelength 780 nm using a PSW taper (a) in the input filter section; (b) in the multi-mode section. Image fields are 11.7 µm x 11.7 µm.

To measure the excess loss of the fundamental transverse mode in the taper, we fabricated 11-mm-long (straight) segmented waveguides with and without back-to-back tapers. Both waveguides are single-mode at their input and output ends, and so could be tested by the Fabry-Perot method [16]. The total propagation loss of the (straight) segmented waveguide was 1.1 dB and the total propagation loss of the segmented waveguide with two 1-mm-long concave tapers was 2.3 dB. Subtracting the losses of the straight section (assumed the same losses as in the waveguide without tapers) leaves the excess loss of 0.6 dB for each 1-mm-long concave taper. Similarly, we obtained the excess losses 1.5 dB for a 1-mm-long linear taper and 0.4 dB for a 2.5-mm-long concave taper.

We used modal interference to measure the mode launching efficiency. When more than one mode is excited in the waveguide, the output intensity distribution is determined by the coherent sum of the modal fields present at the output of the waveguide. Even a small power fraction in a high-order mode will cause a large change in the output intensity distribution because of the coherent summation of the fields (rather than the intensities). To quantify the fraction of power in the fundamental mode, we observed the output intensity distribution while fine tuning the wavelength of a 780-nm diode laser used to excite the waveguide. Wavelength dependence of the output intensity distribution results from the difference in propagation constants between the fundamental mode and the high-order mode. The fields then add in or out of phase with each other as the wavelength varies. Assuming (as predicted by simulations) that the second high-order width mode (i.e. the first even-high-order width mode) and the first high-order depth-mode dominate the undesired modal excitation, then the observed output intensities can be fitted with respect to the power ratio of the fundamental mode to the high-order mode. Figure 4.7 shows the measured intensity profiles of the maximum and minimum widths for a 1-mm-long concave taper. The solid lines are fits for 0 and π relative phases of the fundamental and high-order mode, corresponding to mode conversion efficiencies of 97% in width and 98% in depth, resulting in 95% overall.

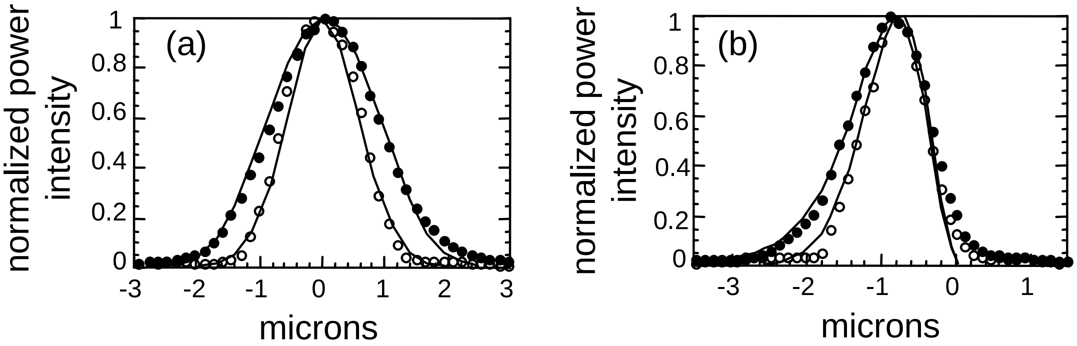

Figure 4.7 Output intensity profiles resulting from modal interference for two different wavelengths. Circles are measured results; solid lines are curve fits for 0 and π relative phases between the fundamental TM_{00} mode and the first allowed high-order transverse mode, (a) in the width direction; (b) in the depth direction.

We tested the sensitivity of the output intensity distribution to the input coupling conditions to illustrate that the filtering action in the input filter region prevents launching of undesired modes. Figure 4.8 illustrates the output intensity distributions observed with different input coupling conditions for a waveguide without any taper and a waveguide with a 1-mm-long concave taper. As the waveguides were moved laterally (as shown) and vertically for about 1.7 μm, the output mode mixture for the waveguide without taper is highly sensitive to input coupling conditions, while the output mode mixture for the waveguide with the coupling taper is essentially independent of the input coupling conditions.

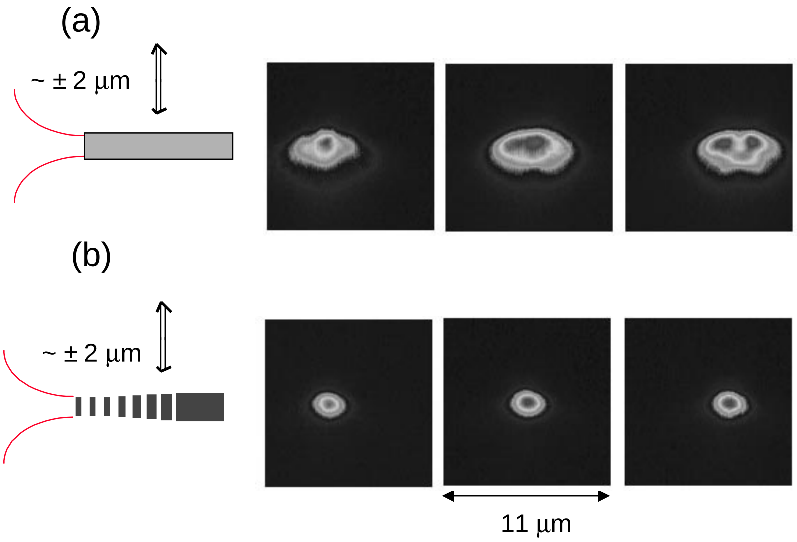

Figure 4.8 Measured output intensity profiles for different input coupling conditions for launching the light into a waveguide (a) without any taper; (b) with an adiabatic taper. In this example, the waveguides are moved in the width direction for about 1.7 microns relative to the incident beam to change coupling conditions.

Adiabatic Taper Using Nonlinear Diffusion

Segmented tapered waveguides are one of the most flexible tapering methods, allowing tapering of the waveguide geometry and of the equivalent refractive index of a waveguide. However, segmented tapered waveguides introduce some excess losses due to a highly non-continuous structure. In this section, we describe an adiabatic taper in APE-$LiNbO_3$ waveguides by use of the concentration-dependent diffusion.

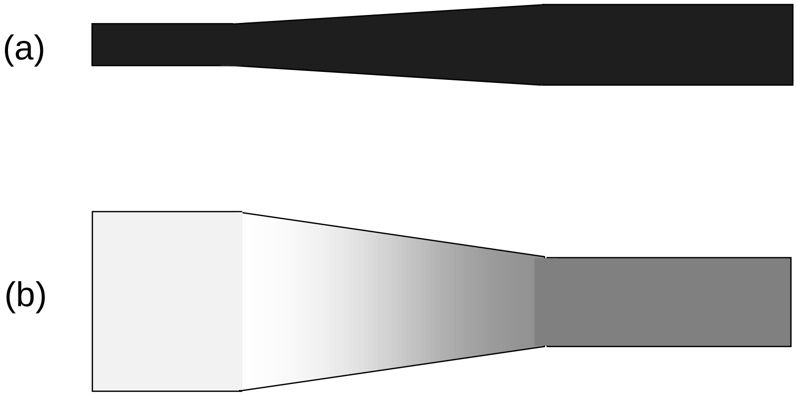

Figure 4.9 (a) PE-$LiNbO_3$ waveguide with a width taper. Refractive index and waveguide depth is constant throughout the taper. (b) APE-$LiNbO_3$ tapered waveguide (after annealing the taper (a)).

The annealing process of proton-exchanged (PE) $LiNbO_3$ waveguides can be modeled by concentration-dependent diffusion, where the diffusion coefficient is a function of the proton concentration. According to the reported model [7, 8] the diffusion coefficient increases dramatically in a region of low proton concentration; the ratio of the diffusion coefficient at a low proton concentration to that at a high proton concentration can be as large as 5. This property can be used for APE-$LiNbO_3$ waveguides to simultaneously taper the waveguide width, depth, and refractive index, as shown in figure 4.9. A PE-$LiNbO_3$ waveguide with the waveguide width defined by a photomask is shown in figure 4.9(a). The refractive index and the waveguide depth are the same throughout the taper structure. Figure 4.9(b) shows the structure after the annealing process. According to the concentration-dependent diffusion model, the input waveguide will become wider and deeper, and has a weak refractive index (low proton concentration). This results in a large mode at the input, which can be designed to be single mode as a mode filter and optimized for fiber-waveguide coupling. The frequency conversion section waveguide will keep the higher refractive index and the tightly confined mode, which are suitable for efficient electro-optic interaction or nonlinear frequency conversion. The adiabatic taper transforms the large input mode into a tightly confined mode.

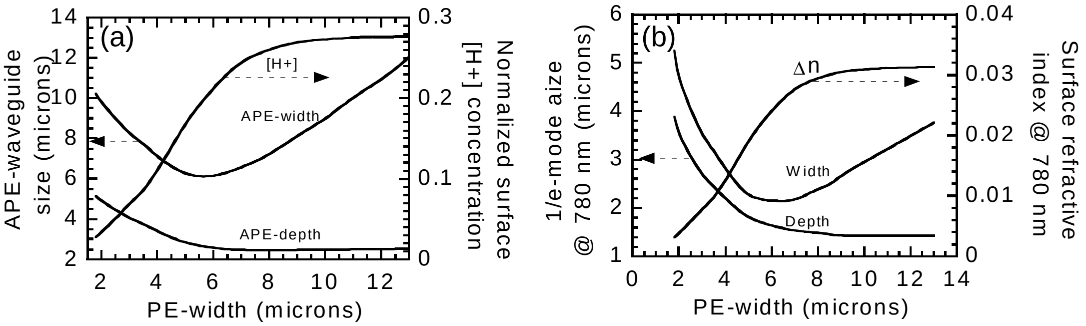

Figure 4.10 (a) calculated 1/*e*-APE-waveguide size and normalized on-axis surface H^+-concentration vs. PE-waveguide width. (b) calculated 1/*e*-mode size and surface refractive index at 780 nm vs. PE-waveguide width. Initial PE-depth, annealing time and temperature are assumed to be 0.71 μm, 25 hours, and 325 °C, respectively.

We designed and fabricated an APE-$LiNbO_3$ tapered waveguide based on the concentration-dependent diffusion model. The taper structure is designed for launching a 780-nm wavelength into the fundamental mode of a multimoded waveguide, optimized for a nonlinear frequency mixing of a wave at 1560 nm and its harmonic wave at 780 nm. The taper function is formed by the quadratic relation $W(z) = 1.8 + 9(z/L)^2$, where $W(z)$ is the waveguide mask width. The sample was proton exchanged at 160 °C for 15 hours, resulting in the PE-waveguide depth of

0.71 μm, and was annealed at 325 °C for 25 hours. Figure 4.10(a) shows a calculated 1/*e*-APE-waveguide size and normalized surface H^+-concentration vs. PE-waveguide width using the above fabrication conditions. The surface H^+-concentration was normalized to that of the PE-waveguide. Figure 4.10(b) shows a calculated 1/*e*-mode size and surface refractive index at 780 nm vs. PE-waveguide width.

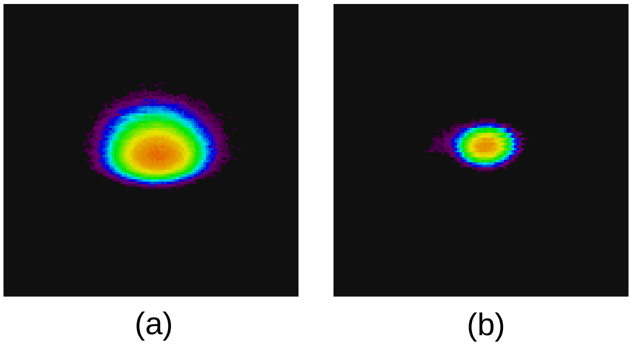
(a) (b)

Figure 4.11 Measured mode profiles at wavelength 780 nm for a nonlinearly diffused taper (a) in the input filter section; (b) in the multi-mode section. Image fields are ~14 μm x 14 μm.

We tested the taper by measuring the mode size and mode excitation efficiency, as shown in figure 4.11. The measured 1/*e*-intensity-dimensions of the fundamental mode were 3.7 μm x 2.7 μm **(**width x depth) at the single mode input section and 2.4 μm x 1.5 μm at the multimoded section. The results cannot be fitted directly by our design and fabrication conditions. We suspected that the discrepancy was due to waveguide patterning and lateral proton exchange, which make the actual PE-waveguide width wider than the mask width. With the above assumption, experimental results are close to a waveguide with effective PE-waveguide widths of 2.8 μm at the input section and 11.8 μm at the multimoded section rather than the design values of 1.8 μm and 10.8 μm, respectively, reasonably consistent with lateral spreading equal to the exchange depth. According to the nonlinear diffusion model with these assumed PE dimensions, the 1/*e*-APE-waveguide size and surface refractive index of the taper structure are 8.4 μm x 8.6 μm and 0.0063 (for 780 nm) at the input section, and 2.5 μm x 10.9 μm and 0.0312 at the multi-mode section.

4.4 Directional Coupler

Directional couplers are important components and have wide applications in integrated optics and fiber optics. They can be used as power splitters or wavelength selective couplers, such as WDM couplers for combining pump and signal in erbium-doped-fiber amplifiers (EDFA's).

They can also be used for optical switching by applying electrical or optical control signals. The design of directional couplers has been well studied [18, 19]. In this section, we will describe only a noncritical design that allows the directional coupler to be less sensitive to waveguide width variations.

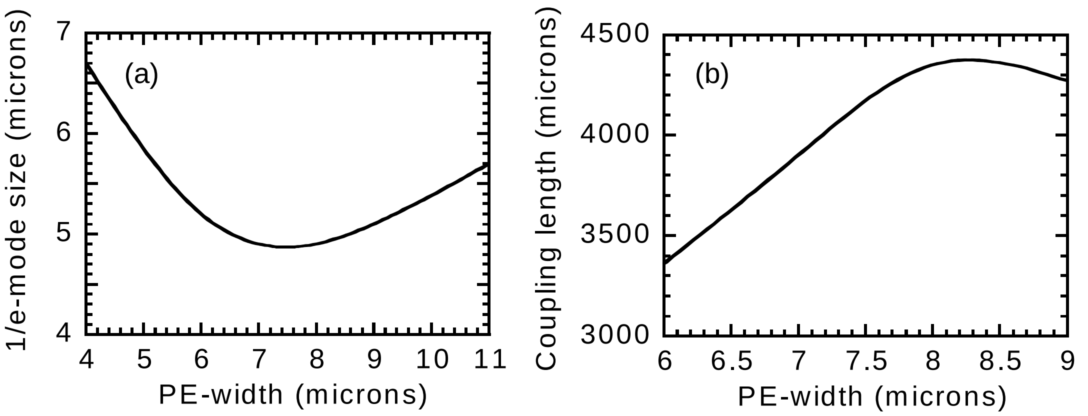

Figure 4.12 (a) Calculated 1/*e*-mode size of 1550 nm waveguide in the width direction vs. PE-waveguide width; (b) calculated length of the directional coupler for 100% coupling vs. PE-waveguide width.

The coupling length of a directional coupler is a function of the mode overlap between two adjacent waveguides; the mode overlap is sensitive to waveguide width variations even with the same waveguide center-to-center separation. In practice, the waveguide width is sensitive to the fabrication processes, such as photolithography, etching, proton-exchange, etc. Thus to increase the tolerance, one can design a waveguide where the waveguide mode size is less sensitive to width variation. Figure 4.12(a) shows the calculated 1/e-mode size at 1550 nm in the width-direction versus PE-waveguide width. Proton exchange at 160 °C for 15 hours and annealing at 325 °C for 25 hours were used in the calculation. In the narrow waveguide region, the mode width decreases as the waveguide width increases due to the improved confinement. In the wide waveguide region, the mode width increases as the waveguide width increases because the waveguide geometry dominates the mode size. In the transition region, the first derivative of mode size with respect to waveguide width is zero. Figure 4.12(b) plots the calculated coupling length vs. waveguide width. The first derivative of mode size with respect to waveguide width is zero at a waveguide width ~8 μm. The major drawback of this design is that it requires a longer coupling length due to tightly confined waveguide modes. However, we use it in devices described in section 5.2 because of its greater fabrication tolerances.

4.5 Summary

In this chapter, we have addressed the mode launching issues of guided-wave nonlinear frequency mixing using integrated waveguide structures. The integration of waveguide mode coupling structure (adiabatic taper and directional coupler) with the nonlinear frequency-mixing region allows for launching the input radiation into the desired mode and allows for efficiency optimization. Two attractive approaches, segmented structures and nonlinear diffusion, for fabricating adiabatic tapers have been described. A method for designing a noncritical directional coupler (less sensitive to the waveguide width variation) has also been described. The concepts of integrated structures and techniques for realizing the mode coupling components will be very important for future sophisticated guided-wave nonlinear frequency mixers, and are used in the devices described in Chapter 5 through Chapter 7.

Reference for Chapter 4:

---

1. M. H. Chou, M A. Arbore, and M. M. Fejer, “Adiabatically tapered periodic segmentation of channel waveguides for mode-size transformation and fundamental mode excitation,” *Opt. Lett.* **21**, 794-796 (1996).
2. Z. Weissman and A. Hardy, “2-D mode tapering via tapered channel waveguide segmentation,” *Electron. Lett.* **28**, 1514-1516 (1992).
3. Z. Weissman and A. Hardy, “Modes of periodically segmented waveguides,” *J. Lightwave Technol.* **11**, 1831-1838 (1993).
4. L. Li and J. J. Burke, “Linear propagation characteristics of periodically segmented waveguides,” *Opt. Lett.* **17**,1195 –1197 (1992).
5. K. Thyagarajan, C. W. Chein, R. V. Ramaswany, H. S. Kim, and H. C. Cheng, “Proton-exchanged periodically segmented waveguides in $LiNbO_3$,” *Opt. Lett.* **19**, 880-882 (1994).
6. D. Nir, S. Ruschin, A. Hardy and D. Brooks, “Proton-exchanged periodically segmented channel waveguides in lithium niobate,” *Electron. Lett.* **31**, 186-188 (1995).
7. M. L. Bortz and M. M. Fejer, “Annealed proton-exchanged $LiNbO_3$ waveguides,” *Opt. Lett.* **16**, 1844-1846 (1991).
8. M. L. Bortz, “Quasi-phasematched optical frequency conversion in lithium niobate waveguides,” Ph.D. Dissertation, Department of Applied Physics, Stanford University, Stanford, CA (1994).
9. M. A. Arbore, M. H. Chou, and M. M. Fejer, “Difference frequency mixing in $LiNbO_3$ waveguides using an adiabatically tapered periodically-segmented coupling region,” *CLEO’96*, JTuE2.
10. M. H. Chou, J. Hauden, M. A. Arbore, and M. M. Fejer, “1.5-μm-band wavelength conversion based on difference frequency generation in $LiNbO_3$ waveguides with integrated coupling structures,” *Opt. Lett.* **23**, 1004-1006 (1998).
11. M. A. Arbore, M. H. Chou, M. M. Fejer, A. Galvanauskas, and D. Harter, “380-pJ-threshold optical parametric generator in periodically poled lithium niobate waveguides,” *ASSL’98*, PD paper.
12. H. Nishhara. M. Harauna, T. Suhara, *Optical Integrated Circuits*, McGraw-Hill, New York 1987, pp.62-95.
13. T. U. Haq, K. Webb, N. C. Gallagher, “Synthesis of waveguide mode control devices based on aperiodic gratings,” *J. Opt. Soc. Am. A* **13**, 1501-1505 (1996).
14. A. Shahar, W. J. Tomlinson, A. Yi-Yan, M. Seto and R. J. Deri, “Dynamic etch mask technique for fabricating tapered semiconductor optical waveguides and other structures,” *Appl. Phys. Lett*. **56**, 1098-1100 (1990).

---

15. H. S. Kim, S. Sinha and R. V. Ramaswamy, "An MQW-SQW tapered waveguide transition," *IEEE Photon. Techonl. Lett.* **5**, 1049-1052 (1993).
16. R. Regener and W. Sohler, "Loss in low-finesse Ti:LiNbO$_3$ optical waveguide resonators," *Appl. Phys. B* **36**, 143-147 (1985).
17. M. D. Feit and J. A. Fleck, Jr., "Mode properties of optical fibers with lossy components by the propagating beam method," *Appl. Opt.* **20** , 848-856 (1981).
18. R. Syms and J. Cozens, *Optical Guided Waves and Devices*, McGraw-Hill, England, 1992. pp. 250-267.
19. K. Kissa, "Modeling annealed proton-exchanged directional couplers with nonlinear diffusion theory," *IEEE Photon. Techonl. Lett.* **9**, 1065-1067 (1993).

CHAPTER 5

OPTICAL FREQUENCY MIXERS AS WAVELENGTH CONVERTERS IN WDM NETWORKS

5.1 Introduction

Wavelength-division multiplexing (WDM) effectively utilizes fiber bandwidth in the wavelength domain, where multiple independent channels are transmitted at different carrier wavelengths to increase system capacity. In addition, WDM offers flexible interconnections based on wavelength routing. However, realization of all-optical transparent WDM networks requires functions (such as switching, wavelength add/drop, wavelength conversion, etc.) beyond those required for WDM point-to-point connections.

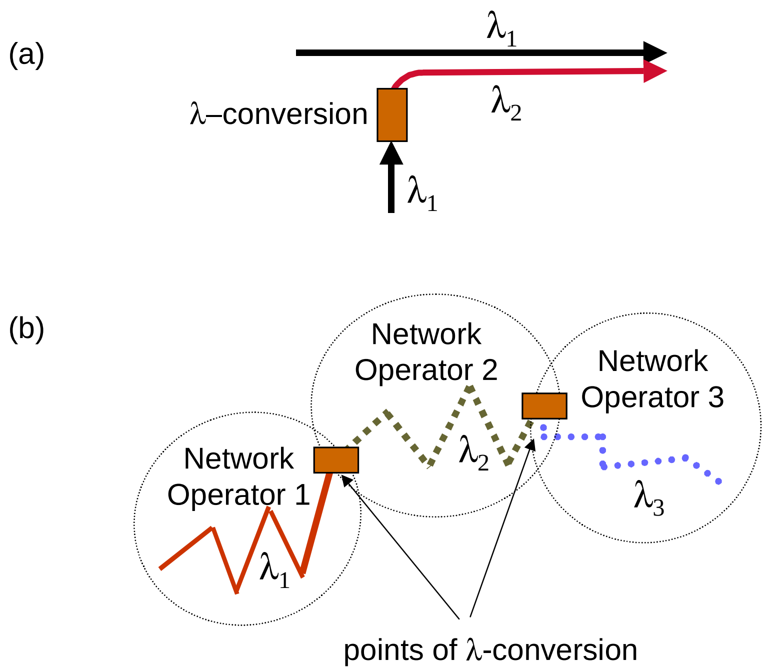

Figure 5.1 (a) Network blocking probabilities can be resolved by wavelength-conversion function. (b) Distribution of network control and management into smaller sub-networks utilizes wavelength conversion. Network operators 1, 2, and 3, are responsible for their own sub-networks, and wavelength assignments within the sub-networks are independent of each other. [References 1, 2, 3, 4]

To enable full flexibility and easy management of a transparent WDM network, one of the most important functions is wavelength conversion. In WDM networks, single fiber capacity can be expanded to fulfill the required information capacities by increasing the number of different wavelengths. However, the number of interconnection nodes is often not large enough to support a large number of different wavelengths. In such a case, blocking probability rises due to the possible wavelength contention when two channels at the same wavelength are to be routed into the same output. One solution to this problem is to convert signal from one wavelength to another, as illustrated in figure 5.1(a). Wavelength conversion also allows distributing the network control and management into smaller sub-networks, thus wavelength can be flexibly assigned within each sub-network, as shown in figure 5.1(b). Other functions that have been foreseen include wavelength routing, data format conversion, etc. [1, 2, 3, 4, 5, 6, 7].

Several wavelength conversion techniques have been demonstrated, which can be classified as optoelectronic converters (O/E-E/O), incoherent all-optical converters (cross-gain modulation (XGM) or cross-phase modulation (XPM**),** and coherent all-optical converters (four-wave mixing (FWM) or difference-frequency mixing (DFM)). Comparison of those conversion schemes can be found in references [4, 8, 9]. To evaluate the adequacy of wavelength converters for transparent WDM networks, numerous requirements need to be addressed. An example illustrating the considerations in such an evaluation is shown in figure 5.2 [10].

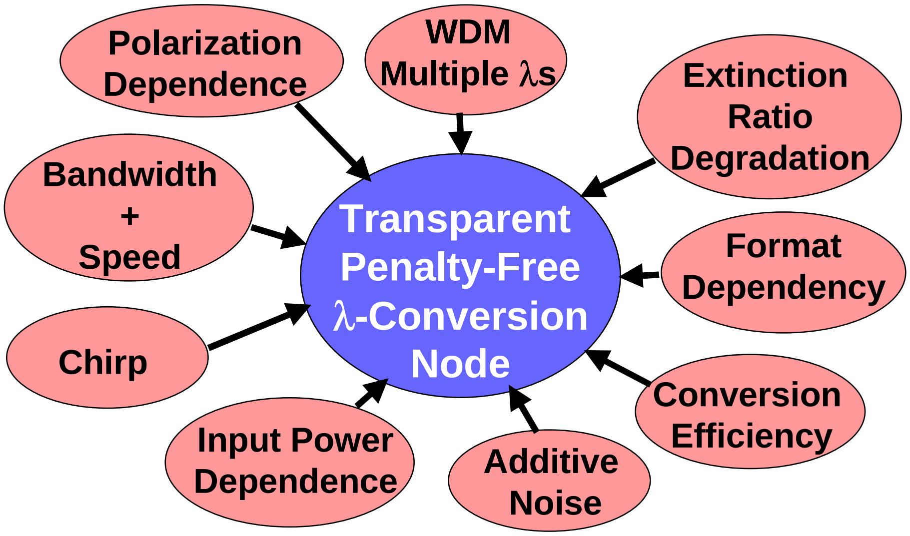

Figure 5.2 Issues of the transparent and penalty-free wavelength-conversion node need to be considered. [Reference 10, A. E. Willner]

Nonlinear frequency mixing based on the second-order nonlinear susceptibility $\chi^{(2)}$ is very attractive for wavelength conversion and offers a number of unique properties that are unavailable in other techniques. The $\chi^{(2)}$-based wave-mixing process, similar to FWM, belongs to coherent wave mixing, thus this process has most of the parametric properties of FWM. Unlike

FWM, the $\chi^{(2)}$-based wave mixing processes do not create additional cross-terms that will interfere with other WDM channels. $\chi^{(2)}$-based wavelength conversion offers strict transparency to amplitude, frequency, and phase information, which allows simultaneous conversion of several signal formats (digital, analog, etc.). The conversion process adds negligible amplified-spontaneous emission (ASE) noise, has extremely high input dynamic range, and can easily accommodate terahertz modulation bandwidth. It can also up- and down- convert multiple wavelengths simultaneously. In addition, the conversion process generates chirp-reversed signal output, which can be used to perform dispersion compensation of fiber links.

Wavelength converters based on $\chi^{(2)}$ can be implemented by a variety of different schemes: DFM [11, 12, 13, 14, 15, 16, 17] and cascaded second-order nonlinear frequency mixing ($\chi^{(2)}$:$\chi^{(2)}$ mixing) [18, 19, 20, 21, 22] with co-propagating beams or counter-propagating beams. In this chapter, we show experimental demonstrations of OF mixers as wavelength converters and evaluate their performance for transparent WDM networks. We will also compare these different conversion schemes.

5.2 1.5-μm-Band Wavelength Conversion Based on DFM

Introduction

1.5-μm-band wavelength conversion based on DFM in AlGaAs and annealed proton-exchanged (APE) $LiNbO_3$ waveguides has been demonstrated prior to this thesis. However, the previous results [11, 12, 13, 14, 15, 16] suffered from low conversion efficiency (<-17 dB) because of high propagation losses (in AlGaAs) or limited homogeneous interaction length (in $LiNbO_3$). Another critical issue with guided-wave DFM, as described in Chapter 4, is to launch the local oscillator (short wavelength) into the fundamental mode of a waveguide that can confine the signal (long wavelength) and hence is multi-mode at the local oscillator wavelength. In this section, we will show the performance of OF mixers as 1.5-μm-band wavelength converters based on the fabrication techniques and integrated waveguide structures described in Chapter 3 and Chapter 4.

The DFM-based wavelength converter generates an output at wavelength λ_{out} by mixing the signal at wavelength λ_s with a local oscillator at wavelength λ_{LO} according to the parametric equation:

$$\frac{1}{\lambda_{out}} = \frac{1}{\lambda_{LO}} - \frac{1}{\lambda_s}. \tag{5.1}$$

Such a parametric process allows conversion of multiple input wavelengths (or channels). Each set of input and output wavelengths follows the same parametric equation (5.1), where the efficiency for each channel is similar as long as the phasematching condition is fulfilled for each individual channel (i.e. channels are within the signal bandwidth). An architecture for a wavelength interchanging cross-connect (WIXC) using such a parametric wavelength conversion process has been proposed by Antoniades *et al.* and demonstrated to be scaleable and rearrangeably non-blocking [5]. Four inputs at wavelengths λ_1, λ_2, λ_3, and λ_4 (with equal frequency difference between every nearest two) are converted to their respective wavelengths λ_4, λ_3, λ_2, and λ_1 by use of a local oscillator at wavelength λ_{LO} that satisfies $1/\lambda_{LO}=1/\lambda_3+1/\lambda_2$ relation. Thus the information carried by the input wavelength is interchanged with the output wavelength by a mirror image mapping relative to frequency $\omega_{LO}/2$. This mirror image property of multi-channel conversion is the key characteristic of the proposed parametric WIXC architecture [5].

Device Fabrication

To demonstrate OF mixers as 1.5-μm-band wavelength converters, we fabricated the waveguides by annealed proton-exchange in periodically poled $LiNbO_3$ (PPLN). The device includes an integrated waveguide structure for efficient mode coupling and has a 41-mm-long wavelength-conversion section with a quasi-phasematching (QPM) grating period of 14.75 μm. Figure 4.3(c) shows the waveguide structure of the device; the detailed device parameters are described in reference 23. The normalized efficiency of this device is 50-60%/W-cm^2 with waveguide propagation losses ~0.7 dB/cm at 780 nm and 0.35 dB/cm at 1550 nm. The device has a near ideal sinc^2 second-harmonic generation (SHG) tuning curve with internal SHG efficiency (output second-harmonic power divided by the square of input fundamental power) of 500-600%/W and 3-dB SHG bandwidth of ~0.27 nm.

Conversion Efficiency

Operation of a 1.5-μm-band wavelength converter based on DFM requires a CW local oscillator at wavelength ~780 nm and power of 50-100 mW with current device performance (lower power operation is possible in the future). The conversion efficiency for an ideal (lossless) waveguide is related to the normalized efficiency, device length, and local oscillator power by equation (2.20):

$$\eta\ (\mathrm{dB}) \equiv 10\log\left(P_{out}/P_s\right) \tag{5.2a}$$

$$= 10\log\left[\sinh^2\left(\sqrt{\eta_{norm}L^2P_{LO}}\right)\right] \tag{5.2b}$$

$$\approx 10\log\left(\eta_{norm}L^2P_{LO}\right) \qquad (\text{for } \eta_{norm}L^2P_{LO} < 1) \tag{5.2c}$$

The normalized efficiency η_{norm} for near-degenerate DFM is similar to that of SHG. The power conversion efficiency ($=P_{out}/P_s$) is linearly proportional to the local oscillator power in the limit of low conversion efficiency (from equation (5.2c)). At higher conversion efficiencies (when there is significant signal parametric gain), equation (5.2b) should be used.

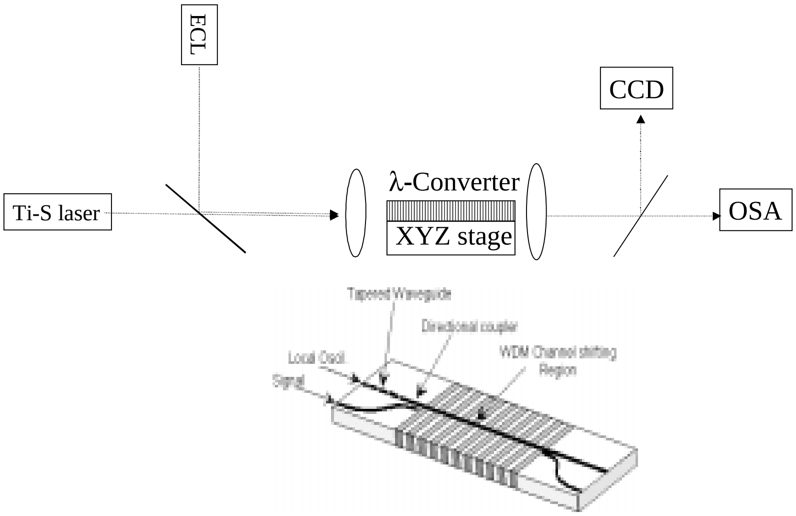

Figure 5.3 Experimental configuration of DFM wavelength conversion. Local oscillator and signal are launched into different ports and then combined by the directional coupler.

Figure 5.3 shows a schematic diagram of the experimental setup for the wavelength conversion. A CW Ti-sapphire laser at ~781 nm was used as local oscillator, and the 1.5-μm-band signal is from an external cavity laser (ECL) and amplified through an erbium-doped-fiber amplifier (EDFA). These two beams were free-space launched into two different waveguides and combined into the wavelength converter by an integrated directional coupler. The local oscillator light that exits the waveguide was imaged onto a CCD camera, with which it was seen that TM_{00} mode of the waveguide was excited. During the measurement, the sample was maintained at 120 °C to reduce the photorefractive effects. With 90 mW of coupled local oscillator powers, we observed a stable internal conversion efficiency of -4 dB. Figure 5.4 shows a measured optical spectrum on a log scale for a signal at 1540 nm and its converted output, which has been shifted by 44 nm to 1584 nm. Note that there is about 2-dB parametric gain for the signal in this conversion process.

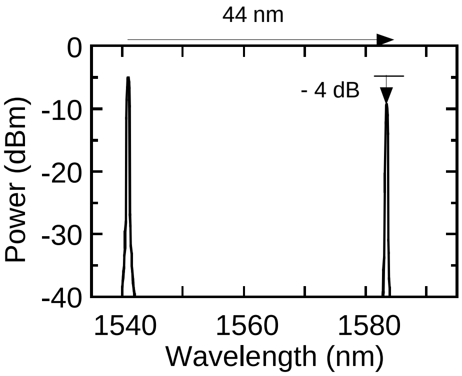

Figure 5.4 Measured optical spectrum on a logarithmic scale of a signal at 1540 nm and its converted output, which has been shifted 44 nm to 1584 nm and has internal conversion efficiency of –4 dB.

Bandwidth

The 1.5-μm-band wavelength converter has a wide conversion bandwidth due to the near-degenerate operation where the output wavelength moves in the opposite direction with respect to the signal wavelength tuning. The conversion efficiency is proportional to the square of the interaction length, but the signal bandwidth is inversely proportional to the square root of the interaction length. Thus doubling the device length will improve the conversion efficiency by 5-6 dB and reduce bandwidth by 30%. We measured the conversion bandwidth of this converter by tuning the input signal wavelength with the local oscillator wavelength fixed at 781 nm, as shown in figure 5.5. This device shows a 3-dB signal bandwidth of 56 nm, which is wider than the bandwidth (~40 nm) of conventional EDFA's. The device bandwidth can be broadened to more than 100 nm by detuning local oscillator and/or using non-uniform QPM structures, which will be described in Chapter 7.

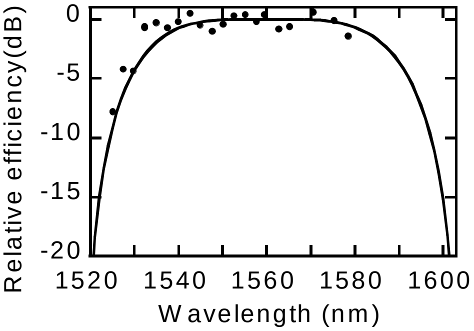

Figure 5.5 Relative conversion efficiency as a function of input signal wavelength. The closed circles are measured results, and the solid line is the theoretical prediction. This 41-mm-long device has a 3-dB conversion bandwidth of 56 nm.

Linearity

DFM-based devices have the same conversion efficiency over a wide signal power range (high dynamic range). The deviation from linearity (or deviation from constant conversion efficiency) comes from the depletion of local oscillator power. For $\eta_{norm}L^2P_{LO}<1$ and $P_s<P_{LO}$, conversion efficiency reduction $\Delta\eta$ (dB) can be approximated by

$$\Delta\eta \approx 10\log\left(1+\eta_{norm}L^2P_s\right). \tag{5.3}$$

For an ideal device with a nonlinear mixing efficiency of 1000%/W, the conversion efficiency will be reduced by 0.04 dB for a 0-dBm input signal, or 0.42 dB for 10 dBm. We performed wavelength conversion by varying the input signal power over a 50-dB range (from -50 dBm to 0 dBm), and no deviation from linearity was observed at the 0.1-dB limit of the measurement.

Spectral Inversion

For DFM-based wavelength converters, the converted electric field is the complex conjugate of signal electric field (i.e. $E_{out}\sim E_s^*$), meaning that the output electric field spectrum is the mirror image of the input signal electric field spectrum relative to the local oscillator frequency. We performed such a measurement by inputting a signal with a distorted spectrum; the result is shown in figure 5.6. This feature can be used to invert the signal chirp for dispersion compensation in a transmission system, which will be investigated in Chapter 6.

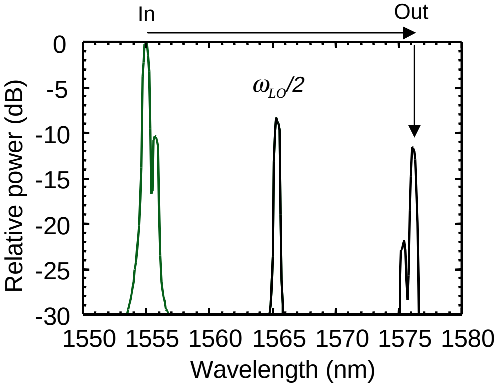

Figure 5.6 Spectral inversion of the DFM wavelength converter. The output electric field spectrum is the mirror image of the input spectrum relative to the degenerate frequency ($\omega_{LO}/2$).

Multi-Channel Conversion

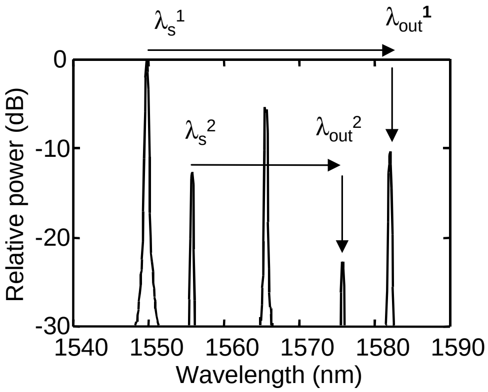

Figure 5.7 Measured optical spectrum on a logarithmic scale for two input signals at 1549.6 nm and 1555.6 nm and their converted output 1582 nm and 1575.7 nm, respectively. The central peak at 1565.6 nm is the second-order spectrometer response to the local oscillator wavelength of 782.8 nm.

The parametric frequency-conversion process allows for simultaneous up and down conversion of multiple channels with similar efficiencies, as long as the channels are within the signal bandwidth. We performed wavelength conversion simultaneously for two input channels using two 1.5-μm lasers. Similar conversion efficiency was observed for both channels, as shown in figure 5.7. The issues related to the crosstalk of multi-channel conversion will be discussed in Chapter 6.

Summary

In this section, we have shown the performance of a DFM-based 1.5-μm-band wavelength converter, which consists of a 41-mm-long interaction length and integrated waveguide structures. The device has an internal conversion efficiency of –4 dB with 90 mW of coupled local oscillator power, conversion bandwidth of 56 nm, and constant conversion efficiency over the measured signal power range of 50 dB. It generates spectrally inverted outputs and can perform multiple channel conversion. Such a conversion process adds negligible spontaneous noise and so does not significantly degrade the signal-to-noise ratio. By improving the device fabrication process (such as improved waveguide uniformity and lower propagation loss), 0-dB conversion efficiency should be possible with a diode laser local oscillator.

5.3 1.3-μm-Band and 1.5-μm-Band Bi-directional Wavelength Conversion Based on DFM

Introduction

Although transmission in the 1.5-μm-band is attractive because of the availability of the EDFA, a large proportion of existing systems still operate at the 1.3-μm-band. In addition, some recently proposed local access schemes [24, 25] deliberately use both 1.3-μm-band and 1.5-μm-band in the same network because demultiplexing these channels is straightforward. To exploit the full bandwidth of silica optical fiber, it will be necessary to use both the 1.3-μm and the 1.5-μm low loss transmission windows in the future multi-wavelength optical networks. To realize an efficient optical network, all-optical wavelength conversion between these two bands is useful. Wavelength conversion between the 1.3-μm-band and the 1.5-μm-band using DFM has been demonstrated in $LiNbO_3$ waveguides [26] but suffered from low conversion efficiency (-31 dB) owing to several technological issues, including unoptimized design and inhomogeneous waveguide fabrication. In this section, we address those issues and show an efficient 1.3/1.5-μm-band bi-directional wavelength converter [27].

Device Fabrication

Wavelength conversion based on DFM between the 1.3-μm-band and the 1.5-μm-band uses a local oscillator at ~710 nm. The 1.3/1.5-μm-band bi-directional wavelength converter has properties similar to those of a 1.5-μm-band converter, such as adding negligible spontaneous noise and having signal-format independence. To optimize the device and solve the multi-wavelength coupling issue, integrated waveguide structures are again required. Thus we fabricated the wavelength converter using similar structures and processing steps as for the 1.5-μm-band devices. The device has a 33-mm interaction length and has a QPM period of 11.5 μm. Details of device parameters are given in reference 28.

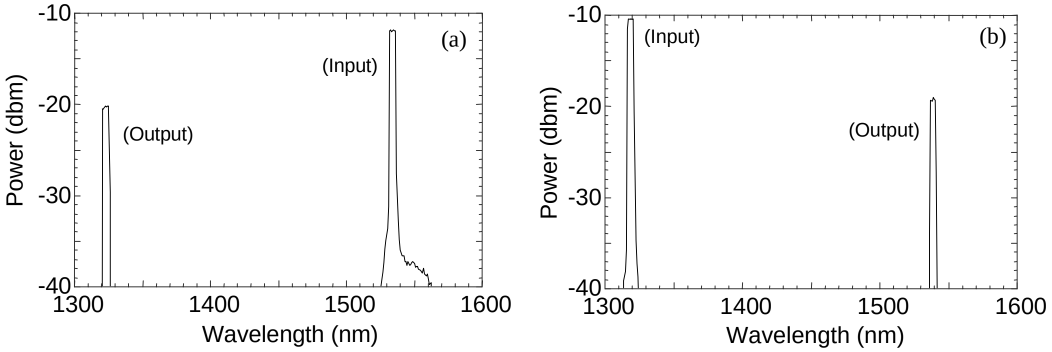

Figure 5.8 (a) Measured optical spectrum for a signal at 1533 nm and its converted output at 1324 nm. The conversion efficiency is -9 dB, corresponding to a nonlinear mixing efficiency of 380%/W. (After correction for waveguide propagation losses and Fresnel losses) (b) Optical spectrum for a signal at 1319 nm and its converted output at 1538 nm.

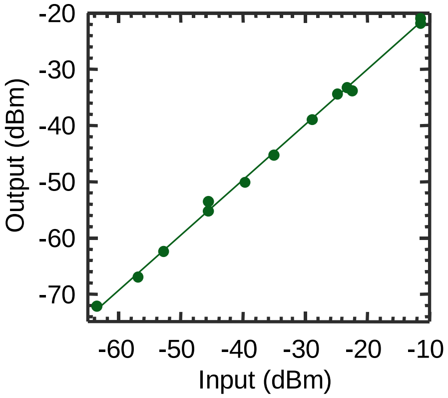

Figure 5.9 Measured output power vs. input signal power for converting a signal from 1319 nm to 1538 nm. The result shows good linearity over the 50-dB power range tested, indicating a high signal dynamic range.

Static wavelength conversion tests were performed using a CW Ti-sapphire laser at 710 nm for the local oscillator, a CW tunable erbium-doped-fiber laser for the 1.5-μm signal, and a Nd:YAG laser at 1.319 μm. Figure 5.8(a) shows a measured optical spectrum for a signal at 1533 nm and its converted output at wavelength 1323 nm. Figure 5.8(b) shows the conversion from 1319 nm to 1538 nm. With ~40 mW of coupled local oscillator power, we observed a conversion efficiency of ~-9 dB. Note that there will be equal quantum efficiencies for up and down conversion, which correspond to a power conversion efficiency imbalance of 0.7 dB due to the energy difference between 1.3-μm and 1.5-μm photons. The device was linear over the 50-dB range of signal powers tested, as shown in figure 5.9.

Bandwidth

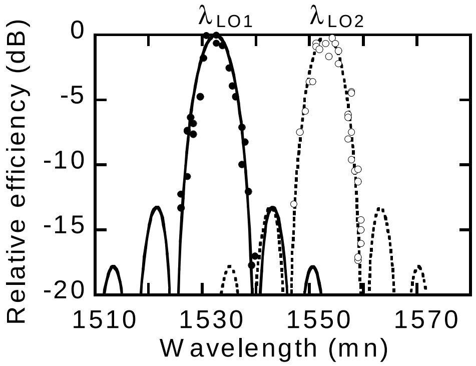

Figure 5.10 The bandwidth of a 1.3/1.5-μm-band bi-directional device at two different local oscillator wavelengths, 717.9 nm and 718.2 nm.

The 1.3/1.5-μm-band device has a 3-dB bandwidth of ~6 nm, which is about one-tenth of that in the 1.5-μm-band device. Hence with a fixed local oscillator wavelength, it can accommodate only a limited number of signal channels for 1.3/1.5-μm-band conversion. The narrower bandwidth is due to the off-degenerate operation, in contrast to the near-degenerate operation for the 1.5-μm-band device. However, a very wide (but not simultaneous) signal bandwidth is accessible using a tunable local oscillator, since any input signal wavelength (channel) can be phasematched to a particular local oscillator wavelength using a fixed QPM period. Figure 5.10 shows the signal bandwidth of a single-channel device at two different local oscillator wavelengths. The signal phasematching wavelengths are shifted about 20 nm by tuning the local oscillator wavelength about 0.3 nm.

Summary

The bi-directional 1.3/1.5-μm-band wavelength converter demonstrated in this section shows conversion efficiency – 9 dB by using coupled local oscillator power 40 mW, and has a signal dynamic range tested to be more than 50 dB. (In section 7.1, another device showing a conversion efficiency of –7 dB by using coupled local oscillator power~50 mW is illustrated.) Higher conversion efficiency can be expected with higher local oscillator power and further device improvement in the future, similar to those described for 1.5-μm-band devices in the previous sections.

5.4 1.5-μm-Band Wavelength Conversion Based on $\chi^{(2)}:\chi^{(2)}$: Co-Propagating Scheme

Introduction

DFM devices for 1.5-μm-band wavelength conversion currently require a single-mode local oscillator with 50-100 mW of power operating in the wavelength range of 750-800 nm, which is a less convenient laser source compared to the well developed 1.5-μm sources for telecommunication applications. In this section, we demonstrate wavelength conversion in $LiNbO_3$ waveguides by use of $\chi^{(2)}:\chi^{(2)}$ mixing, where both the local oscillator and input signal are in the 1.5-μm-band. Mode matching in this case is also simplified compared to DFM, since all input wavelengths are in the same band and can be launched into a single port.

$\chi^{(2)}:\chi^{(2)}$ mixing with co-propagating beams involves the simultaneous frequency-mixing processes of SHG and DFM. The local oscillator at frequency ω_{LO} is up-converted to frequency $2\omega_{LO}$ by SHG via the second-order nonlinear susceptibility $\chi^{(2)}$. The generated $2\omega_{LO}$ is simultaneously mixed with the input signal ω_s to generate a wavelength-shifted output $\omega_{out}=2\omega_{LO} - \omega_s$ by DFM via another $\chi^{(2)}$ process. It is interesting to note that this $\chi^{(2)}:\chi^{(2)}$ process mimics FWM that uses the third-order nonlinear susceptibility $\chi^{(3)}$. The effective $\chi^{(3)}$ of such a process in $LiNbO_3$ under QPM conditions is 10^4 to 10^5 times larger than that of silica glass. $\chi^{(2)}:\chi^{(2)}$ mixing allows the use of a very short sample compared to fiber FWM and is immune to parasitics such as SBS, and has better noise figure compared to FWM in semiconductor optical amplifiers.

Device Fabrication

The APE-PPLN waveguide used in this experiment is 5-cm-long, has a QPM period of 14.7 μm, waveguide width of 12 μm, proton exchange depth of 0.7 μm, and was annealed for 26 hours at 325 °C. The above parameters allow phasematching at room temperature between the fundamental mode of the local oscillator at ~1534 nm and the fundamental mode of the SHG wave, at 767 nm. The normalized efficiency of this device is 50-60%/W-cm^2 which has typical waveguide propagation losses of 0.35 dB (0.7 dB) at wavelength of 1550 nm (780nm). At the input and output of this device, the waveguides are optimized for fiber coupling by tapering a 1-mm-long section to adiabatically transform the modes into and out of the wavelength conversion sections. The devices are fiber-pigtailed and show a typical fiber-to-fiber loss of 3-3.5 dB.

Experimental Setup

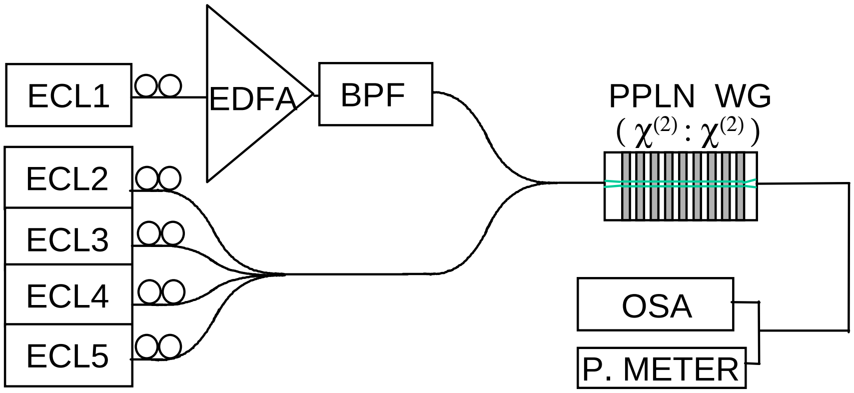

Figure 5.11 Experimental setup. ECL: external cavity laser; BPF: band pass filter; PPLN WG: periodically poled $LiNbO_3$ waveguide; OSA: optical spectrum analyzer. The waveguide is fiber coupled at both the input and output. An OSA and a power meter are used to analyze the output of the waveguide.

Figure 5.11 shows a schematic diagram of the experimental setup used in this work. The local oscillator laser is an ECL amplified by an EDFA to a level of 200-300 mW and filtered through a band pass filter in order to suppress the amplified-spontaneous emission. This local oscillator is combined with signal sources generated in four different ECL's, then launched into the waveguides through a fiber. The output of the waveguide is filtered by a fiber Bragg grating to reject the residual 1.5-μm-band local oscillator and then analyzed by an optical spectrum analyzer (OSA) and a power meter. During the measurement, the devices are maintained at 120 °C to avoid photorefractive effects.

Multi-Channel Conversion and Signal-to-Noise Ratio (SNR)

In $\chi^{(2)}:\chi^{(2)}$ mixing, the conversion efficiency is related to the normalized efficiency of device and local oscillator power by equation (2.26):

$$\eta \ \text{(dB)} \approx 10\log\left(\frac{1}{4}\eta_{norm}^2 L^4 P_{LO}^2\right). \qquad \text{(for } \eta_{norm} L^2 P_{LO} < 1\text{)} \tag{5.4}$$

The power conversion efficiency ($=P_{out}/P_s$) is proportional to the square of the local oscillator power and the normalized efficiency in the limit of low conversion efficiency. The quadratic dependence is due to the cascaded wave-mixing process. At higher conversion efficiencies, due to significant local oscillator depletion in the SHG process and significant signal parametric gain, numerical integration should be used as described in Chapter 2.

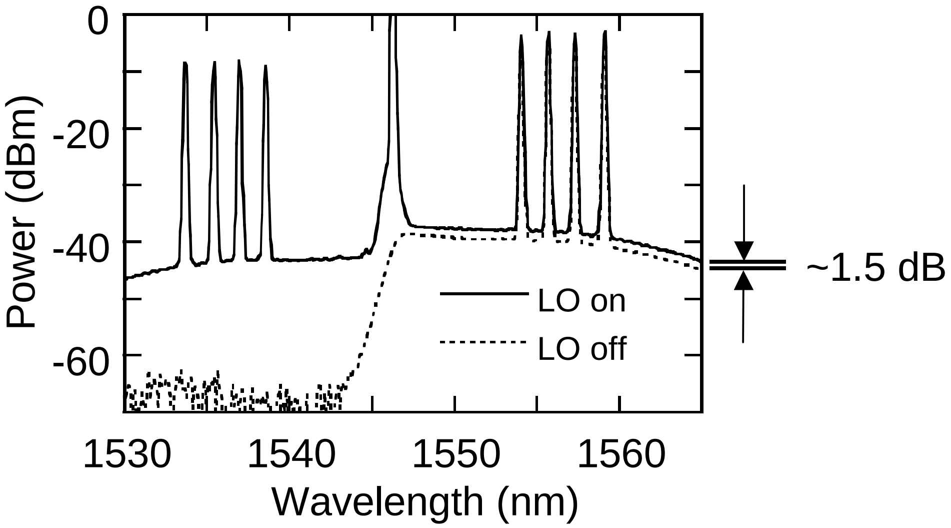

Figure 5.12 Spectral inversion and simultaneous wavelength conversion of four WDM channels with the same conversion efficiency. The original channels lie on the right-hand side of the local oscillator peak.

A typical spectrum of the original and spectrally inverted channels is shown in figure 5.12. The internal (external, fiber to fiber) conversion efficiency for a local oscillator power of ~100 mW is –10 dB (–13.5 dB). When the local oscillator power is raised to ~200 mW, the efficiency rises to -5 dB (–7 dB). The power level differences between the solid line and the dashed line on the right-hand side of the plot is the signal parametric gain (1.5-2 dB) for this conversion process, indicating that the conversion process is very efficient. Also note that the SNR of the converted channels is about the same as that of the input channels. The SNR degradation of this device intrinsically is limited only by quantum noise. In practice, the stability and noise of the local oscillator source dominate the SNR.

Spectral Inversion

For $\chi^{(2)}$:$\chi^{(2)}$-based wavelength converters, the converted output electric field is the complex conjugate of the signal electric field. That is, the output electric field spectrum is the mirror image of input spectrum relative to the local oscillator wavelength. This feature can be used to invert the signal chirp for dispersion management in a transmission system. Figure 5.13 shows the spectral inversion properties of such type of device. By combining an ECL signal with the filtered ASE from an EDFA, a distorted signal spectrum is formed to demonstrate the effect.

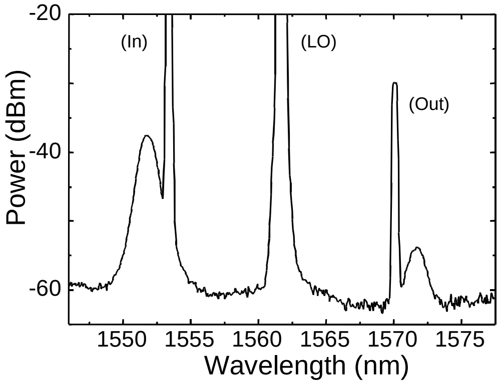

Figure 5.13 Spectral inversion of $\chi^{(2)}:\chi^{(2)}$–based wavelength converter. The output electric field spectrum is the mirror image of input spectrum relative to the local oscillator frequency.

Bandwidth

$\chi^{(2)}:\chi^{(2)}$-mixing process also has a wide signal bandwidth because of the near-degenerate DFM process. Figure 5.14 shows the measured bandwidth of this wavelength converter when the input signal wavelength is tuned while the local oscillator wavelength is fixed at 1550 nm. This device has a 3-dB signal bandwidth of 70 nm, which is wider than the theoretical bandwidth of an ideal (lossless) 5-cm-long device due to some residual photorefractive effects at high local oscillator powers.

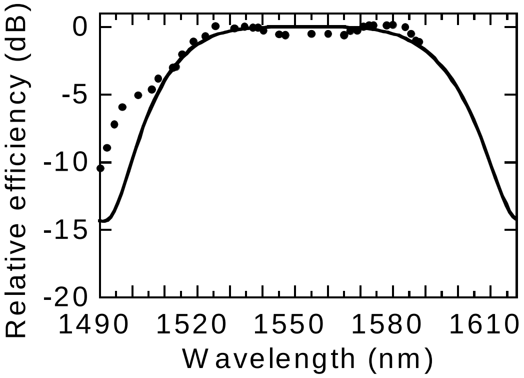

Figure 5.14 Relative conversion efficiency as a function of the input signal wavelength. The closed circles are measured results and the solid line is the theoretical fit (~15% wider than the theoretical prediction).

Linearity

The device has the same conversion efficiency over a wide signal power range. The deviation from the linearity comes from the depletion of the generated SHG power. We tested the linearity of this wavelength converter by varying the input signal power, as shown in figure 5.15. The device has a linear response for an input signal power over the tested range of more than 50 dB, with the maximum input signal power of ~0 dBm.

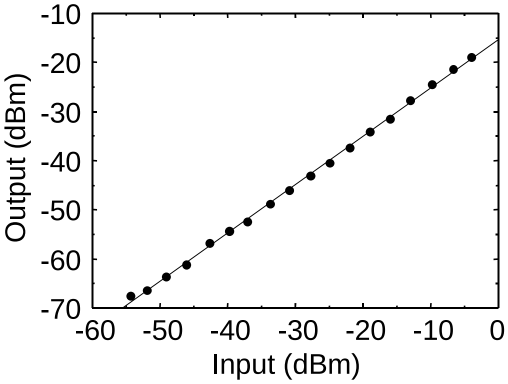

Figure 5.15 Single-channel output/input transfer curve of a $\chi^{(2)}:\chi^{(2)}$-based wavelength converter. This device has a linear response for more than 50-dB range of input signal power. LO power of 100 mW was used in this measurement.

Summary

In this section, we have shown wavelength conversion within the 1.5-μm-band using $\chi^{(2)}:\chi^{(2)}$ mixing in PPLN waveguides. This approach requires only lasers operating in the 1550-nm region. Spectral inversion and simultaneous conversion of four WDM channels, -7-dB fiber-to-fiber conversion efficiency, no significant SNR degradation in the conversion process, a conversion bandwidth of 70 nm, and a linearity over an input power range of more than 50 dB were shown.

5.5 1.5-μm-Band Wavelength Conversion Based on $\chi^{(2)}:\chi^{(2)}$: Counter-Propagating Scheme

Introduction

In $\chi^{(2)}:\chi^{(2)}$-based wavelength conversion using co-propagating local oscillator and signal beams, considerable local oscillator power is present at the output of the waveguide and consequently an appropriate blocking filter must be used. In this section, we demonstrate a wavelength converter that uses counter-propagating local oscillator and signal beams [18, 29]. This configuration improves the overall conversion efficiency and alleviates the local oscillator rejection requirements.

$\chi^{(2)}:\chi^{(2)}$-based device using counter-propagating beams is implemented by launching the local oscillator and signal beams from opposite facets of the waveguide. One facet is coated with a dichroic dielectric mirror that reflects the second-harmonic beam back into the waveguide. In this device, the local oscillator at frequency ω_{LO} is up-converted to frequency $2\omega_{LO}$ by SHG. The generated $2\omega_{LO}$ is reflected back into the waveguide and mixed with the input signal ω_s for co-propagating phasematching to generate a wavelength-shifted output $\omega_{out}=2\omega_{LO} - \omega_s$ by DFM. Phasematching between the interacting waves for both SHG and DFM is required, and can be accomplished by choosing an appropriate QPM grating period. Phasematching with counter-propagating beams is in principle possible but the poling period required is extremely small (<1 μm) and thus not easily fabricated, and the DFG bandwidth is very narrow.

Device Fabrication

The PPLN waveguide used in this experiment consists of a 4-cm-long interaction section, has a phasematching wavelength of 1548 nm (~1560 nm) at room temperature (120 °C). Efficient fiber coupling is achieved by introducing extra 1-mm taper regions at the input and output of the waveguides. We then coated one facet by e-beam deposition with a dielectric 6-layer stack of Al_2O_3 and SiO_2. This mirror had a reflectivity of ~96% at 780 nm and ~1% at 1550 nm.

Experimental Setup

Figure 5.16 shows the experimental setup used in this work. The local oscillator laser is an external cavity diode laser amplified by an EDFA to a level of ~100-200 mW. The signal channel is provided by another ECL and is launched from the coated side of the waveguide through a fiber. The converted output is collected through a circulator. The total loss in the signal path, including isolator, coupling and propagation losses, and circulator is 5.6 dB. The waveguide-related losses (e.g. coupling loss plus waveguide propagation losses) are ~3.3 dB.

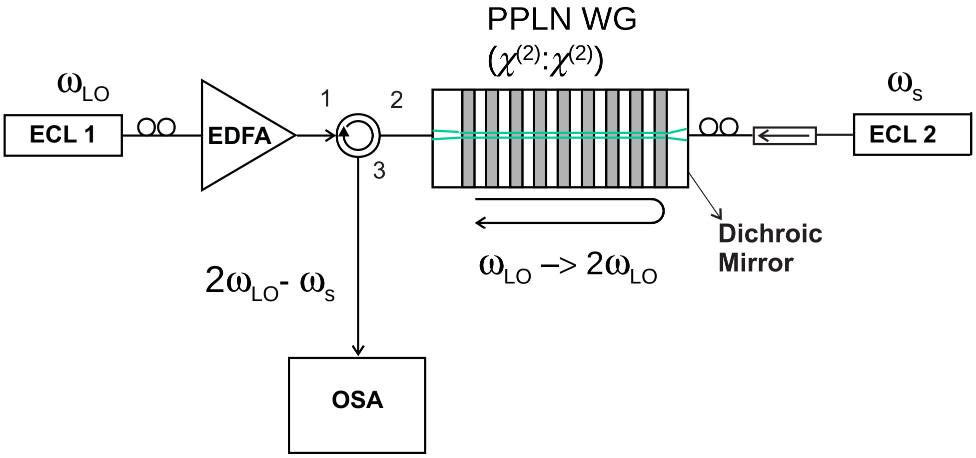

Figure 5.16 Experimental setup for the wavelength converter based on cascaded second-order nonlinear frequency mixing with counter-propagating beams. ECL: external cavity laser; PPLN WG: periodically poled $LiNbO_3$ waveguide; EDFA: Erbium-doped-fiber amplifier; OSA: optical spectrum analyzer.

Conversion Results

The conversion efficiency is related to the normalized efficiency of device and the local oscillator power by equation (2.30)

$$\eta \text{ (dB)} \approx 10\log\left(\eta_{norm}^2 L^4 P_{LO}^2\right). \qquad \text{(for } \eta_{norm} L^2 P_{LO} < 1\text{)} \tag{5.5}$$

One major advantage of the counter-propagating scheme over the co-propagating scheme can be easily observed by comparing equation (5.5) and equation (5.4). There is about a factor of 4 or a 6-dB improvement in the power conversion efficiency for the same device parameters and local oscillator power, since the counter-propagating scheme effectively uses the device length twice. In practice, the improvement is a function of the length of the device due to the limitation of waveguide propagation losses.

A typical trace measured at port 3 of the circulator is shown in figure 5.17. The converted signal is denoted by A'. Wavelength conversion efficiency of ~-12 dB was achieved with local oscillator power of ~120 mW (coupled local oscillator power of 90 mW). A good suppression (without any filter) of the local oscillator left after the conversion process can be seen from the plot.

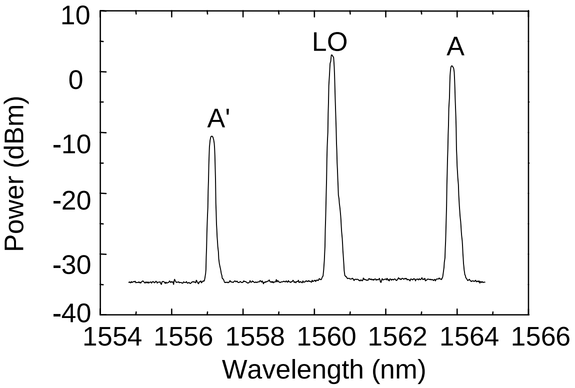

Figure 5.17 A typical trace measured at port 3 of the circulator for single-channel wavelength conversion. Local oscillator power ~120 mW. Note the good rejection (without filter) of the remaining local oscillator power due to the counter-propagating geometry.

We then varied the signal wavelength and measured the conversion efficiency for a fixed local oscillator wavelength (1559 nm) and power (110 mW). This device has a 3-dB signal bandwidth of 68 nm. The linearity of this device in signal power is similar to that for the $\chi^{(2)}$:$\chi^{(2)}$-based device with co-propagating beams.

5.6 Comparison between Different Conversion Schemes

To evaluate the performance of $\chi^{(2)}$-based wavelength converters using these three different schemes, we plot the calculated conversion efficiency vs. device length. Figure 5.18 shows the plots under three different normalized efficiencies, at the coupled signal power of 1 mW, and the coupled local oscillator power of 100 mW and 200 mW respectively. Waveguides with propagation losses of 0.35 dB/cm (0.7 dB/cm) at wavelength of 1550 nm (780 nm) are assumed. The DFM process has the best conversion efficiency because it is a direct $\chi^{(2)}$ process. But this scheme has more complicated input-coupling requirements. The co-propagating $\chi^{(2)}$:$\chi^{(2)}$-based device has a lower conversion efficiency than DFM device, however, it allows the use of a local oscillator in the 1.5-μm-band and therefore the input coupling is easier. The counter-propagating $\chi^{(2)}$:$\chi^{(2)}$-based device has a higher conversion efficiency than the co-propagating $\chi^{(2)}$:$\chi^{(2)}$-based device for lengths less than ~6 cm, since it actually uses about twice the device interaction length. However, for longer devices, the co-propagating device has a better efficiency than the counter-propagating method. Thus, in a short device it is better to generate the SHG field first and then use it for DFM. Longer devices are dominated by waveguide losses and the situation is reversed.

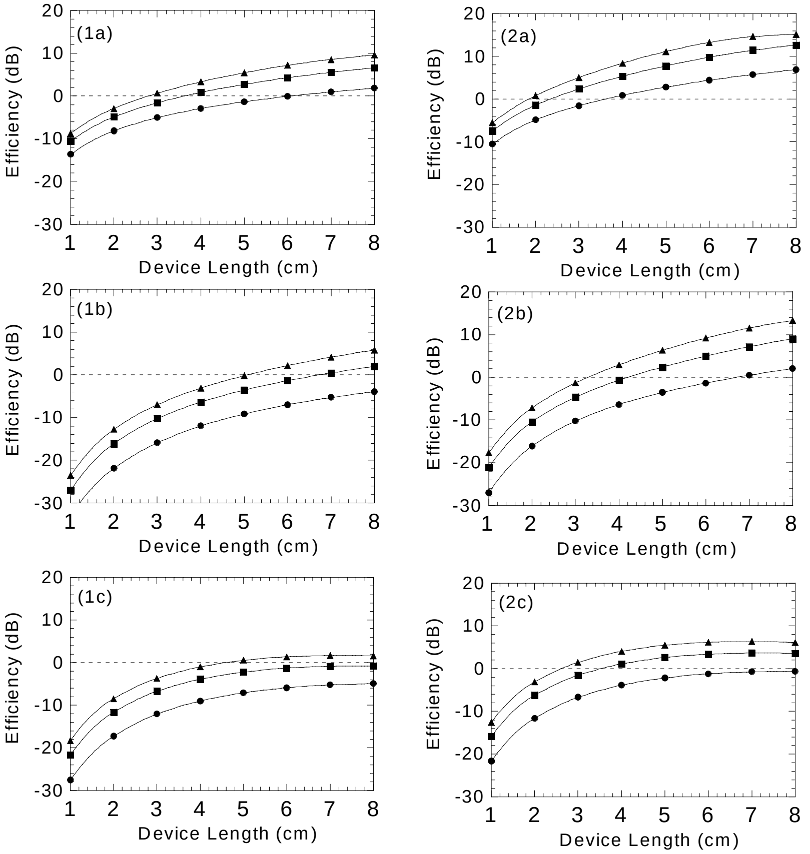

Figure 5.18 Comparison of three different conversion schemes for three different normalized efficiencies at coupled signal power of 1 mW and coupled local oscillator power of 100 mW and 200 mW respectively. Waveguides with propagation losses of 0.35 dB/cm (0.7 dB/cm) at wavelength of 1550 nm (780 nm) are assumed in the calculation. (a), (b), and (c) represent DFM, $\chi^{(2)}:\chi^{(2)}$ co-propagating and counter-propagating schemes, respectively. (1a), (1b) and (1c) are with 100 mW and (2a), (2b), and (2c) are with 200 mW of coupled local oscillator power. The conversion efficiency is internal conversion efficiency, i.e. without taking account of waveguide to fiber coupling loss. Normalized efficiency: ▲ 150%/W-cm^2 ■ 100%/W-cm^2 ● 50%/W-cm^2

With further development in the waveguide fabrication process, one can expect further improvements in the waveguide propagation losses and normalized efficiency. Thus it is interesting to plot conversion efficiency for some ideal (lossless) situations. Figure 5.19 shows conversion efficiency for three different normalized efficiencies in lossless waveguides. In the extreme case (8-cm-long waveguide and 150%/W-cm^2 normalized efficiency), about 15-dB conversion gain can be achieved with a coupled local oscillator power 100 mW in both DFM and $\chi^{(2)}:\chi^{(2)}$ mixing. Under this circumstance the conversion efficiency is limited by the depletion of local oscillator power.

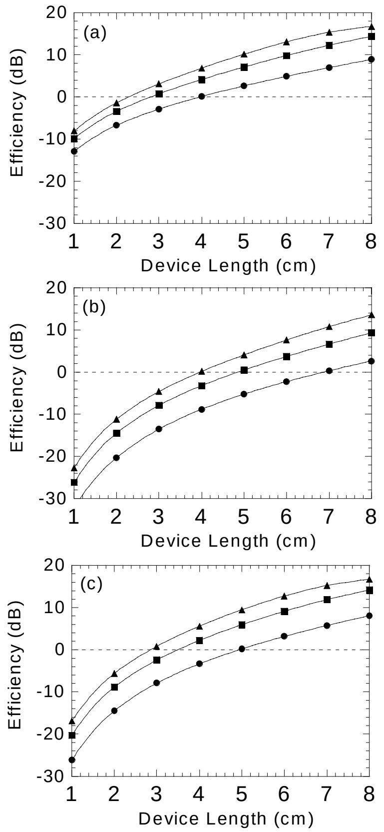

Figure 5.19 Comparison of three different conversion schemes for three different normalized efficiencies at coupled signal power of 1 mW and coupled local oscillator power of 100 mW. Lossless waveguides are assumed in this calculation. (a), (b), and (c) represent DFM, $\chi^{(2)}:\chi^{(2)}$ co-propagating and counter-propagating schemes, respectively. ▲ 150%/W-cm^2 ■ 100%/W-cm^2 ● 50%/W-cm^2

5.7 Polarization Dependence

While checking the issues illustrated in figure 5.2 for an all-optical wavelength converter, one can find that the major remaining issue associated with our demonstrated devices is the polarization dependence. Polarization dependence is not favorable in practical communication systems, thus this issue needs to be addressed for practical applications. Figure 5.20 shows two feasible approaches based on polarization diversity. In the first approach (figure 5.20(a)), the two polarization states are separated by a polarizing-beam splitter (PBS). One path uses a half-wave plate in order to rotate the polarization to the TM state. The outputs from each arm are launched into the device from opposite sides; the converted output is taken from port 3 of the circulator. This scheme is very attractive for the $\chi^{(2)}:\chi^{(2)}$ mixing using co-propagating beams. In this scheme, two different polarization states are passing through the same optical path, and polarization mode dispersion (PMD) would not exist. In the second scheme (figure 5.20(b)), two PBS's are needed and each polarization is coupled into a different waveguide with the required polarization. If the waveguides are on the same chip, then they will have identical characteristics. The major drawback is that it will require some effort to balance the length of the two optical paths.

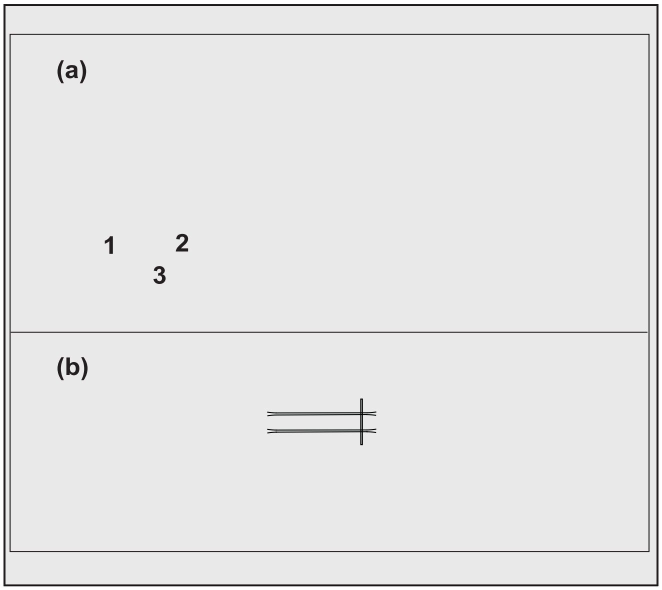

Figure 5.20 Two different schemes for fabricating polarization insensitive devices.

5.8 Summary

In this chapter, we have investigated OF mixers as WDM wavelength converters using three different schemes: difference-frequency mixing, cascaded second-order nonlinear frequency mixing using co-propagating beams and cascaded second-order nonlinear frequency mixing using counter-propagating beams. The results show several attractive characteristics of $\chi^{(2)}:\chi^{(2)}$-based converters for WDM applications. In checking the tractable issues illustrated in figure 5.2, it can be found that the device can well address most of the requirements and is very suitable as a component in WDM wavelength conversion nodes. Future work will involve correction for polarization dependence, reduced operating temperature and increased efficiency. With further device improvement, 0-dB conversion efficiency or conversion with gain can be expected in the near future with moderate local oscillator power.

Reference for Chapter 5:

1. C. A. Brackett, A. S. Acampora, J. Sweitzer, G. Tangonan, M. T. Smith, W. Lennon, K.–C. Wang, R. H. A. Hobbs, “Scalable multiwavelength multihop optical network: a proposal for research on all-optical networks,” *IEEE J. Lightwave Technol.* **11**, 736-753 (1993).
2. R. Ramaswami and K. N. Sivarajan, *Optical Networks: A Practical Perspective*, Morgan Kaufmann, San Francisco, 1998.
3. K. C. Lee and V. O. Li, “A wavelength-convertible optical network,” *IEEE J. Lightwave Technol.* **11**, 962-970 (1993).
4. S. J. B. Yoo, “Wavelength conversion technologies for WDM network applications,” *J. Lightwave Technol*. **14**, 955-966 (1996).
5. X. N. Antoniades, K. Bala, S. J. B. Yoo, and G. Ellinas, “A parametric wavelength interchanging cross-connect (WIXC) architecture,” *IEEE Photon. Technol. Lett.* **8**, 1382-1384 (1996).
6. D. Norte and A. E. Willner, “All-optical data format conversion and reconversions between the wavelength and time domains for dynamically reconfigurable WDM networks,” *J. Lightwave Technol*. **14**, 1170-1182 (1996).
7. S. L. Danielsen, P. B. Hansen, K. E. Stubkjaer, “Wavelength conversion in optical packet switching,” *J. Lightwave Technol*. **16**, 2095-2108 (1998).
8. K. E. Stubkjaer, A. Kloch, P. B. Hansen, H. N. Poulsen, D. Wolfson, K. S. Jepsen, A. T. Clausen, E. Limal, A. Buxens, “Wavelength converter technology,” *IEICE Trans. on Communications.* **E82-B**, 390-400 (1999).
9. J. M. Wiesenfeld, “Wavelength conversion in WDM networks,” *LEOS'97*, pp. 88-89; “Wavelength conversion for all-optical networks,” *IPR’96*, pp. 143-146.
10. A. E. Willner (University of Southern California), *OMC review talk* 1999.
11. S. J. B. Yoo, M. A. Koza, C. Caneau, and R. Bhat, “Simultaneous wavelength conversion of 2.5-Gbit/s and 10-Gbit/s signal channels by difference-frequency generation in an AlGaAs waveguide,” *OFC’98*, WB5.
12. S. J. B. Yoo, C. Caneau, R. Bhat, M. A. Koza, A. Rajhel, and X. N. Antoniades, “Polarization-independent, multichannel wavelength conversion by difference frequency generation in quasi-phase-matched AlGaAs waveguide,” *CLEO’96*, JTuE1.
13. S. J. B. Yoo, R. Bhat, C. Caneau, and M. A. Koza, “Multichannel polarization-independent wavelength conversion by difference-frequency generation in AlGaAs waveguide,” *CLEO’97*, CMF3.
14. S. J. B. Yoo, C. Caneau, R. Bhat, M. A. Koza, A. Rajhel, N. Antoniades, “Wavelength conversion by difference frequency generation in AlGaAs waveguides with periodic domain inversion achieved by wafer bonding,” *Appl. Phys. Lett.* **68**, 2609-2611 (1996).

---

15. C. Q. Xu, H. Okayama, and M. Kawahara, “1.5 μm band efficient broadband wavelength conversion by difference frequency generation in a periodically domain-inverted $LiNbO_3$ channel waveguide,” *Appl. Phys. Lett.* **63**, 3559-3561 (1993).
16. M. L. Bortz, D. Serkland, M. M. Fejer, and S. J. B. Yoo, “Near degenerate difference frequency generation at 1.3 μm in $LiNbO_3$ waveguides for application as an all-optical channel shifter,” *CLEO’94*, CTHD6.
17. M. H. Chou, J. Hauden, M. A. Arbore, and M. M. Fejer, “1.5 μm band wavelength conversion based on difference frequency generation in $LiNbO_3$ waveguides with integrated coupling structures,” *Opt. Lett.* **23**, 1004-1006 (1998).
18. K. Gallo, G. Assanto, and G. Stegeman, “Efficient wavelength shifting over the erbium amplifier bandwidth via cascaded second order processes in lithium niobate waveguides,” *Appl. Phys. Lett.* **71**, 1020-1022 (1997).
19. I. Brener, M. H. Chou, and M. M. Fejer, “Efficient wideband wavelength conversion using cascaded second-order nonlinearities in $LiNbO_3$ waveguides,” *OFC’99*, FB6.
20. C. G. Treveno-Palcios, G. I. Stegeman, P. Baldi, and M. P. De Micheli, “Wavelength shifting using cascaded second-order processes for WDM applications at 1.55 μm,” *Electron. Lett.* **34**, 2157 (1998).
21. M. H. Chou, I. Brener, M. M. Fejer, E. E. Chaban, and S. B. Christman, “1.5-μm-band wavelength conversion based on cascaded second-order nonlinearity in $LiNbO_3$ waveguides,” *Photonics Technol. Lett.* **11**, 653-655 (1999).
22. K. Gallo and G. Assanto, “Analysis of lithium niobate all-optical wavelength shifters for the third spectral window,” *J. Opt. Soc. Am. B.* **16**, 741-753 (1999).
23. The device includes integrated waveguide structures for efficient mode coupling and has a 41-mm-long wavelength conversion section with a QPM grating period of 14.75 μm. The structure is shown in **Figure 4.2(a)**. The separation between two input waveguides optimized for fiber-pigtailing is 250 mm. The mode filter for local oscillator wavelength is 2-mm-long with waveguide mask width of 1.8 μm, the taper is 4-mm-long with mask width varying smoothly from 1.8 to 7.6 μm. The mode filter for the signal wavelength is 1-mm-long with mask width of 3.6 μm, the taper is 1-mm-long with mask width varying from 3.6 to 7.6 μm, and the bend with raised-cosine function is 4.5-mm-long. The directional coupler is 4-mm-long with a 10.5-μm center-to-center separation. The second taper is 1.25-mm-long with mask width varying from 7.6 to 12 μm. The DFM region is 41-mm-long with mask width of 12 μm. The output port consists of a 1-mm-long taper and 0.8-mm-long mode-coupling waveguide. The whole device length is 56 cm. We chose an initial proton exchange depth of 0.71 μm and annealing time of 26 hours at 325 °C.

24. M. Zirngibl, C. H. Joyner, L. W. Stulz, C. Dragone, H. M. Presby, I. P. Kaminow, "LARnet, a local access router network, " *IEEE Photon. Technol. Lett.* **7**, 215-217 (1995).

25. See special feature on "Technologies for economical optical access system components," NTT Rev. **9,** 44-85 (1997).

26. C. Q. Xu, H. Okayama, and M. Kawahara, "Wavelength conversions between the two silica fibre loss windows at 1.31 and 1.55 μm using difference frequency generation," *Electron. Lett.* **30**, 2168-2170 (1994).

27. M. H. Chou, K. R. Parameswaran, M. A. Arbore, J. Hauden, and M. M. Fejer, "Bi-directional wavelength conversion between 1.3 and 1.5 μm telecommunication bands using difference frequency mixing in $LiNbO_3$ waveguides with integrated coupling structures," *CLEO'98*, CThZ2.

28. The device has a QPM period of 11.5 μm, waveguides were formed by proton exchange to a depth of 0.55 μm, followed by annealing at 320 °C for 13 hours. The integrated device consists of a 2.5-mm-long mode filter (with segmentation period of 10 μm and duty cycle of 28%), a 5-mm-long periodically segmented taper, a 2-mm-long directional coupler, and a 33-mm-long wavelength converter.

29. I. Brener, M. H. Chou, D. Peale, and M. M. Fejer, "Cascaded $\chi^{(2)}$ wavelength converter in $LiNbO_3$ waveguides with counter-propagating beams," accepted by *Electron. Lett.* (1999).

CHAPTER 6

OPTICAL FREQUENCY MIXERS FOR DISPERSION COMPENSATION IN FIBER LINKS

6.1 Introduction

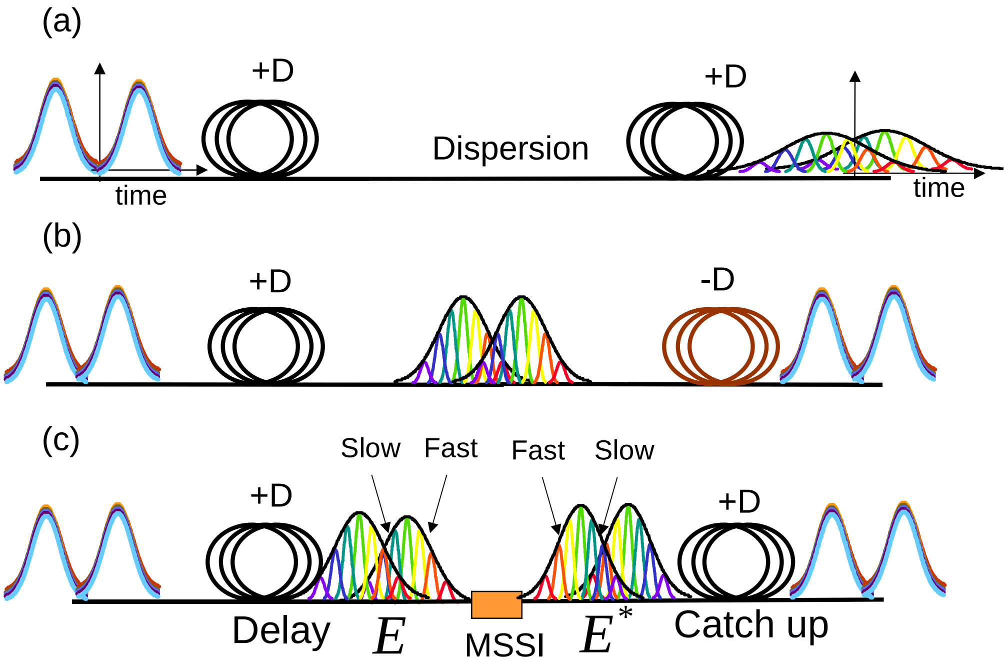

Figure 6.1 Schematic drawing of dispersion and dispersion compensation of fiber links. (a) Signals transmitted in optical fibers will get distorted after a significant distance due to chromatic dispersion, so two adjacent bits will interfere with each other. (b) Dispersion compensation fiber has an opposite dispersion to the other section of fiber and results in an averaged zero dispersion. (c) Mid-span spectral inverter (MSSI) inverts the signal chirp in the middle point of fiber links and results in an undistorted signal at receiver.

One of the most troublesome issues in high capacity optical fiber transmission is the accumulated dispersion of fiber links. When the modulated signal propagates in an optical fiber, different spectral components of the transmitted signal generally travel at different velocities and thus cause signal pulse distortion after a significant distance. A schematic drawing of the dispersion phenomenon is shown in figure 6.1(a). Due to chromatic dispersion, two adjacent bits will interfere with each other and result in a closed eye after a long transmission distance. For a system operated at rate B Gbits/s, the maximum transmission distance L km is limited by the dispersion D ps/km-nm according to the relation

$$L < \frac{104{,}000 \;\; Gbits^2 / ps - nm}{DB^2} \tag{6.1}$$

For example at 40 Gbits/s, the maximum transmission distance is about 4 km over standard single mode fiber (SMF, D=17 ps/km-nm).

To increase transmission distance, several techniques (such as dispersion compensating fibers (DCF) [1], chirped fiber gratings [2, 3, 4], mid-span spectral inversion (MSSI) [5, 6, 7, 8], etc.) have been used to compensate the accumulated dispersion. In the dispersion compensation fiber technique as illustrated in figure 6.1(b), the dispersion accumulated in one span of a fiber is negated by the opposite dispersion accumulated in another span of a fiber. An optical element that provides the opposite chirp or generates an optical phase-conjugated signal can also be used to cancel out the accumulated dispersion. Figure 6.1(c) shows a schematic description of the mid-span spectral inverter. The mid-span spectral inverter performs spectral inversion of the signals at the middle point of the transmission fiber line. The slow (fast) running wavelengths of a pulse are converted into the fast (slow) running wavelengths. Hence the delayed spectral components catch up to the faster components in the second half of the fiber link and the signal at the receiver end is undistorted.

Among different dispersion compensation techniques, MSSI provides several advantages. MSSI does not require accurate knowledge of the dispersion of each fiber section, as long as the middle point of the total fiber span is accessible and the two resulting halves produce similar accumulated dispersion. MSSI has a natural appeal at high bit rates, since it is usually implemented using some sort of optical nonlinearity (typically four-wave mixing (FWM)) of an instantaneous nature. Previous implementations of MSSI were based on FWM in semiconductor optical amplifiers (SOA's) [6] or optical fibers [7]. The approach in SOA's suffers from an intrinsic noise in the form of amplified spontaneous emission (ASE) originating in the SOA's. Furthermore, both approaches typically have low conversion efficiency (<-15 dB). In this chapter, we will investigate the application of OF mixers as MSSI and demonstrate their performance for 4x10 Gbits/s transmission over a 150-km standard single-mode fiber.

6.2 MSSI in Periodically Poled LiNbO$_3$ (PPLN) Waveguides

MSSI in $\chi^{(2)}$ materials can be implemented by difference-frequency mixing (DFM) or cascaded second-order nonlinear frequency mixing ($\chi^{(2)}$:$\chi^{(2)}$ mixing) because both frequency-mixing processes can generate spectrally inverted outputs. The inverters can perform spectral inversion of multiple signal channels simultaneously, regardless of the data formats and modulation speed. In this section, we show MSSI by $\chi^{(2)}:\chi^{(2)}$ mixing with co-propagating beams in periodically poled $LiNbO_3$ (PPLN) waveguides and discuss its performance in high speed multi-channel compensation. For $\chi^{(2)}:\chi^{(2)}$ mixing, both the signal and local oscillator lie in the 1.5-μm-band. From an external point of view, this process mimics FWM in other nonlinear materials but with a large effective $\chi^{(3)}$ (the effective $\chi^{(3)}$ of a 5-cm PPLN waveguide is equivalent to that of more than a few kilometers of dispersion-shifted fiber). MSSI in PPLN waveguides has all the advantages of FWM in passive media, such as having instantaneous response and being excess noise free. In addition, it doesn't suffer from Stimulated Brillouin Scattering (SBS) which is a process that makes it difficult to launch a high power pump into fibers without back reflection. For MSSI in PPLN waveguides, zero dispersion wavelength fluctuation is inherently irrelevant and the phasematching wavelength can be further finely tuned by temperature with ~0.1 nm/°C.

Experiments and Results

The annealed proton-exchanged (APE) PPLN waveguide used in this experiment has a 5-cm-long quasi-phasematching (QPM) section. The devices are fiber pigtailed and show a typical fiber-to-fiber loss of 3-3.5 dB. Several aspects of the performance of this device have been illustrated in Section 5.3. The device has a 3-dB bandwidth of ~70 nm, and shows the same conversion efficiency for all four of the wavelength-division multiplexing (WDM) channels.

The experimental setup used for the MSSI experiment is shown in figure 6.2. Four WDM channels at 200-GHz spacing are provided by four tunable external cavity lasers (ECL’s). They are modulated in a $LiNbO_3$ modulator at 10 Gbits/s with a 2^{31}-1 pseudo-random binary sequence. The combined channels are then decorrelated in 9 km of SMF, pre-amplified to a level of 0 dBm per channel in an erbium-doped-fiber amplifier (EDFA) and launched into a 75-km standard SMF (D=17 ps/nm-km). After the fiber, another EDFA is used to restore the powers per channel to ~0 dBm. The local oscillator laser for the spectral inverter is an external cavity laser pump (ECL) amplified by an EDFA to a level of 100-200 mW and filtered through a band pass filter (BPF1) in order to suppress its ASE. The spectral inverter module can be made more compact by using a high power DFB laser as a local oscillator source. The local oscillator and signals are combined in a WDM coupler and launched copolarized into the $LiNbO_3$ waveguide. After the waveguide, the spectrally inverted channels are isolated with a broad (>5 nm) bandpass filter (BPF2), amplified and launched into a second 75-km spool of SMF. Finally, the individual channels are filtered in a narrow (0.8 nm) bandpass filter (BPF3) and detected in an optically preamplified receiver.

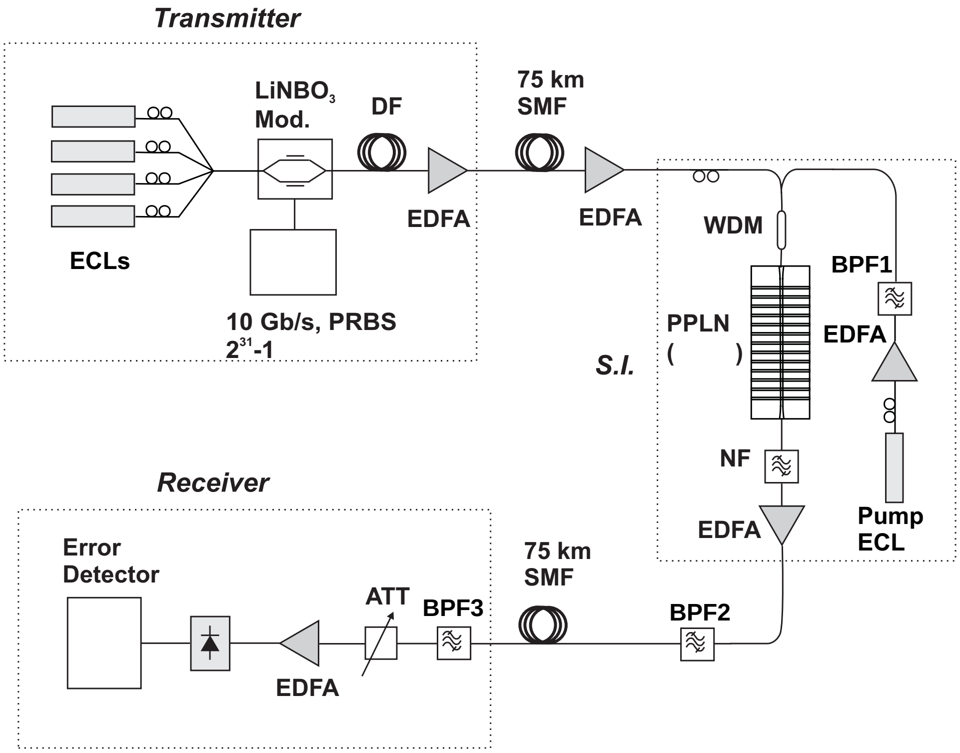

Figure 6.2 Experimental setup used to demonstrate the performance of the PPLN waveguide spectral inverter. NF: notch filter; BPF: bandpass filter; DF: decorrelation fiber.

A typical spectrum of the original and spectrally inverted channels has been shown in figure 5.12. The external (fiber-to-fiber) conversion efficiency for a local oscillator power of ~100 mW is –13.5 dB. When the local oscillator power is raised to ~200 mW, the external efficiency rises to –7 dB. This is the most efficient waveguide spectral inverter presented to date using a cw pump. A device with unity efficiency can be achieved with an improved fabrication process and a minor redesign of the waveguide structure.

The eye diagrams for one of the channels, back-to-back and after transmission through 150 km of standard SMF are shown in figure 6.3. Similar traces are obtained for all four channels. Figure 6.3(b) shows the eye diagram for the unconverted signal channel after 150 km of fiber, with the impairment due to dispersion clearly visible. When the filter is tuned to its spectrally inverted counterpart, the eye appears completely open showing the effectiveness of MSSI in counteracting the fiber dispersion.

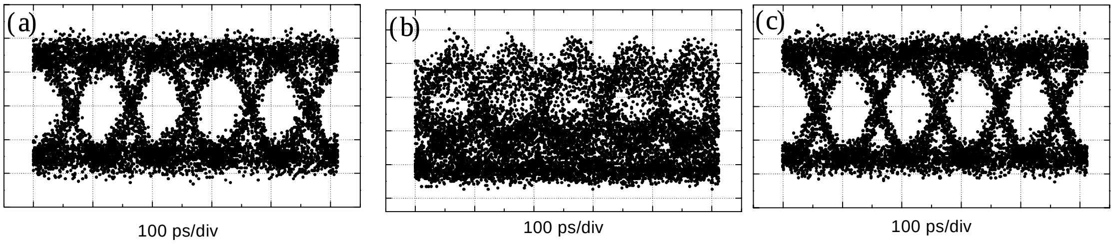

Figure 6.3 Eye diagrams for one of the channels (a) back to back; (b) unconverted after 150 km of SMF; (c) after MSSI by our device and 150 km of SMF.

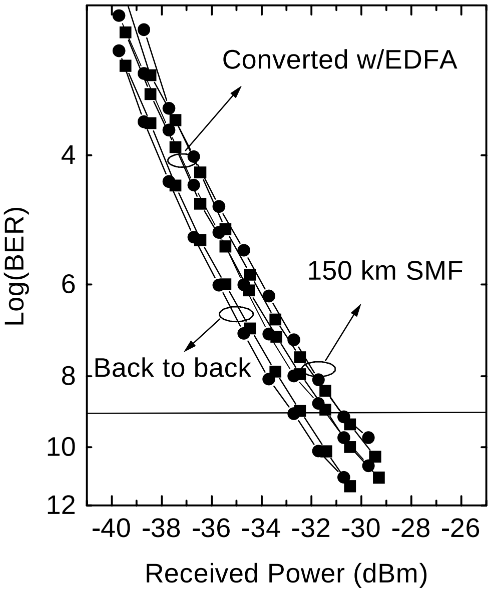

Figure 6.4 BER curves for the two center channels: back to back; after conversion in the MSSI device and amplification by one EDFA (no fiber); after MSSI and transmission through the full 150 km of SMF.

The bit error rate curves for one channel operation and the two inner channels of WDM inputs are shown in figure 6.4. For one channel operation, there is ~0.5 dB power penalty in the back-to-back measurement of the spectrally inverted channel. The additional penalty after transmission over 150 km is only ~0.5 dB. In the four WDM channels, the inner two channels represent the worst case in our 4-channel transmission system as they maximize any penalty due to nonlinearities or crosstalk of the transmission system. There is a penalty of ~1 dB in the back-to-back measurement of the spectrally inverted channels. The conversion penalty is possibly due to the use of a high power EDFA in the local oscillator path, the drift in the input polarization, and to some additional noise added by the EDFA present immediately after the waveguide device (noise figure of 8). Nevertheless, the additional penalty after transmission over 150 km is only ~0.5 dB, showing the effectiveness of dispersion compensation of this MSSI.

Discussion

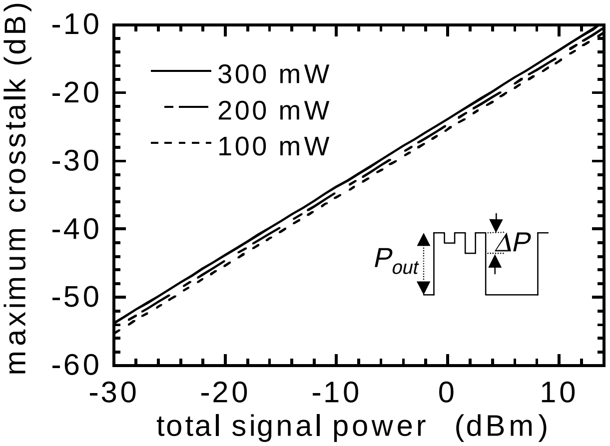

Figure 6.5 Calculated maximum crosstalk vs. total input signal power for local oscillator powers of 100, 200, and 300 mW. The maximum crosstalk is defined by 10log($\Delta P/P_{out}$).

One of the main concerns for multiple-channel operation of the current device is the crosstalk between different channels. Although this MSSI device can be characterized by an effective $\chi^{(3)}$, FWM crosstalk will not happen in the conversion process, because the conversion process is still inherently based on $\chi^{(2)}$. The crosstalk in this $\chi^{(2)}$:$\chi^{(2)}$-based spectral inverter is mainly due to pump depletion, which is less than –22 dB for less than 0-dBm input power per channel in this experiment. Note that such crosstalk, due to gain compression, is incoherent crosstalk in contrast to the coherent crosstalk that would severely distort the signal pulses. Figure 6.5 shows the calculated maximum crosstalk (or gain compression) vs. total input signal powers for local oscillator powers of 100 mW, 200 mW, and 300 mW. A device with a 5-cm-long interaction length, normalized efficiency of 50%/W-cm^2, waveguide propagation losses of 0.35 (0.7) dB/cm at wavelength of 1550 (780) nm, and fiber-waveguide coupling loss of 1 dB, is used in the calculation. The (fiber-to-fiber) conversion efficiency is about –13 dB, -7 dB, and -4 dB for local oscillator powers of 100 mW, 200 mW, and 300 mW, respectively.

The number of channels, system bit rate, and transmission distance can be increased in this device. The main limitation comes from the dispersion difference between the original wavelength and the spectrally inverted wavelength (i.e. due to finite dispersion slope of SMF). Figure 6.6(a) shows a typical SMF dispersion curve. For single-channel systems, one can perfectly compensate the dispersion by selecting an optimum spectral inversion point according to the relation

$$DL = D^{'}L^{'}, \tag{6.2}$$

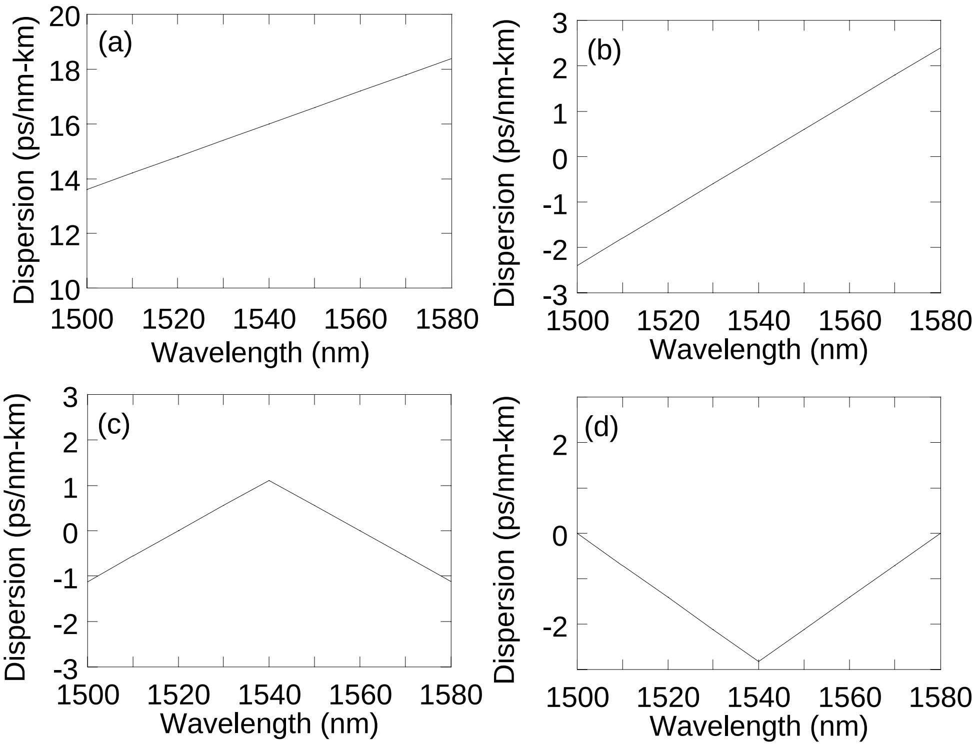

Figure 6.6 (a) Dispersion of SMF. Effective dispersion for the effective zero dispersion at wavelength of (b) 1540 nm, (c) at 1560 (1520) nm, and (d) 1580 (1500) nm.

where D and $D^{'}$ are the dispersion of the original wavelength and the spectral inverted wavelength, respectively. L and $L^{'}$ are the lengths of the two sections of the fiber link. For multiple (N) channels with a very wide wavelength span, simple mid-span spectral inversion would result in incomplete dispersion compensation for some of the channels. For channel number N with dispersion D_N for the original wavelength and $D_N^{'}$ for the spectral inverted wavelength, the effective dispersion (defined as the difference between $D_N L$ and $D_N^{'}L^{'}$) is

$$D_{eff} = \frac{1}{2}(D_N - D_N^{'}\frac{D}{D^{'}}), \tag{6.3}$$

where D and $D^{'}$ are the dispersions for the ideally compensated wavelength. The effective dispersion is a function of the wavelength (channel). Figure 6.6(b), (c), and (d) plot the effective dispersion vs. wavelength for three perfect dispersion compensation wavelengths, 1540 nm, 1560

(1520) nm, and 1500 (1580) nm, respectively. The degenerate wavelength for the MSSI is chosen to be 1540 nm in the above calculation. In a 100-channel DWDM system with 0.4-nm/channel separation, the channel number 100 is 20 nm away from the center channel. Assuming that the center channel (λ=1560 nm or 1520 nm in figure 6.6(c)) is the perfect dispersion compensated channel, this results in an effective dispersion D_{eff} ~1 ps/nm-km for channel number 100. For such a system the maximum dispersion compensation distance allowed is about 1000 km and 65 km when the system is operating at 10 Gbits/s and 40 Gbits/s, respectively. Thus a more sophisticated arrangement for the dispersion compensation will be required for a very high speed and wideband WDM system, such as using a slope compensating DCF at the receiver [7].

6.3 Summary

In this chapter, we have described the dispersion issue in fiber links for high speed transmission systems and addressed that issue by MSSI in the APE-PPLN waveguides using $\chi^{(2)}$:$\chi^{(2)}$ mixing. The device has an external (fiber-to-fiber) efficiency of -7 dB and conversion bandwidth 70 nm. We have successfully used this device in dispersion compensation of 4x10 Gbits/s channels transmitted through 150 km of SMF. Two major issues associated with multiple-channel operation are crosstalk and incomplete compensation. The availability of a compact spectral inverter with almost unity efficiency will lead to the revision of the role of spectral inversion in optical networking.

Reference for Chapter 6:

1. W. Pieper, R. Ludwig, C. M. Weinert, B. Kuhlow, G. Przyrembel, M. Ferstl, E. Pawlowski, H. G. Weber, “4-channel 40 Gb/s unrepeatered OTDM transmission over 100-km standard fiber,” *IEEE Photon. Technol. Lett.* **10**, 451-453 (1998).
2. L. Dong, M. J. Cole, A. D. Ellis, R. I. Laming, T. Widdowson, “40 Gbit/s 1.55 μm RZ transmission over 109 km of non-dispersion shifted fibre with long continuously chirped fibre gratings,” *Electron. Lett.* **33**, 1563-1565 (1997).
3. L. D. Garrett, A. H. Gnauck, F. Forghieri, V. Gusmeroli, D. Scarano, “16*10 Gb/s WDM transmission over 840-km SMF using eleven broad-band chirped fiber gratings,” *IEEE Photon. Technol. Lett.* **11**, 484-486 (1999).
4. K.-M. Feng, J.-X. Chai, V. Grubsky, D.S. Starodubov, M. I. Hayee, S. Lee, X. Jiang, A. E. Willner, J. Feinberg, “Dynamic dispersion compensation in a 10-Gb/s optical system using a novel voltage tuned nonlinearly chirped fiber Bragg grating,” *IEEE Photon. Technol. Lett.* **11,** 373-375 (1999).
5. A. H. Gnauck, and R. M. Jopson, “Optical Fiber Telecommunications IIIA,” ed. I Kaminov, T. Koch, ch. 7, p. 182, 1997.
6. U. Feiste, R. Ludwig, E. Dietrich, S. Diez, H. J. Ehrke, Dz. Razic, H. G. Weber, “40 Gbit/s transmission over 434 km standard fibre using polarization independent mid-span spectral inversion,” *Electron. Lett.* **34**, 2044-2045 (1998).
7. S. Watanabe, S. Takeda, and T. Chikama, “Interband wavelength conversion of 320 Gb/s (32x10 Gb/s) WDM signal using a polarization-insensitive fiber four-wave mixer,” in *Proc. Eur. Conf. Optical Communications*, 1998, PD Paper pp. 85-87.
8. S. Y. Set, R. Girardi, E. Riccardi, B. E. Olsson, M. Puleo, M. Ibsen, R. I. Laming, P. A. Andrekson, F. Cisternino, H. Geiger, “40 Gbit/s field transmission over standard fibre using midspan spectral inversion for dispersion compensation,” *Electron. Lett.* **35**, 581-582 (1999).

CHAPTER 7

NOVEL OPTICAL FREQUENCY MIXERS USING NON-UNIFORM QPM STRUCTURES

7.1 Introduction

In nonlinear frequency-conversion processes, the wavelength-tuning curve (i.e. conversion efficiency vs. wavelength) is related to the interacting wavelengths through the Fourier transform [1] of the spatial distribution of the effective nonlinearity [2]. Arbitrary wavelength response functions can be obtained by designing appropriate spatial grating structures. For example, aperiodic quasi-phasematching (QPM) structures have been used to broaden the second-harmonic generation (SHG) tuning curve [3, 4, 5, 6, 7] or compress the second-harmonic wave of a chirped pulse [8, 9, 10]. In this chapter, we will investigate the application of non-uniform QPM structures for multi-wavelength optical systems. We will address the instability issue and enhance signal bandwidth of difference-frequency mixing (DFM) wavelength conversion by detuning the local oscillator (LO) from the degenerate phasematching wavelength. The further bandwidth enhancement by use of non-uniform QPM structures together with local oscillator detuning is also illustrated.

7.2 Multiple-Channel OF Mixers

Principle

The devices described in the previous chapters are attractive for several optical signal-processing functions, such as wavelength conversion and dispersion compensation in wavelength-division multiplexed (WDM) optical networks, and multiplexing/demultiplexing and clock recovery in optical time-division multiplexed (TDM) systems. We defined those devices as single-channel OF mixers because they use a uniform QPM structure and have only one SHG phasematching wavelength. Single-channel OF mixers generate outputs with one-by-one parametric mappings of input signals, and are not tunable unless the device operating temperature is tuned. In some circumstances, especially in multi-wavelength communication systems, one might need to dynamically reconfigure the parametric mappings or perform functions other than one-by-one mapping; this kind of OF mixer is currently unavailable. One way to realize multiple parametric mappings is to use several discrete single-channel devices, however this is in general not practical. In this section, we describe multiple-channel OF mixers implemented by use of non-uniform QPM structures, and use the multiple-channel OF mixers to perform several advanced and novel optical signal-processing functions [11].

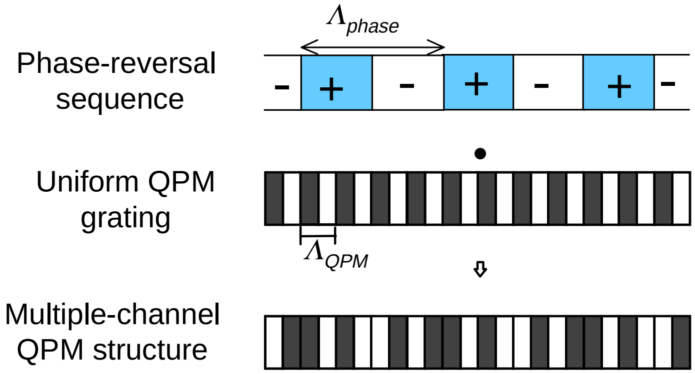

Figure 7.1 Multiple-channel QPM structure, which is formed by superimposing a phase-reversal grating on a uniform QPM grating.

Figure 7.1 illustrates the basic design principle of multiple-channel OF mixers. The multiple-channel QPM structure is designed with a phase-reversal sequence superimposed upon a uniform QPM grating. The Fourier transform of the multiple-channel QPM structure can be viewed as the convolution of a sinc function (the Fourier transform of a finite uniform grating) and a comb function due to the superimposed phase reversal sequence (with some high-order harmonics, since it is the Fourier transform of a square wave). The output power can be expressed as

$$P_{out} \approx \eta_{norm} L^2 P_{LO} P_s \left| \frac{1}{L} \int_0^L \Pi(z) \exp(-j\Delta\beta z) dz \right|^2 \tag{7.1a}$$

$$= \eta_{norm} L^2 \mathrm{P}_{LO} \mathrm{P}_s \left| \hat{\Pi}(\Delta\beta) \otimes \mathrm{sinc}(\Delta\beta L/2) \right|^2 \tag{7.1b}$$

where P_{LO}, P_s, and P_{out} are the local oscillator, input signal, and converted output powers, respectively. η_{norm} is the normalized efficiency of device in units of %/W-cm^2, which is related to the modal overlap of the interacting waves with material second-order nonlinear susceptibility, as given in equation (2.18). $\Delta\beta = \beta_{LO} - \beta_s - \beta_{out} - K_{QPM}$ is the phase mismatch among the interacting waves and the uniform QPM grating K_{QPM} (whose period is Λ_{QPM}). $\Pi(z)$ is the superimposed phase-reversal sequence and $\hat{\Pi}(\Delta\beta)$ is the Fourier transform of $\Pi(z)$. As an example of a two-channel device, let $\Pi(z)$ be a periodic phase-reversal sequence with a grating period of Λ_{phase} and a duty cycle of 50%. The superimposed phase-reversal sequence can be written as $\Pi(z)=\sum_{n=1}^{\infty}\left(\frac{2}{\pi n}\right)\sin\left(\frac{\pi n}{2}\right)\left[\exp(jK_n z)+\exp(-jK_n z)\right]$, where $K_n = 2\pi n/\Lambda_{phase}$. Inserting $\Pi(z)$ into equation (7.1) will give us equation (7.2):

$$P_{out} \approx \eta_{norm} L^2 P_s P_{LO} \sum_{n=1,3,5...}^{\infty}\left(\frac{2}{\pi n}\right)^2\left[\operatorname{sinc}^2\left(\frac{\Delta\beta + K_n}{2}L\right)+\operatorname{sinc}^2\left(\frac{\Delta\beta - K_n}{2}L\right)\right]. \tag{7.2}$$

This results in a tuning curve with two main (n=1) and some high-order harmonic (n=3,5,…) phasematching wavelengths, whose location and spacing can be engineered to conform with the International Telecommunication Union (ITU) standards.

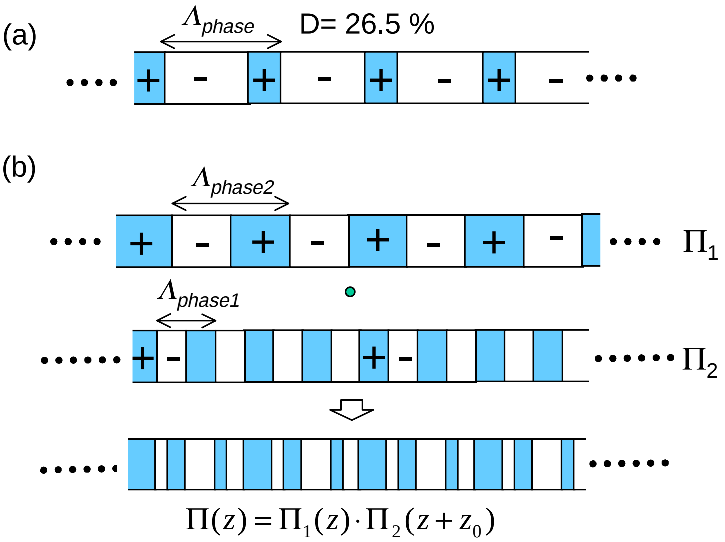

Figure 7.2 Phase-reversal sequence of (a) three-channel and (b) four-channel devices.

Two-channel devices can be designed by superimposing a phase-reversal with a duty cycle of 50% on a uniform QPM grating, which splits the one-channel tuning curve into a tuning curve with two main phasematching wavelengths and some high-order harmonics. In the case when the duty cycle is not exactly 50% (as shown in figure 7.2(a)), there will be an un-split DC term, i.e. the carrier is not fully suppressed. A three-channel device can be implemented by controlling the duty cycle of the phase-reversal sequence of a two-channel device, which changes the ratio of center-channel efficiency relative to the other two channels. The superimposed phase-reversal sequence with duty cycle of D is defined by

$$\Pi(z)=(1-2D)+\sum_{n=1}^{\infty}\frac{2}{\pi n}\sin\left[n\pi(1-D)\right]\left[\exp(jK_n z)+\exp(-jK_n z)\right]. \tag{7.3}$$

Inserting Π(z) into equation (7.1) and using the assumption Λ_{QPM} << L will yield

$$P_{out} \approx \eta_{norm} P_s P_{LO} (1-2D)^2 \operatorname{sinc}^2\left(\frac{\Delta\beta L}{2}\right)$$

$$+\eta_{norm} P_s P_{LO} \sum_{n=1}^{\infty}\left(\frac{2}{\pi n}\sin[n\pi(1-D)]\right)^2\left[\operatorname{sinc}^2\left(\frac{\Delta\beta+K_n}{2}L\right)+\operatorname{sinc}^2\left(\frac{\Delta\beta-K_n}{2}L\right)\right]. \qquad (7.4)$$

When D=26.5%, the DC term is equal to the two main split peaks with amplitude of ~22% relative to the single-channel device (D=0%).

The four-channel device is implemented by superimposing another phase-reversal sequence on a two-channel device, which splits the two channels into four. The phase-reversal sequence, as shown in figure 7.2(b), can be defined by

$$\Pi(z) = \Pi_1(z)\cdot\Pi_2(z+z_0)\,. \qquad (7.5)$$

There is a relative phase between two phase-reversal sequences to adjust the amplitude of each split peak.

Design and SHG Characterization

To demonstrate multiple-channel operation in QPM OF mixers, we designed and fabricated a set of devices by annealed proton exchange in periodically poled $LiNbO_3$ (PPLN). The device includes integrated waveguide structures for efficient mode coupling and has a 41-mm-long wavelength-conversion section with a uniform QPM grating period of 14.75 μm and superimposed phase-reversal sequences. The phase-reversal period Λ_{phase} of the two-channel device is 14 mm. The three-channel device has a phase-reversal period Λ_{phase}=7 mm and duty cycle=26.5%. The four-channel device is implemented by superimposing another phase-reversal sequence (Λ_{phase2}=14 mm) on a two-channel device (Λ_{phase1}=7 mm; the relative phase of the 14-mm-period grating with respect to the 7-mm-period grating is $2\pi z_0/\Lambda_{phase2}$=0.1364π).

We first characterized the devices by measuring SHG versus the fundamental wavelength. Figure 7.3(a) shows a normalized sinc^2 wavelength-tuning curve for a device with a single phasematching wavelength (channel) of 1550.4 nm and a peak internal nonlinear mixing efficiency of ~500%/W (output SHG power divided by the square of input fundamental power). Figures 7.3(b), 7.3(c), and 7.3(d) show the normalized tuning curves of devices with two, three, and four phasematching channels, respectively. The phasematching wavelengths are centered around 1550.4 nm and separated by ~1.6 nm (200 GHz). The efficiency for each individual channel is ~41%, 22%, and 17% relative to the one-channel device with the same interaction length in the two-, three-, and four-channel devices, respectively. The devices described in this work have several unwanted phasematching wavelengths (sidelobes of the tuning curves). These can be suppressed by optimizing the QPM grating design (for example, apodizing the QPM grating by use of digital filter design techniques).

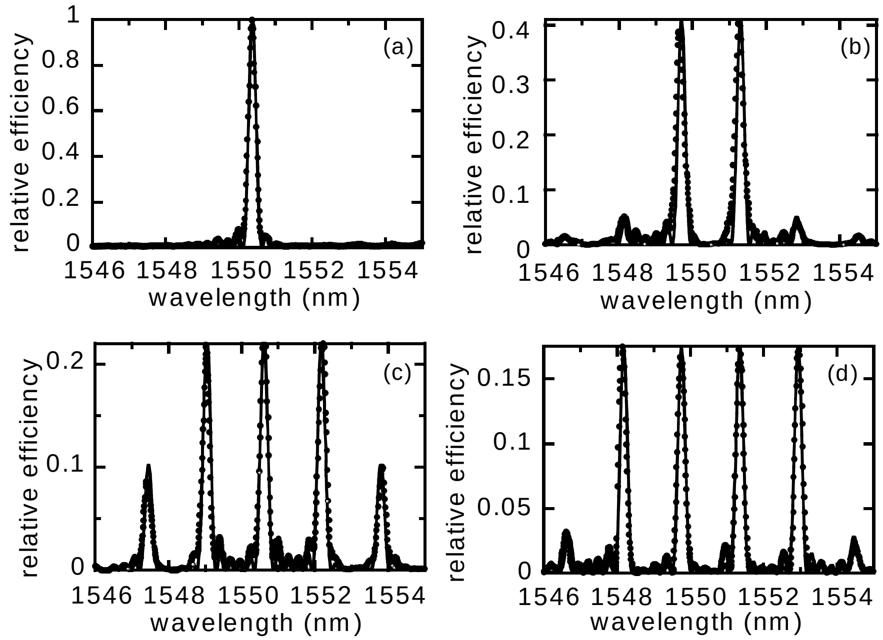

Figure 7.3 SHG wavelength-tuning curves for (a) one-channel, (b) two-channel, (c) three-channel, and (d) four-channel devices. The closed circles are measured results, and the solid lines are theoretical fits. The efficiencies are relative to the peak efficiency (~ 500%/W) of a one-channel device.

Applications

Figure 7.4 shows examples of applications of such multiple-channel devices. Wavelength-conversion function (figure 7.4(a)) in WDM optical networks can be performed with the flexibility to dynamically reconfigure the converted wavelengths by selecting the appropriate local oscillator wavelength. As in figure 7.4(b), using M local oscillator wavelengths these devices can also perform wavelength broadcasting, where each of N input signals is simultaneously converted into M output wavelengths. Other possible functions include multiple-channel drop, switching, optical sampling, etc.

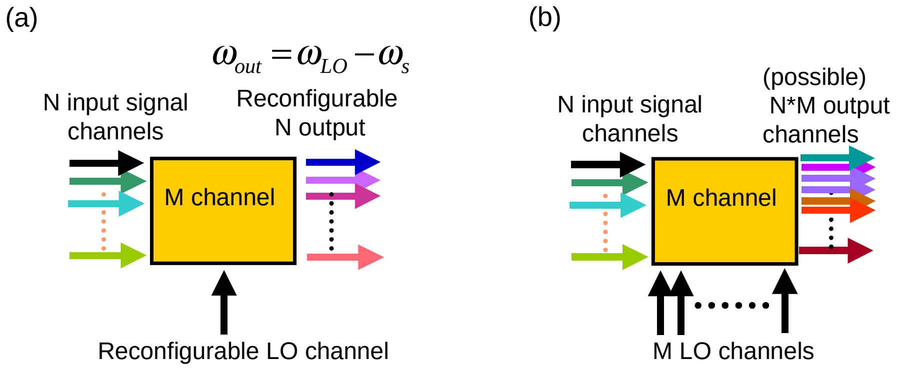

Figure 7.4 Examples of applications of multiple-channel OF mixers: (a) dynamic reconfiguration of wavelength conversion; (b) wavelength-broadcasting function by using M local oscillator wavelengths simultaneously.

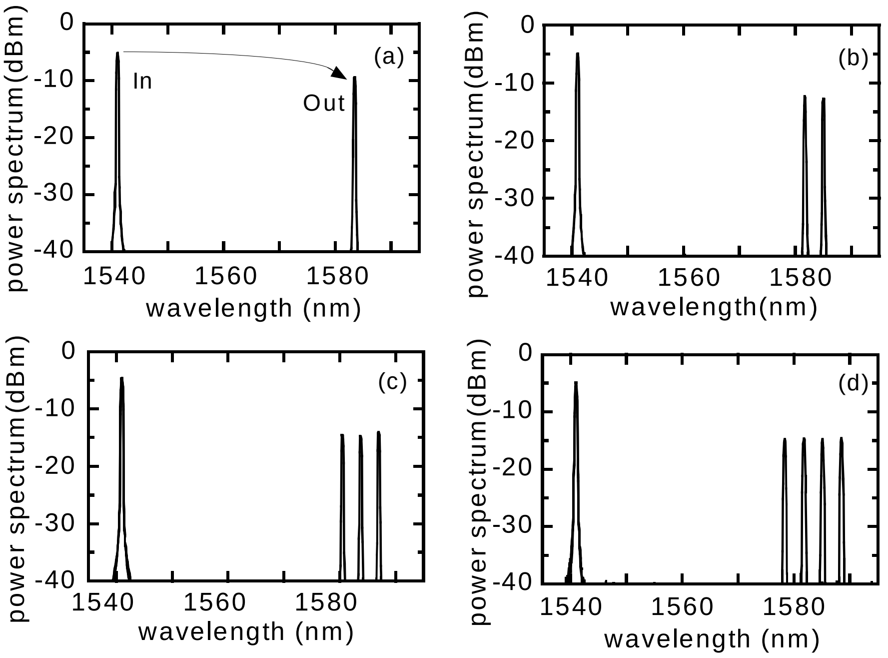

Figure 7.5 Measured multiple-channel wavelength conversion of (a) one-channel, (b) two-channel, (c) three-channel, and (d) four-channel devices. These plots show the combination of wavelength conversion of each individual channel.

Using the multiple-channel devices, we performed wavelength-conversion functions to demonstrate the applications illustrated in figures 7.4(a) and 7.4(b), i.e. dynamic reconfiguration of wavelength conversion and wavelength broadcasting. We used a CW Ti-sapphire laser operating at ~780 nm as local oscillator and chose to operate the device at ~120 °C to avoid photorefractive effects. This effectively shifts the phasematching wavelength to ~1562 nm but keeps the other parameters unchanged. The 780-nm local oscillator and the 1.5-µm-band signal were free-space launched into two different waveguides and combined into the wavelength-conversion section by an integrated directional coupler. Figure 7.5(a) shows the measured output spectrum for a single-channel device. The internal conversion efficiency is about -4 dB with a local oscillator at a wavelength of 781 nm and ~90 mW of local oscillator power coupled into the waveguide. Figures 7.5(b), 7.5(c), and 7.5(d) show the results with internal conversion efficiencies of ~-7 dB, -9 dB, and -10 dB for the two-, three-, and four-channel devices, respectively. We obtained these curves by tuning the local oscillator to each individual phasematching wavelength and combining the results in the same graph, since four local oscillators were unavailable at the time. However, by use of multiple local oscillator wavelengths, these devices can convert one or more inputs to multiple output wavelengths simultaneously.

We measured the bandwidth of the wavelength converters by tuning the input signal wavelength with the local oscillator fixed at each individual phasematching wavelength. The 3-dB conversion bandwidth is the same (~56 nm) for both the single-channel device and each individual channel in the multiple-channel devices. Figure 7.6 shows the bandwidth of each individual channel in a two-channel device.

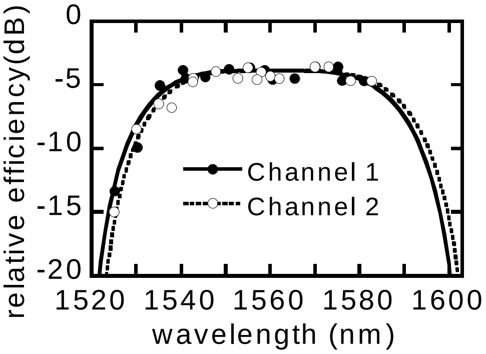

Figure 7.6 Signal bandwidth of each individual channel in a two-channel device. The circles are measured results and the lines are theoretical predictions. The efficiencies are relative to the peak efficiency of a one-channel device with the same interaction length.

We also designed and fabricated 1.3/1.5-μm multiple-channel OF mixers for wavelength conversion between the 1.3-μm-band and 1.5-μm-band. These devices have a QPM period of 12.4 μm and a 36-mm-long wavelength-conversion section. Sum-frequency generation measurements were performed to evaluate the characteristics of these devices by tuning one wavelength in the 1.5-μm-band with the other wavelength fixed at 1.319 μm. The results are similar to the SHG results shown in figure 7.3. We performed the wavelength-conversion experiment by mixing a signal at wavelength of ~1540 nm and a local oscillator from the Ti-sapphire laser at wavelength of ~718 nm. Figure 7.7 shows the measured output spectrum obtained by tuning the local oscillator wavelength to each individual phasematching wavelength and combining the results in the same graph. The conversion efficiencies are about -7 dB, -10 dB, -12 dB, and -14 dB for the one-, two-, three-, and four-channel devices, respectively, with ~50-mW local oscillator power coupled into the waveguides. The same devices can also perform multiple-wavelength conversion from the 1.3-µm-band to the 1.5-µm-band.

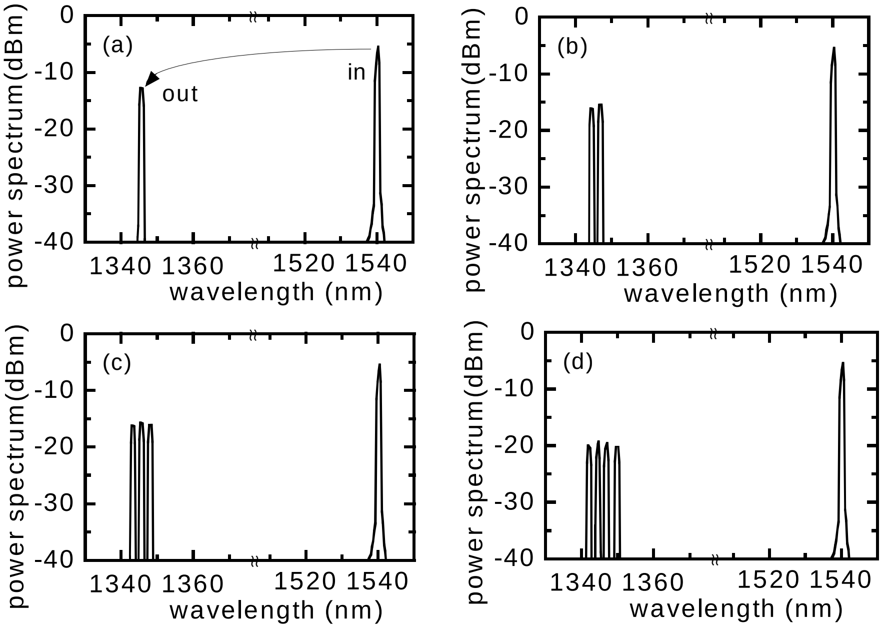

Figure 7.7 Multiple-channel wavelength conversion of 1.5-µm-band to 1.3-µm-band for (a) one-channel, (b) two-channel, (c) three-channel, and (d) four-channel devices. These plots were formed in the same way as figure 7.5.

The 1.3/1.5-µm device has a 3-dB bandwidth of ~6 nm, which is approximately one-tenth that of the 1.5-µm-band device, as discussed in section 5.3. Hence with a fixed local oscillator wavelength, the device can accommodate only a limited number of signal channels for the 1.3/1.5-µm conversion. It has been shown in section 5.3 that a very wide signal bandwidth is accessible by use of a tunable local oscillator. Multiple-channel devices can also be used to obtain a range of signal bandwidths with a single local oscillator wavelength, since each phasematching peak allows for the generation of a separate signal band. Figure 7.8 shows the signal bands of a two-channel device that uses a local oscillator fixed at ~718.1 nm.

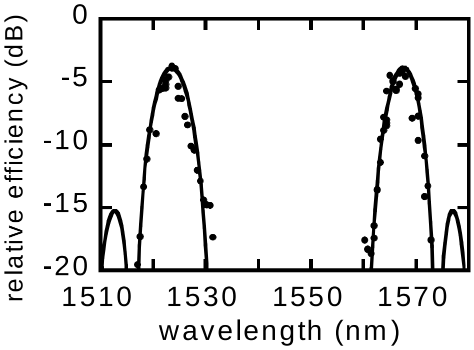

Figure 7.8 Bandwidth of each individual channel for a 1.3/1.5-µm two-channel device at a fixed local oscillator wavelength (718.1 nm). The efficiencies are relative to the peak efficiency of a one-channel device with the same interaction length.

7.3 Stability and Bandwidth Enhancement

Introduction

Although wavelength conversion based on DFM has a wide signal-conversion bandwidth (~60-90 nm), the local oscillator bandwidth is in general narrow (~0.1 nm) as will be described in the following section. Traditionally, the local oscillator is chosen to operate at the degenerate phasematching wavelength, where $\lambda_{out}=\lambda_{signal,0}$ and $\lambda_{LO,0}=\lambda_{signal,0}/2$. ($\lambda_{LO}$, λ_{signal}, and λ_{out} are local oscillator, input signal, and converted output wavelengths, respectively; subscript 0 denotes degeneracy). However, the conversion efficiency and its bandwidth will be sensitive to drifts in device temperature or the local oscillator wavelength under these circumstances. In this section, we address and solve this instability problem by detuning the local oscillator from the degenerate phasematching wavelength. We also discuss the possibility for further enhancement of the device stability and bandwidth by use of non-uniform QPM structures.

Theory

In nonlinear frequency-conversion processes such as SHG and DFM, the conversion efficiency is proportional to $\mathrm{sinc}^2(\Delta\beta L/2)$, where $\Delta\beta L$ is the phase mismatch among the interacting waves for a given QPM grating. We can Taylor expand the phase mismatch $\Delta\beta L$ as a function of an arbitrary parameter ξ (such as λ_{signal}, λ_{LO}, or temperature):

$$\Delta\beta L(\xi)=\Delta\beta L(\xi_0)+(\xi-\xi_0)\frac{d}{d\xi}\Delta\beta L(\xi_0)+(\xi-\xi_0)^2\frac{d^2}{d\xi^2}\Delta\beta L(\xi_0)+\ldots\ldots \qquad (7.6)$$

For near-degenerate DFM (λ_{out}~λ_{signal}~$2\lambda_{LO}$), the first derivative of phase mismatch with respect to the signal wavelength is equal to zero, due to the signal and output wavelengths moving in opposite directions with signal tuning. Thus, the phase mismatch depends only on the second and higher derivatives, resulting in a wide signal bandwidth. The first derivative of the phase mismatch with respect to the local oscillator wavelength is not zero because no signal/output wavelength cancellation occurs. Thus the magnitude of phase mismatch is strongly dependent on the local oscillator wavelength, so that a well-chosen local oscillator wavelength and stable temperature are necessary for practical device operations.

Experiments

To efficiently access the wide signal-conversion bandwidth, it is not optimal to use a local oscillator at the degenerate wavelength $\lambda_{LO,0}$. Instead, the local oscillator wavelength should be chosen to be slightly shorter than degeneracy to achieve global optimization. To illustrate this, we performed wavelength conversion using a DFM device under different local oscillator conditions. The device was fabricated with annealed proton-exchange in PPLN. The device includes integrated waveguide structures for efficient mode coupling and a 41-mm-long wavelength-conversion section with a QPM grating period of 15 μm.

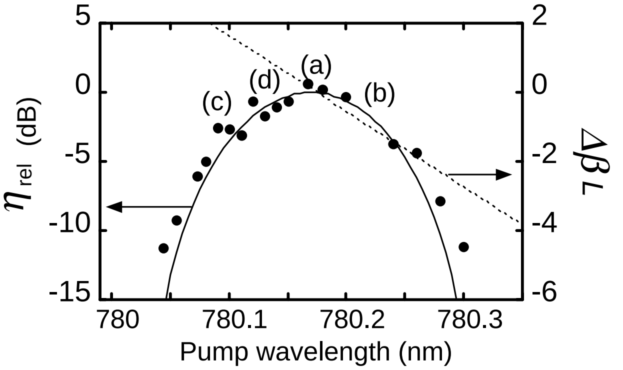

Figure 7.9 Relative conversion efficiency (η_{rel}) and calculated phase mismatch ($\Delta\beta L$) vs. local oscillator wavelength (λ_{LO}). The signal is fixed at ~$\lambda_{signal,0}$. η_{rel} = -3 dB at $\Delta\beta L = \pm 0.443\pi$. The points (a), (b), (c), and (d) correspond to the values of λ_{LO} used in figure 7.10.

Figure 7.9 shows the relative conversion efficiency (η_{rel}) and calculated phase mismatch ($\Delta\beta L$) versus λ_{LO}, with λ_{signal} fixed close to $\lambda_{signal,0}$=1560.34 nm. The efficiencies are normalized to the peak conversion efficiency, which is about -4 dB with ~90 mW of local oscillator power coupled into the waveguides. Using a local oscillator fixed at $\lambda_{LO,0}$, we measured η_{rel} versus λ_{signal}, as shown in figure 7.10(a). The 3-dB-bandwidth of this device is ~56 nm. η_{rel} is 0 dB at $\lambda_{signal,0}$ (where $\Delta\beta L$=0) and decreases slowly when the signal moves away from $\lambda_{signal,0}$.

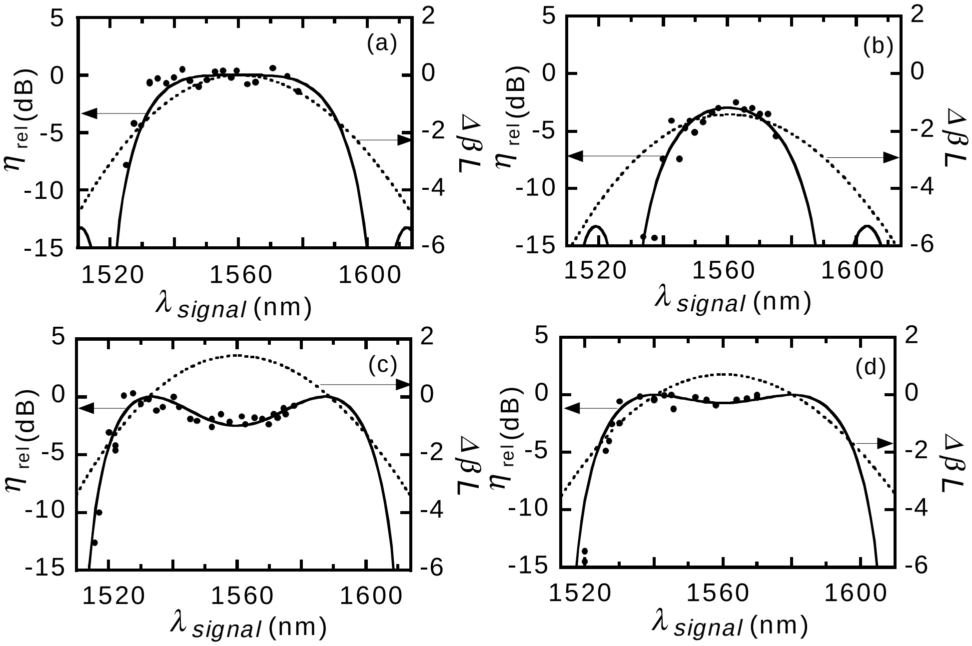

Figure 7.10 Conversion efficiency (η_{rel}) and calculated phase mismatch ($\Delta\beta L$) vs. input signal wavelengths (λ_{signal}) with local oscillator at wavelengths indicated in figure 7.9: (a) 780.170 nm, (b) 780.105 nm, (c) 780.235 nm, (d) 780.138 nm. The closed circles are the measured results, the solid line is the theoretical fit, and the dashed line is the calculated $\Delta\beta L$.

Figures 7.10(b) and 7.10(c) show the relative conversion efficiency η_{rel} and phase mismatch $\Delta\beta L$ with the local oscillator at wavelengths of $\lambda_{LO,0}$±0.065 nm. For the longer local oscillator wavelength, η_{rel} is -3 dB at $\lambda_{signal,0}$ but is reduced significantly at other signal wavelengths. This indicates the instability of operating the local oscillator at $\lambda_{LO,0}$, since small local oscillator wavelength up-drift will result in a significant drop in efficiency. For the shorter local oscillator wavelength, η_{rel} is -3 dB for $\lambda_{signal,0}$ but increases when the signal moves away from this point. Under this condition, there are two phasematching wavelengths (where $\Delta\beta L$=0) such that the 3-dB-bandwidth is 78 nm, which is 22 nm wider than that when the local oscillator is at $\lambda_{LO,0}$. This suggests that the local oscillator wavelength should be chosen in between the conditions of (a) and (c), allowing for both upward and downward drift of local oscillator wavelength and/or temperature, as shown in figure 7.10(d).

Non-uniform QPM grating

One can further optimize the device stability by using non-uniform QPM gratings. It has been shown that QPM gratings with de-phasing domains enhance the SHG bandwidth [12]. In the following, we theoretically investigate non-uniform QPM gratings, as shown in the inset of figure 7.11(i), for DFM wavelength conversion. The structure used here consists of three segments with length of L_1, L_2, L_3 where L_1=L_3, device length (L=L_1 + L_2 + L_3) is 41 mm, and L_1/L=0.107. Figure 7.11(i) shows the calculated η_{rel} vs. λ_{LO} for a QPM structure with phase-reversal gratings and the same device parameters as before. Figure 7.11(ii) shows plots of η_{rel} versus λ_{signal} for different local oscillator wavelengths. This QPM structure broadens the local oscillator and signal bandwidth (signal bandwidth >100 nm, but with some efficiency reduction). To efficiently use this non-uniform QPM grating, it is again necessary to operate the local oscillator at an off-degenerate wavelength.

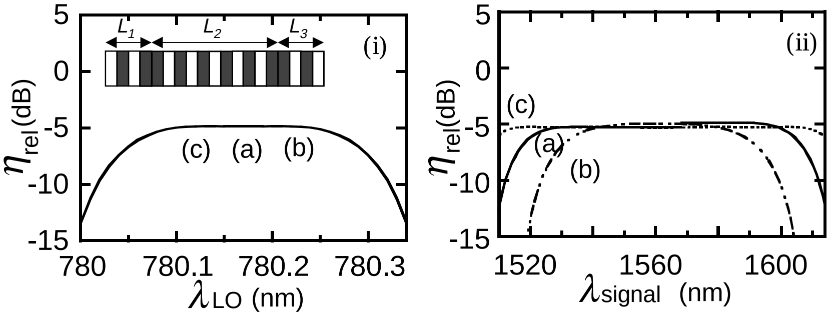

Figure 7.11 (i) η_{rel} vs. λ_{LO} for QPM structures with phase-reversal gratings. The inset is the schematic illustration of the QPM structures. (ii) η_{rel} vs. λ_{signal} for three different local oscillator wavelengths as indicated in (a), (b) and (c).

1.5-μm wavelength conversion based on $\chi^{(2)}:\chi^{(2)}$ allows for the use of a local oscillator within the 1.5-μm-band. The frequency-mixing process involves the cascading of SHG and DFM, which can be implemented using either co-propagating or counter-propagating local oscillator and signal beams. The method described above can be immediately applied to the counter-propagating scheme, in which the 1.5-μm local oscillator frequency is doubled by SHG, then reflected back into waveguides by a dichroic mirror to mix with signals by DFM. For the co-propagating scheme where SHG and DFM happen simultaneously, further optimization of non-uniform QPM gratings will be required.

7.4 Summary

Multiple-channel QPM optical frequency mixers and their novel applications in all-optical signal processing were presented. Dynamic reconfiguration of WDM wavelength conversion and wavelength broadcasting were demonstrated as examples. Multiple-channel wavelength add/drop, switching, and optical sampling could also be realized by these devices. In addition, these devices are potentially useful for wavelength-interchange cross connection in WDM networks and could have major impact in future multi-dimensional optical systems.

In the second part of this chapter, we used local oscillator detuning to enhance the stability and signal bandwidth in near-degenerate nonlinear frequency mixing. Both can be further enhanced by use of non-uniform quasi-phasematching structures with local oscillator detuning. As has been shown, twice the local oscillator bandwidth and over 100-nm signal bandwidth can be efficiently obtained by this approach.

Reference for Chapter 7:

---

1. R. N. Bracewell, *The Fourier Transform and its Applications*, 2 ed. (McGraw-Hill, New York, 1986).
2. M. M. Fejer, G. A. Magel, D. H. Jundt, R. L. Byer, “Quasi-phase-matched second harmonic generation: tuning and tolerances,” *IEEE J. Quantum Electron.* **28**, 2631-2654 (1992).
3. T. Suhara and H. Nishihara, “Theoretical analysis of waveguide second-harmonic generation phase matched with uniform and chirped gratings,” *IEEE J. Quantum Electron.* **26**, 1265-1276 (1990).
4. M. L. Bortz, M. Fujimura, and M. M. Fejer, “Increased acceptance bandwidth for quasi-phasematched second harmonic generation in $LiNbO_3$ waveguides,” *Electron. Lett.* **30**, 34-35 (1994).
5. M. L. Bortz, “Quasi-phasematched optical frequency conversion in lithium niobate waveguides,” Ph.D. Dissertation, Department of Applied Physics, Stanford University, Stanford, CA (1994).
6. K. Mizuuchi, K. Yamamoto, M. Kato, and H. Sato, “Broadening the phase-matching bandwidth in quasi-phasematched second harmonic generation,” *IEEE J. Quantum Electron.* **30**, 1596-1604 (1994).
7. K. Mizuuchi and K. Yamamoto, “Waveguide second-harmonic generation device with broadened flat quasi-phase-matching response by use of a grating structure with located phase shifts,” *Opt. Lett.* **23**, 1880-1882 (1998).
8. G. Imeshev, A. Galvanauskas, D. Harter, M. A. Arbore, M. Proctor, M. M. Fejer, “Engineerable femtosecond pulse shaping by second-harmonic generation with Fourier synthetic quasi-phase-matching gratings,” *Opt. Lett.* **23**, 864-866 (1998).
9. M. A. Arbore, “Generation and manipulation of infrared light using quasi-phasematched devices: ultrashort-pulse, aperiodic-grating and guided-wave frequency conversion,” Ph.D. Dissertation, Department of Electrical Engineering, Stanford University, Stanford, CA (1998).
10. M. A. Arbore, A. Galvanauskas, D. Harter, M. H. Chou, M. M. Fejer, “Engineerable compression of ultrashort pulses by use of second-harmonic generation in chirped-period-poled lithium niobate,” *Opt. Lett.* **22**, 1341-1343 (1997).
11. M. H. Chou, K. Parameswaran, and M. M. Fejer; I. Brener, “Multiple channel wavelength conversion using engineered quasi-phasematching structures in $LiNbO_3$ waveguides,” *CLEO’99*, CTuW7.
12. M. H. Chou, I. Brener, K. Parameswaran, and M. M. Fejer, “Stability and bandwidth enhancement of difference frequency generation based wavelength conversion by pump detuning,” *CLEO’99*, CWB8.

CHAPTER 8

CONCLUSION

8.1 Summary of Research Contributions

The essential contributions of this research are the development of techniques for designing and fabricating efficient annealed proton-exchanged periodically poled $LiNbO_3$ (APE-PPLN) waveguides and the successful demonstration of OF mixers for optical fiber communications.

Waveguide design by use of integrated structures facilitates the coupling of the input radiation into desired modes as well as the device optimization. The development of APE-PPLN fabrication techniques and integrated waveguide structures enabled several successful demonstrations of guided-wave nonlinear frequency mixing, which include efficient telecommunication-band OF mixers, waveguide optical parametric generators, mid-infrared difference-frequency generators, and noncritical waveguides. As a result of this research, efficient APE-PPLN waveguides in the telecommunication bands with nonlinear mixing efficiency of ~750%/W were demonstrated.

The demonstrated OF mixers for optical fiber communications include the 1.5-μm-band wavelength converter, 1.3/1.5-μm-band bi-directional wavelength converter, and mid-span spectrum inverter (MSSI). The demonstrated 1.5-μm-band wavelength converters are implemented by three different conversion schemes, which are difference-frequency mixing (DFM), cascaded second-order nonlinear frequency mixing ($\chi^{(2)}$:$\chi^{(2)}$ mixing) using co-propagating beams, and $\chi^{(2)}$:$\chi^{(2)}$ mixing using counter-propagating beams. The different schemes are complementary to each other, with advantages depending on the future availability of different local oscillators. Bi-directional wavelength conversion between the 1.3-μm-band and the 1.5-μm-band is a unique feature of $\chi^{(2)}$-based wave mixing, currently impossible by other conversion techniques. Mid-span spectral inversion, demonstrated in a system with 4x10 Gbits/s over 150 km of single mode fiber (SMF), provides a promising method for dispersion compensation in fiber links. The availability of efficient and compact wavelength converters and mid-span spectral inverters will be important for the evolution of optical fiber communication systems.

Multiple-channel OF mixers using non-uniform quasi-phasematching (QPM) structures are also demonstrated in this work. They are useful for dynamic re-configuration of wavelength conversion nodes, can provide wavelength-broadcasting functions, and are also potentially important in wavelength interchanging cross connects. An approach to enhance the device bandwidth and stability has also been investigated, showing the feasibility of flat signal bandwidth (over 100 nm) to cover the future generation of erbium-doped-fiber amplifiers (EDFA's) [1]. In addition, theoretical study of an optical gated mixer provides the basis for the future applications of OF mixers in time-division multiplexed (TDM) systems.

8.2 Future Research

Polarization Dependence

The devices demonstrated in this work show several major advantages of OF mixers for optical fiber communications. However, one further step, i.e. successful demonstration of polarization insensitive devices, is required for practical system applications. This can be accomplished by use of the polarization diversity schemes illustrated in Chapter 5. The polarization diversity scheme for wavelength conversion has been demonstrated using four-wave mixing (FWM) in semiconductor optical amplifiers (SOA's) and optical fibers. Using the schemes shown in figure 5.20(b), we made a preliminary demonstration of polarization insensitive devices. Further characterization, such as bit error rate in a wavelength-division multiplexed (WDM) testbed, are being performed. Successful demonstration of low polarization dependence will lead to a practical component for real systems. Another solution to realize the polarization insensitive device is use of AlGaAs waveguides, which has been demonstrated by Yoo [2]. However, such devices currently suffer from low conversion efficiency due to the high propagation losses. Recently, all-epitaxially patterned twinning of AlGaAs thin films developed by Eyres at Stanford University show promising results for high performance AlGaAs devices in the future [3].

Further Improvement of Device Efficiency

Although high conversion efficiency has been demonstrated in this research, there is still need to increase the conversion efficiency. Improved waveguide design for nonlinear frequency mixing, such as using the fundamental mode (TM_{00}) of the signal and the first high-order mode (TM_{01}) of its harmonic wave, is one of the solutions described in Chapter 4. Recently, there are several reported waveguide fabrication techniques to increase the nonlinear frequency-conversion efficiency, such as using soft proton or vapor phase methods [4, 5]. The results show several attractive properties, including high refractive index increase (~0.03) and no dead layer induced by the fabrication process. Zn-diffusion is an attractive waveguide fabrication process that appears highly robust with respect to photorefractive damage [6]. These processes are potentially important for fabricating high quality PPLN waveguides in the future. To make devices with good quality by use of these processes, further characterization and waveguide modeling are required.

Photorefractive Damage

Due to photorefractive effects, the use of $LiNbO_3$ requires operation of the device at an elevated temperature. Some related $LiNbO_3$–based materials (i.e. $MgO:LiNbO_3$ and $Zn:LiNbO_3$) have been shown to be more resistant to photorefractive damage [7]. Devices fabricated on those doped $LiNbO_3$ substrates would provide the possibility for operating at a lower temperature and would allow handling higher power. Another attractive material that can be designed to be polarization insensitive is an AlGaAs waveguide, which has a higher nonlinearity and no photorefractive effects. Further research in this material would possibly make efficient OF mixers with an integrated diode laser as a local oscillator.

Other Novel and Important Devices

Engineerable QPM structures can be used to tailor the device to other novel functions, such as the multiple-channel converters demonstrated in Chapter 7. Other novel devices can be designed and fabricated by the non-uniform QPM structures and using Fourier synthetic QPM gratings as a general design tool.

For TDM applications, several important functions can be realized with the OF mixers demonstrated in this work. Examples include clock recovery, multiplexing/demultiplexing of multiple TDM channels, and optical sampling [8, 9]. The theoretical investigation of optical gated mixers in TDM systems is described in Appendix A. The performance of the optical gated mixers is mainly limited by the group-velocity mismatch between the 1.5-μm-band signal and its harmonic wave. Improvement on the normalized efficiency or a method to compensate for the group-velocity mismatch among the interacting waves will be important for the further progress in those applications.

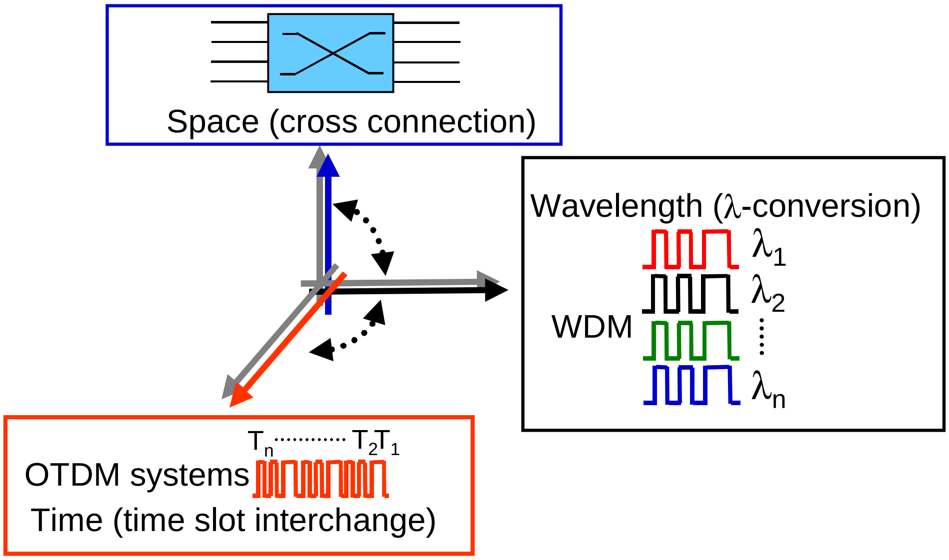

Figure 8.1 Multiple-dimension optical fiber communication system, where space, wavelength, and time are all used as degrees of freedom to increase the system capacity. Information exchange among these dimensions is important for the realization of a transparent optical network.

The results accomplished in this research could lead to the development of OF mixers as practical components for optical fiber communications. It is anticipated that with the further development of PPLN waveguide devices or AlGaAs waveguides, OF mixers will be applied to a variety of practical applications. This research has the potential to make a lasting impact in the future multi-dimensional optical fiber communications (figure 8.1), where space, wavelength, and time are all used as degrees of freedom to increase the system capacity. In addition, the same device can also be applied to a variety of nonlinear frequency-conversion processes such as efficient mid-IR generation or ultra-short pulse applications.

Reference for Chapter 8:

---

1. Y. Sun, J. W. Sulhoff, A. K. Srivastava, J. L. Zyskind, C. Wolf, T. A. Strasser, J. R. Pedrazzani, J. B. Judkins, R. P. Espindola, A. M. Vengsardar, J. Zhou, “An 80 nm ultra wide band EDFA with low noise figure and high output power,” 11th International Conference on Integrated Optics and Optical Fibre Communications 23 European Conference on Optical Communications *IOOC-ECOC97*.
2. S. J. B. Yoo, C. Caneau, R. Bhat, M. A. Koza, A. Rajhel, and X. N. Antoniades, “Polarization-independent, multichannel wavelength conversion by difference frequency generation in quasi-phase-matched AlGaAs waveguide,” *CLEO’96*, JTuE1.
3. L. A. Eyres, C. B. Ebert, M. M. Fejer, J. S. Harris, “MBE growth of laterally antiphase-patterned GaAs films using thin Ge layers for waveguide mixing,” *CLEO’98* CWH4.
4. K. El Hadi, V. Rastogi, M. R. Shenoy, K. Thyagarajan, M. De Micheli, D. B. Ostrowsky, “Spectral measurement of the film-substrate index difference in proton-exchanged $LiNbO_3$ waveguides,” *Appl. Opt.* **37**, 6463-6467 (1998).
5. J. Rams, J. M. Cabrera, “Preparation of proton-exchange $LiNbO_3$ waveguides in benzoic acid vapor,” *J. Opt. Soc. Am. B* **16**, 401-406 (1999). J. Rams, J. M. Cabrera, “Nonlinear optical efficient $LiNbO_3$ waveguides proton exchanged in benzoic acid vapor: Effect of the vapor pressure,” *J. Appl. Phys*. **85**, 1322-1328 (1999).
6. W. M. Young, M. M. Fejer, M. J. F. Digonnet, A. F. Marshall, R. S. Feigelson, “Fabrication, characterization and index profile modeling of high-damage resistance Zn-diffused waveguides in congruent and MgO:lithium niobate,” *J. Lightwave Technol.* **10**, 1238-1246 (1992).
7. K. Mizuuchi, K. Yamamoto, M. Kato, “Harmonic blue light generation in X-cut $MgO:LiNbO_3$ waveguide,” *Electron. Lett.* 33, 806-807 (1997).
8. S. Kawanishi, “Ultrahigh-speed optical time-division-multiplexed transmission technology based on optical signal processing,” *IEEE J. Quantum Electron.* **34**, 2064-2079 (1998).
9. T. Suhara, H. Ishizuki, M. Fujimura, and H. Nishhara, “Waveguide quasi-phase-matched sum-frequency generation device for optical sampling,” *ECIO’99*, pp 501-504.

Appendix A: Optical Gated Mixers in TDM Systems

A.1 Introduction

In TDM systems**,** low bit-rate channels are multiplexed into a high bit-rate time-sequential stream, in which each channel is synchronized and carried by the same wavelength. High speed TDM is an efficient way to increase the transmission capacity of a given fiber link [1, 2, 3]. Moreover, the combination of WDM and TDM, i.e. WDM/TDM systems, can further optimize the system capacity and flexibility [4, 5]. The ability to process ultra-short pulses (in the range of pico-seconds) is essential to TDM systems. Due to the speed limitation of electronic circuitry (currently ~40 Gbits/s), optical techniques will be important in order to fully exploit the transmission bandwidth. The OF mixers described in the previous chapters are well suited for such purposes due to their instantaneous parametric interaction. In this appendix, we describe OF mixers for TDM applications.

A.2 Principle and Application

The OF mixers demonstrated in the previous chapters can be used as optical gated mixers, with short optical pulses used as local oscillators or optical clocks. When the optical clocks are temporally overlapped with TDM signals, nonlinear frequency mixing generates wavelength-shifted outputs containing signal information that is synchronized to the clock. Figure A.1 shows example applications of the optical gated mixers [6, 7]. They can be used as de-multiplexers to extract a TDM channel with a low repetition rate optical clock, or as clock recovery components to remove the time jitter of TDM signals by interacting with a synchronized optical clock. When a chirped optical clock is used, the mixers can also be used as multiple-channel de-multiplexers or as TDM to WDM converters where each TDM channel is converted into a different wavelength output. Other applications include WDM to TDM conversion, TDM time slot interchanging, and optical sampling.

For the 1.5-μm-band applications, the optical clock can be at a wavelength of ~780 nm by DFM or ~1550 nm by $\chi^{(2)}:\chi^{(2)}$ mixing. We will illustrate an application based on $\chi^{(2)}:\chi^{(2)}$ mixing with counter-propagating beams, because it allows the use of 1.5-μm-band optical clock and has higher conversion efficiency than co-propagating schemes. In this frequency mixing process, the 1.5-μm-band TDM signals are amplified and converted to 780 nm by SHG. The generated 780 nm is reflected back by a dichroic mirror into the waveguide and interacts with the optical clock to generate the frequency-shifted output. In such a conversion scheme, the converted output power scales approximately with the square of the signal power and is linearly proportional to the clock power. This scheme allows the generation of tunable output by tuning the clock wavelength. In analyzing such a conversion process, two factors need to be considered: signal depletion in the SHG process and group-velocity mismatch (GVM) of the 1.5-μm wave and its harmonic wave.

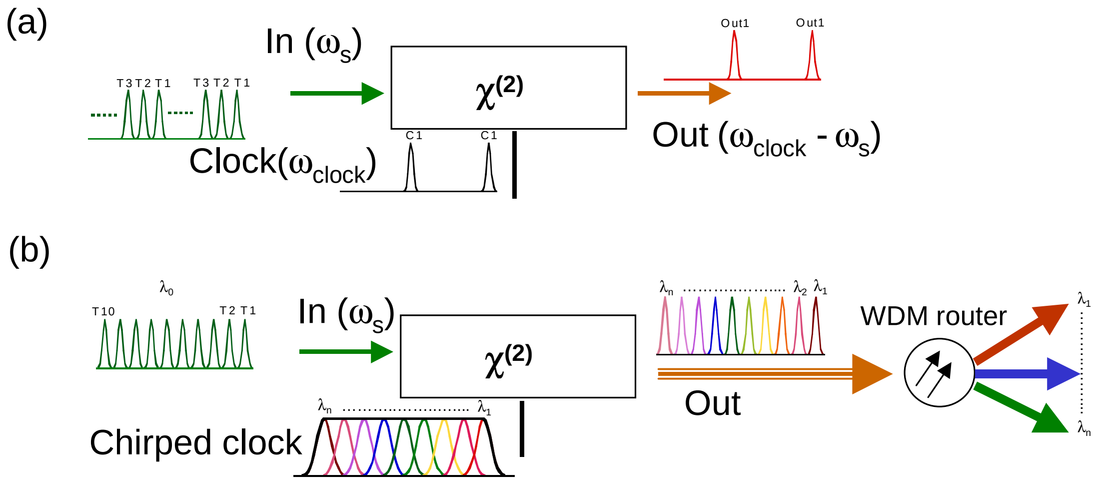

Figure A.1 Examples of applications of OF mixers in TDM systems. (a) Clock recovery and TDM demultiplexing, (b) multi-channel demultiplexing and TDM to WDM conversion using a linearly chirped clock.

A.3 Simulation Results of Multi-Channel Demultiplexing

As an example, we show simulation results of OF mixers in PPLN waveguides for applications as multiple-channel de-multiplexers and TDM/WDM converters. The device consists of a uniform QPM grating, and is assumed to have a normalized efficiency of 150%/W-cm^2 and no waveguide propagation losses. The GVM between 780 nm and 1550 nm, i.e.

$$GVM = \frac{1}{v_g(\lambda_\omega)} - \frac{1}{v_g(\lambda_{2\omega})},$$

is 0.32 ps/mm. A 10-GHz linearly chirped supercontinuum square pulse is used as clock [7]. A 100-GHz TDM signal train (…0111011010…) is mixed with this chirped clock. It is assumed that both the optical signal and optical clock are amplified to a peak power level of 200 mW.

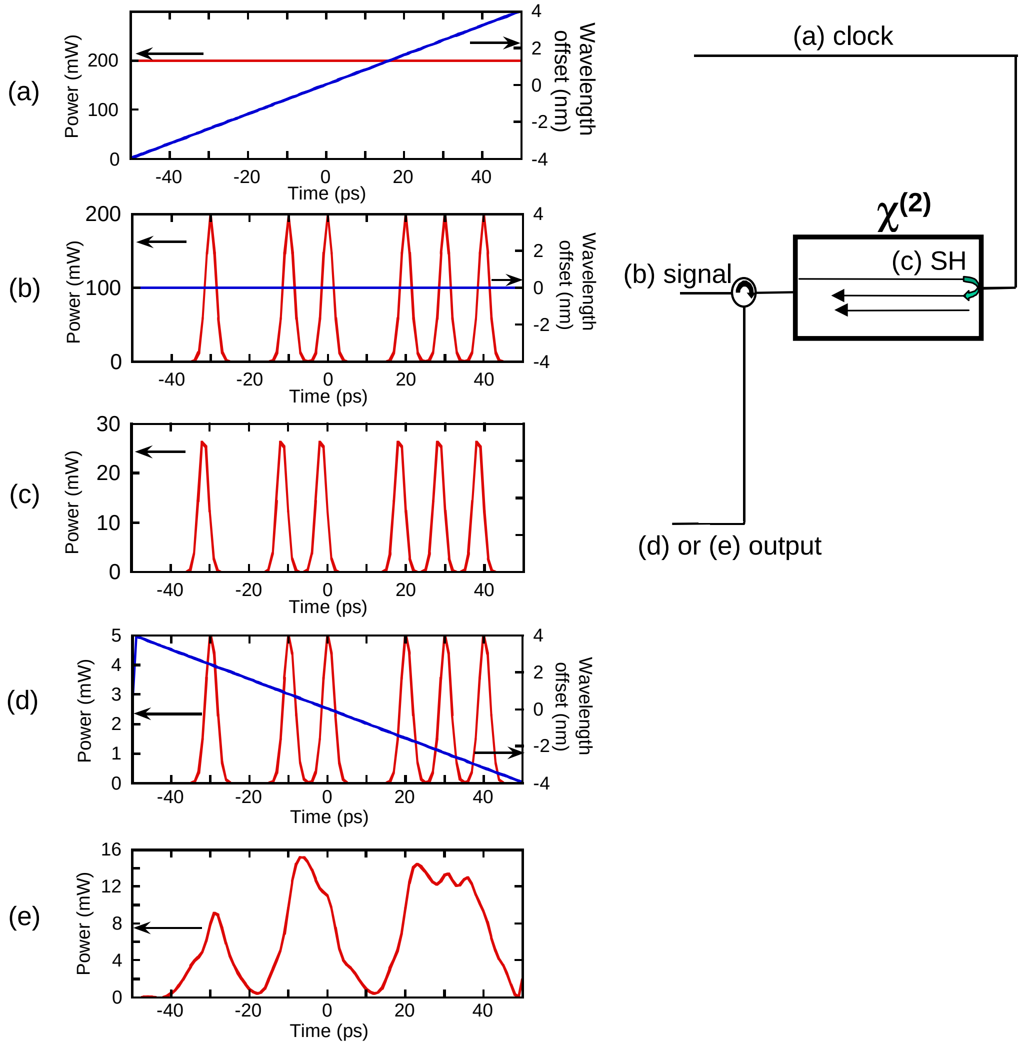

Figure A.2 Simulation results of multiple-channel demultiplexing using a chirped clock. (a) Input linearly chirped square clock, (b) input 100-GHz TDM signal, (c) converted SH wave of input 100-GHz TDM signal after the first single pass using a device with 1-cm interaction length. (d) converted output using a device with 1-cm interaction length, (e) converted output using a device with 5-cm interaction length showing effect of GVM.

The signal and clock pulses have Gaussian profiles with 1/*e*-pulse width of 3 picoseconds, and are counter-propagating into the device. In such a mixing process, the TDM signals are first converted into second-harmonic (SH) waves and then reflected back into the waveguide to interact with the chirped clock. The SH wave of each TDM channel interacts with a different part of the chirped clock and thus is converted to a different output wavelength. Figure A.2 shows simulation results of such a conversion process based on coupled-mode equations (2.27) and (2.28). Figure A.2(d) is the converted output of a device with 1-cm interaction length. The converted output chirp is a reversal of the input clock chirp, thus the sign of the output chirp can be controlled. Due to the very wide conversion bandwidth for such a conversion process, the device has a wide range over which it can be tuned and reconfigured in WDM channel mapping. One can choose the output wavelength by tuning the clock wavelength or change the output channel separation by adjusting the clock chirp rate. To illustrate the limitation due to GVM, we perform a simulation using a device with 5-cm interaction length, as shown in figure A.2(e).

A.4 Tapping TDM Signal by SFM

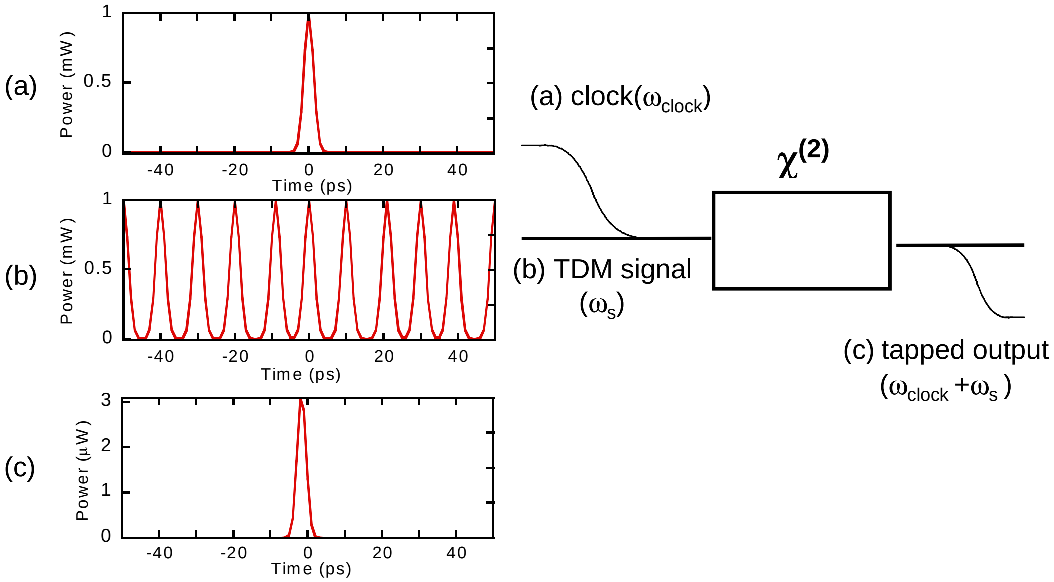

Figure A.3 Operation scheme and simulation results of using OF mixers to tap one of the TDM channels. (a) Input 10-GHz clock, (b) input 100-GHz TDM signals, (c) SFM output using a device with 1-cm interaction length. Note that there is ~3 ps delay of SFM output relative to clock due to GVM.

To illustrate applications of OF mixers in other schemes, we describe and simulate how OF mixers can be used to tap TDM signals via sum-frequency mixing (SFM). In the simulation, we use a 10-GHz pulse as an optical clock to mix with a 100 GHz TDM signal train. It is assumed that both the optical signal and optical clock have a peak power of 1 mW. The signal and clock pulses have Gaussian profiles with 1/*e*-pulse width of 3 picoseconds and are co-propagating into a device. Figure A.3 shows the operation scheme and simulation results of such a conversion process. Summing the synchronized 1.5-μm-band signal and 1.5-μm-band optical clock yields a de-multiplexed SFM output at ~780 nm, which can be easily separated from the 1.5-μm-band signals and detected electronically. The above scheme can possibly also be used to dynamically de-multiplex one of the WDM channels by using a CW LO with the LO wavelength that is phasematched to the desired WDM channel.

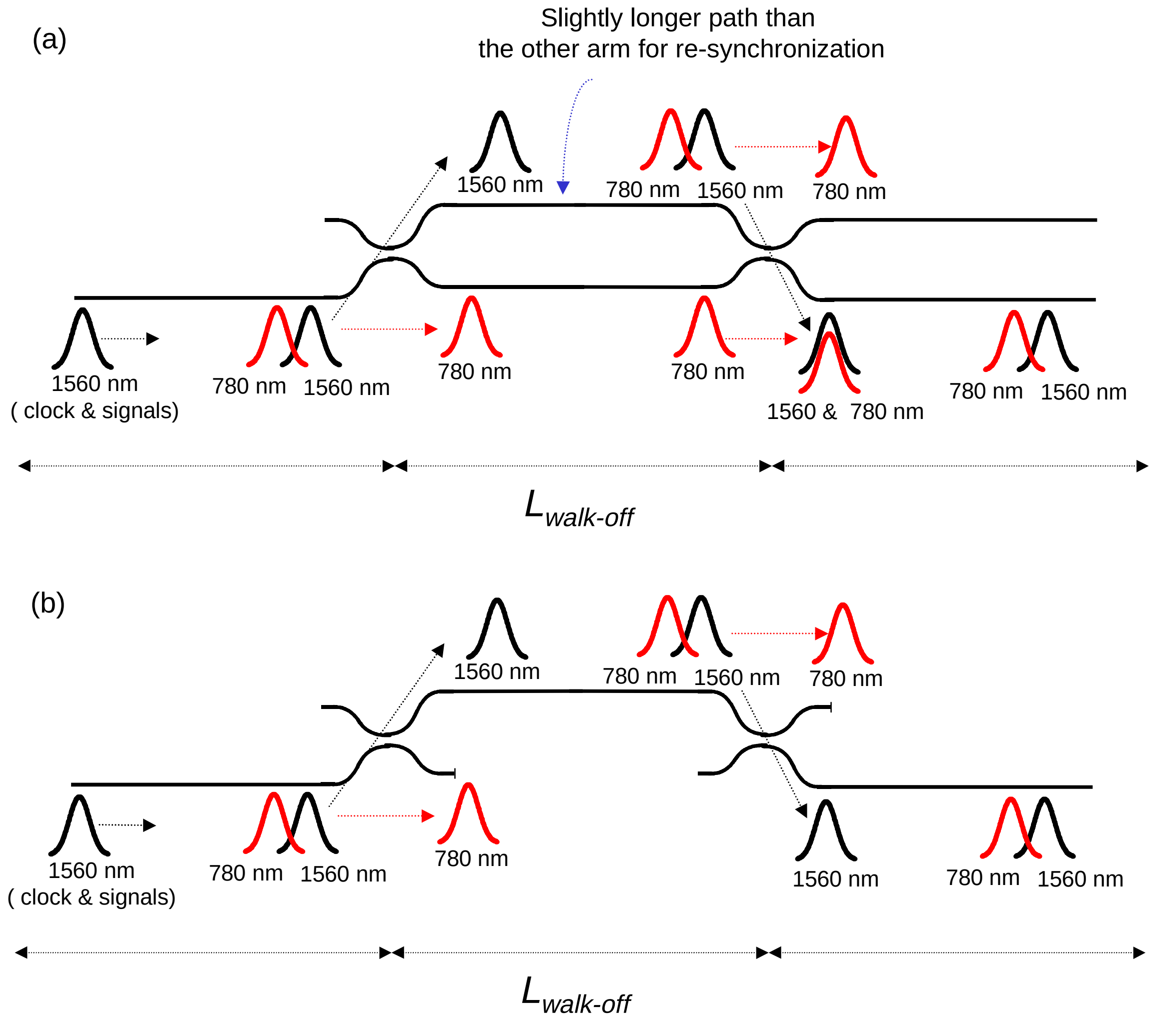

Figure A.4 Two possible schemes for GVM compensation. (a) More efficient but phase-sensitive scheme; (b) phase-insensitive scheme.

The efficiency of $\chi^{(2)}$-based OF mixers is very often limited by GVM among the interacting waves. It is possible to compensate the GVM using more sophisticated schemes. Figure A.4 shows two possible schemes for GVM compensation, allowing the use of longer devices. In the scheme shown in figure A.4(a), the long wavelength (1.5-µm band) and short wavelength (~780 nm) are separated by a directional coupler after one walk-off length. The long wavelength is passed through the arm with a slightly longer path to re-synchronize with respect to the short wavelength and then they are recombined by a directional coupler. Using this scheme for a device with the number of sections N (i.e. the length of the device is $NL_{walk\text{-}off}$), the efficiency scales approximately with $N^2/2$ for the SHG process and $N^4/4$ for cascaded $\chi^{(2)}:\chi^{(2)}$ mixing, as compared to N^2 and N^4 in the case of the same interaction length but without GVM. The major drawback is that this scheme requires not only to synchronize the envelopes of the interacting wavelengths but also to adjust the path accurately to preserve the correct phase relation among the interacting waves, a practical challenge.

Another scheme shown in figure A.4(b) allows the phase-insensitive operation. The arm for the short wavelength is blocked and the interaction restarts again at each section after the long wavelength is coupled through the directional coupler. This scheme has the advantage that it does not require re-synchronization and interferometric stability on recombining, however, the efficiency of this scheme scales only linearly with the number of sections N.

A.6 Summary

We have discussed the applications of OF mixers in TDM systems. For a highly efficient device, the efficiency is mainly limited by GVM between the short wavelength (~780 nm) and the long wavelength (~1.5 μm). Making an extra long device cannot increase the efficiency and would cause inter-symbol interference among different TDM channels. To increase device efficiency, it is important to have a method to either improve the normalized efficiency (per unit length) to allow the use of a shorter device or a method to compensate GVM to allow the use of a longer interaction length.

Reference for Appendix A:

---

1. R. A. Barry, V. W. S. Chan, K. L. Hall, E. S. Kintzer, J. D. Moores, K. A. Rauschenbach, E. A. Swanson, L. E. Adams, C. R. Doerr, S. G. Finn, H. A. Haus, E. P. Ippen, W. S. Wong, and M. Haner, "All-Optical Network Consortium-ultrafast TDM networks," *IEEE J. Select. Areas Commum.* **14,** 999-1013 (1996).
2. S. W. Seo, K. Bergman, P. R. Prucnal, "Transparent optical networks with time-division multiplexing," *IEEE J. Select. Areas Commum.* **14,** 1039-1051 (1996).
3. S. Kawanishi, "Ultrahigh-speed optical time-division-multiplexed transmission technology based on optical signal processing," *IEEE J. Quantum Electron.* **34**, 2064-2079 (1998).
4. M. R. H. Daza, H. F. Liu, M. Tsuchiya, Y. Ogawa, T. Kamiya, "All-optical WDM-to-TDM conversion with total capacity of 33 Gb/s for WDM network links," *IEEE J. Sel. Top. Quantum Electron.* **3,** 1287-1294 (1997).
5. S. Kawanishi, H. Takara, K. Uchiyama, I. Shake, and K. Mori, "3 Tbit/s (160 Gbit/s x 19 ch) OTDM-WDM transmission experiment," *OFC'99*, PD1.
6. K. Uchiyama, H. Takara, T. Morioka, S. Kawanishi, M. Saruwatari, "100 Gbit/s multiple-channel output all-optical demultiplexing based on TDM-WDM conversion in a nonlinear optical loop mirror," *Electron. Lett*. **32**, 1989-1991 (1996).
7. T. Morioka, S. Kawanishi, H. Takara, M. Saruwatari, "Multiple-output, 100 Gbit/s all-optical demultiplexer based on multichannel four-wave mixing pumped by a linearly-chirped square pulse," *Electron. Lett*. **30**, 1959-1960 (1994).